Università di Pisa

FACOLTÀ DI INGEGNERIA
DIPARTIMENTO DI INGEGNERIA DELL'ENERGIA E DEI SISTEMI

Corso di Dottorato in
Automatica, Robotica e Bioingegneria

Ph.D. Dissertation on

On the Role of Haptic Synergies in Modelling the Sense of Touch and in Designing Artificial Haptic Systems

Candidate Student: **Matteo Bianchi**

Supervisors: **Prof. Antonio Bicchi**
Dott. Ing. Enzo Pasquale Scilingo

Course Cycle XXIV — Year of Enrolling 2009

to my sweet Eleonora
to Anto and Ari, my wonderful parents
to Adelmo, Alvaro, Giuseppina and Miriana, for their lovely simplicity

Abstract

This thesis aims at defining strategies to reduce haptic information complexity, with minimum loss of information, to design more effective haptic interfaces and artificial systems. Nowadays, haptic device design can be complex. Moreover, the artificial reproduction of the full spectrum of haptic information is a daunting task and far to be achieved. The central idea of this work is to simplify this information by exploiting the concept of *synergies*, which has been developed to describe the covariation patterns in multi-digit movements and forces in common motor tasks. Here I extend and exploit it also in the perceptual domain, to find projections from the heterogeneous information manifold, generated by the mechanics of touch, and what can be actually perceived by humans. In this manner, design trade-off between costs, feasibility and quality of the rendered perception can be individuated. With this as motivation, referring to cutaneous sensing, I discuss the development of a fabric-based softness display inspired by "Contact Area Spread Rate" hypothesis as well as the characterization of an air-jet lump display method for Robot-assisted Minimally Invasive Surgery. Considering kinaesthesia, I analyze the problem of hand posture estimation from noisy and limited in number measures provided by low cost hand pose sensing devices. By using the information about how humans most frequently use their hands, system performance is enhanced and optimal system design enabled. Finally,

an integrated device, where a conventional kinaesthetic haptic display is combined with a cutaneous softness one, is proposed, showing that the fidelity by which softness is artificially rendered increases.

Acknowledgement

First and foremost, I would like to show my deepest gratitude to my supervisor Prof. Antonio Bicchi, whose encouragement, guidance and wide knowledge have been essential in these years and enabled me to develop in an efficient manner my research activity. It was an honor for me to have him as supervisor.

I would like also to offer my deep and sincere gratitude to my supervisor Dott. Ing. Enzo Pasquale Scilingo. His encouragement, understanding as well as his precious suggestions and knowledge have represented for me a fundamental help in these years. I was honored to have him as supervisor.

I owe my most sincere gratitude to Prof. Allison M. Okamura, from Stanford University, who gave me the opportunity, during my PhD, to work with her at Laboratory for Computational Sensing and Robotics (LCSR) - Johns Hopkins University. It was an honor for me to spend six months under her wise guidance. I would like to thank also Dana Damian, Danilo De Lorenzo and all my friends from LCSR and CHARM (Collaborative Haptics and Robotics in Medicine) lab from Stanford University, especially Alperen Degirmenci and James C. Gwilliam, who collaborated with me during my research activity.

I would like to acknowledge Prof. Marco Santello, from Arizona State University, for the inspiring discussions and suggestions.

Last but not least, I am indebted to all my colleagues, friends and researchers from Interdepartmental Research Center "E. Piaggio" to support me. I would like to spend a few words for them.

So let me offer my deep gratitude to Fabio Vivaldi, for his wise

suggestions, Andrea Di Basco, for his encouragement and friendship, Dott. ssa Lucia Pallottino, for her guidance and patience, Dott. Ing. Marco Gabiccini, for the inspiring discussions, Fabio Bonomo, Manuel G. Catalano, Manolo Garabini, Spillo Altobelli, Davide Di Baccio, Edoardo Farnioli, Simone Martini, Adriano Fagiolini, Felipe Belo, Stefano Falasca, Antonio Lanatà, Armando Turco, Andrea Quagli, Alessandro Tognetti, Nicola Carbonaro, Michele Mancini, Gaetano Lorefice, Luca Greco, Riccardo Schiavi, Carlo Quartieri, Giorgio Grioli, for their friendship and all the help they have given to me in these years.

Let me also thank Agnese Carau, Alessandra Parravicini, Anna Smaniotto, Andrea Goetz, Francesca Carlino and Laura Maley for their extreme kindness.

Finally, let me show my sincere gratitude to my friend Gaetano Valenza, for his encouragement and wise suggestions, Alessandro Serio, for his friendship and precious help, and Paolo Salaris. His understanding, patience and help have provided an essential improvement to my research activity.

Contents

Abstract **v**

Acknowledgement **vii**

Introduction **1**

1 Real Touch and Rendered Touch **11**

2 Softness Displays: from Tactile Flow to Contact Area Spread Rate Paradigm. **21**

2.1 Tactile Flow Hypothesis 23
2.2 Experimental CASR 25
2.3 First Discrete CASR-based Display 27
2.4 A New CASR-based Display: the Fabric Yielding Display (FYD) 30
2.4.1 FYD: Structure Description and Functionality Explanation 31
2.4.2 Control 34
2.4.3 Area Acquisition 35
2.4.4 Characterization and Interpolation 36
2.4.5 Graphical User Interface and Virtual Reality Implementation 40

2.4.6 Psychophysical Experiments 44
2.4.7 Experimental Results and Discussion 47
2.4.8 Conclusions 50

3 New Strategies to Convey Cutaneous Information: a RMIS Application 53
3.1 Theoretical Background 56
3.2 Design and Characterization 58
3.2.1 Quantitative Characterization 60
3.2.2 Tactile Sensor Results 62
3.3 Human Subject Experiments 67
3.3.1 Preliminary Open Paradigm Experiment 67
3.3.2 Psychophysical - Pressure JND 70
3.3.3 Psychophysical - Aperture Size JND 74
3.4 Conclusions 78

4 Synergy-based Hand Pose Sensing 83
4.1 Kinematic Synergies and Their Applications 85
4.2 Performance Enhancement 88
4.2.1 The Hand Posture Estimation Algorithm 89
4.2.2 Model and Data capture 93
4.2.3 Simulation Results 96
4.2.4 Experimental Results 102
4.3 Optimal Design 107
4.3.1 Problem Definition 110
4.3.2 Continuous Sensing Design 111
4.3.3 Discrete Sensing Design 116
4.3.4 Hybrid Sensing Design 120
4.3.5 Continuous and Discrete Sensing Optimal Distribution 120
4.3.6 Estimation Results with Optimal Discrete Sensing Devices 124
4.4 Conclusions 131
4.5 Appendix 132

5 Integration of Cutaneous and Kinaesthetic Cues in a Haptic Device for Softness Rendering. 137
5.1 Motivation: Ambiguities in Unimodal Touch 139
5.2 The Integrated Haptic System 143
5.2.1 Control of the Integrated Display 144
5.3 Materials and methods 146
5.3.1 Subjects 146
5.3.2 Physical Specimens 148
5.3.3 Rendered Specimens 149
5.3.4 Design and Procedure 150
5.3.5 Experiments on Direct touch 151
5.3.6 Experiments on Rendered Touch 152
5.4 Experimental Results and Discussion 154
5.4.1 Pairwise Discrimination with Physical Specimens 154
5.4.2 Ranking of Physical Specimens 155
5.4.3 Pairwise Discrimination with Rendered Specimens 156
5.4.4 Ranking of Rendered Specimens 159
5.4.5 Comparison of Direct and Rendered Touch . . . 160
5.5 Conclusions 160

Bibliography 179

Introduction

This thesis aims at individuating models and strategies to harness the complexity of the sense of touch, by following a geometrical reduction approach that maps between a higher dimensional space of perceptual elemental variables (i.e. information provided by sensory receptors) and a lower dimensional space of primitives of percepts and performance variables, with limited loss of information. The goal is to use these primitives to drive the design and the improvement of haptic devices and artificial systems, in order to enable for a more compelling and reliable human-machine interaction.

According to the definition in [11], *haptic interfaces attempt to replicate or enhance the touch experience of manipulating or perceiving a real environment through mechatronic devices and computer control.* Haptics (haptic derives from Greek *haptesthai*, relative to touch) is the science whose purpose is to create and experience tactile stimuli in humans. The leading role in everyday life of the sense of touch and of its primary physical organ, i.e. the hand, is widely recognized as well as its importance both in the sensory and motor domain. Human beings explore the external world by means of their hands, which represent the fundamental channels to convey haptic information and to actively modify the environment. As Kant affirmed [12]: *This sense is the only one with an immediate exterior perception; due to this it is the most important and the most teaching one, but also the rough-*

est. Without this sensing organ we would not be able to grasp our physical shape, whose perception the other two first class senses (sight and hearing) have to be referred to, to generate some knowledge from experience.

Under a biological point of view, this importance is emphasized e.g. by the organization of sensorimotor functions and the distributions of body parts on the primary motor cortex and primary somatosensory cortex [13], where haptic stimuli are mainly processed. As it shown in figure 1, a consistent portion of human cerebral cortex is dedicated to fingers and hand, and haptic sense is predominant within the sensorimotor functions. Consequently, it is not surprising

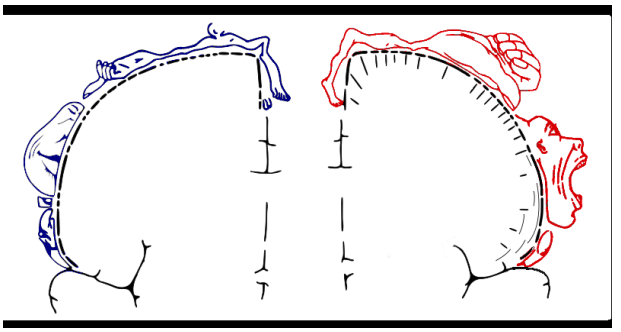

Figure 1: Human cerebral cortex: visualization of sensory functional areas (on the left) and motor functional areas (on the right).

that touch is an extremely complex and heterogeneous information generator with a large number of functions and sensors. Indeed, when an object is haptically explored, information about texture, hardness, weight, shape, size and thermal properties are conveyed, thus producing a manifold perception. Trying to reproduce all these dimensions by means of haptic interfaces is a daunting task. What is challenging is to individuate some suitable projections into adapted perceptual subspaces, which can approximate (and reduce) this complexity and furnish design compromises between feasibility, costs and quality of haptic stimuli to be rendered.

Motivations. Nowadays haptic interface design can be complex (and sometimes unsatisfactory) according to the perception to be reproduced. This thesis aims at simplifying it (and improving it), with minimum loss of information, taking inspiration from neuroscientific studies that in the last twenty years have investigated the complex biomechanical and neural apparatus of the human hand.

The main finding shared by all these studies is that, despite hand complexity, simultaneous motion and force of the fingers is characterized by coordination patterns that reduce the number of independent degrees of freedom (DoFs) to be controlled [14]. This experimental evidence, which can be explained in terms of central (neural inputs are shared by different units acting on different digits) and peripheral (e.g. interconnections between tendons of hand muscles) constraints in the neuromuscular apparatus, describes well the concept of *hand synergies*, (synergy, from Greek *work together*) i.e. broadly, the aforementioned covariation schemes observed in digit movements and contact forces.

A very important geometrical interpretation can be drawn from these results: i.e. for a wide range of hand behaviours, the kinematic space of the hand has a smaller dimensionality than the one represented by its mechanical degrees of freedom. In a certain sense, synergies can be regarded as *maps* [15] between the higher dimensional redundant complexity of purely mechanical architecture of the human hand and the lower dimensional control space of the action and performance, where it is possible to individuate kinematic and kinetic primitives. Following this geometrical interpretation, dimensionality reduction techniques such as principal component analysis (PCA) have been often exploited to quantify and define synergies from a set of hand configurations, for example in grasping tasks [16]. Under a kinematic point of view, in [16] authors demonstrated that a few linear combinations of the measured DoFs of the hand can explain most of the variance contained in the original set of hand postures. Moreover, while lower order PCs (or *postural synergies*) are able to describe basic finger motion patterns, the higher order PCs are mainly

responsible for finer hand adjustments. Using the concept of basis from the theory of vector spaces, it is possible to regard these PCs as a number of linearly independent elements that are able to generate all members of a given set. According to the number and type of these elements (i.e. the level of truncation of the basis), a series of *inner representations of the hand* [16, 17] of increasing complexity can be individuated.

In robotics, the concept of synergies has then been adopted to define simplified manners for the design and control of artificial hands [18–21], using a reduced number of input controls.

An interesting dual application of the aforementioned concepts might be extended to the haptic sensing domain, in order to find maps between the higher-dimensional redundant space of elemental sensory variables involved in the mechanics of touch and the lower dimensional space of perceptual primitives, i.e. "what we actually feel". An attempt to accomplish this goal was reported in [22], where authors hypothesized the existence of a sort of *sensory synergy* basis. The elements of this basis can be regarded as tactual perception manifold projections into constrained subspaces, the latter ones individuating increasingly refined approximations of the full spectrum of haptic information. Also *feature saliency* paradigm described in [23] for the individuation of the predominant characteristics in haptic shape perception can be interpreted as an attempt to reduce haptic information redundancy.

In [24] it was investigated the existence of a *plenhaptic function* for determining the dimensionality of haptic perception. This function is the dual of the plenoptic function [25], defined in the visual domain to indicate the number of coordinates necessary to describe all possible sensorimotor interactions. The plenhaptic function can be regarded as the complete characterization, under a mechanical point of view, of the haptic experience; in terms of vector basis, it comprises all the elements necessary for an exhaustive description. Furthermore, the author noticed that even if the number of coordinates needed to describe mechanical interactions in haptics is larger than three or four,

human touch-related experience seems to take place in a lower dimensional space; i.e. nervous system produces nearly instantaneous reduction of dimensions, to convert a complex problem into a manageable set of computational tasks. Tactile illusions, for example, can be interpreted as the results of these low dimensional simplifications of the plenhaptic function – sampled in time and space – related to motoric and sensory capabilities.

In softness discrimination, a possible reduction of dynamic, force-varying tactile information operated by nervous system can be described by *tactile flow* paradigm [26, 27], which extends Horn and Schunk's equation [28] for image brightness to three-dimensional strain tensor distributions. Tactile flow equation suggests that, in dynamic conditions, a large part of contact sensing on the finger pad can be described by the flow of strain energy density (SED) (or Equivalent von Mises Stress), since Merkel-SA1 afferents, which are primarily responsible for dynamic form in tactile scanning, were proved to be selectively sensitive to these scalar quantities [29]). However, only the flow components that are tangent to the iso-intensity curve itself (i.e. components perpendicular to the intensity gradient) can be determined, as it results from the constraint equation. This intrinsic ambiguity (the same exhibited also by optic flow) can generate hypotheses on some tactile illusions, which were also psychophysically demonstrated [27]. These illusions can be interpreted in terms of information loss due to projections into a lower dimensional space, as it was also discussed w.r.t. plenhaptic function [24].

Moreover, the integral version of tactile flow equation can be used to explain the *Contact Area Spread Rate (CASR)* [30] experimental observation, which affirms that a considerable part of tactile ability in object softness discrimination is retained in the relationship between the contact area growth over an indenting probe (e.g. the finger pad which presses the object) and the indenting force itself.

These suitable approximations and reductions of haptic information manifold can suggest new strategies to build haptic interfaces. For example, recognizing that a simple force-area relation describes a

large amount of cutaneous information involved in softness discrimination by probing has inspired the development of simpler and more effective haptic displays for human-computer interaction, e.g. [30]. In general, motor and sensory synergy concepts can be exploited to advance the state of the art in artificial systems, by learning from human data and hypotheses-driven simulations.

Thesis Contributions. In this thesis I define models and methods to convey haptic stimuli and design haptic devices and active touch sensing instruments, by following the above described geometrical, synergy-based reduction. More specifically, I adopt this approach in relation with the two main functions of haptic perception, cutaneous information (which is mainly related to the mechanical deformation of the skin) and kinaesthesia (which indicates the internal sensing of force, displacements and posture processed inside joints, muscles, tendons and skin). This classification suggests an organization of this work in three parts.

After a brief introduction about the two haptic modalities and their rendering, in the first part I consider the problem to define primitives for the design of tactile displays. More specifically, considering softness discrimination and possible reductions of the involved tactile information (tactile flow equation), I discuss the design of a fabric-based softness display [A1, A2] inspired by Contact Area Spread Rate hypothesis. Subjects interact with this display touching a deformable surface which is naturalistically modelled under their fingertip, therefore their capability of tactually perceiving softness appears to be increased compared with the one offered by a discrete CASR-based pneumatic device previously developed in [30].

Afterwards I analyze the problem to find simple conceptual primitives to vehiculate information about stiffness and geometry of hard lumps (cancer) embedded in soft tissues. This information has to be conveyed to surgeons during palpation tasks performed in Robot-assisted Minimally Invasive Surgery (RMIS). A commonly explored solution to this problem has involved various forms of pin-based tac-

tile arrays [31–33]. These devices can recreate a broad range of stimulus perceptions upon the finger pad, but their somewhat bulky size [34] and complex electromechanical design do not satisfy the requirements for implementation on a typical robot-assisted surgical system; namely, a practical system must be simple in design, occupy an extremely small footprint, and not impede the motion or dexterity of the master manipulators. Moreover, few studies have demonstrated tactile displays capable of integration within an RMIS system, largely because the size and weight constraints of RMIS motivate a more targeted approach. To overcome these limitations, it is possible to perform a reduction from the higher dimensional space of technological solutions so far adopted to a lower dimensional space. In this space, the design can be simplified by relating the technology exploited for stimulus rendering to "what we actually feel" in a more direct and natural manner. Therefore, a pneumatic air-jet approach is proposed, in which pressurized air is directed to the finger pad through a small circular aperture, creating a somewhat hemispherical "lump-like" indentation upon the finger pad. This idea was previously explored in [35], but not rigorously tested quantitatively or evaluated psychophysically. Here, I describe the psychophysical characterization and fluid dynamics modelling [A3] of an air-jet-based method, which has then been implemented in a tactile display [A4]. This work was developed in collaboration with James C. Gwilliam, a Biomedical Engineering PhD candidate from Johns Hopkins University School of Medicine, who equally contributed to it, and will be included also in his PhD dissertation. This collaboration refers to my visiting period (January-June 2011) at the Laboratory for Computational Sensing and Robotics (LCSR) - Johns Hopkins University, under the supervision of Prof. Allison M. Okamura (Research Professor in the Department of Mechanical Engineering and Vice Chair, Johns Hopkins University till June 2011; from July 2011, Associate Professor in the Department of Mechanical Engineering, Stanford University).

In the second part, I deal with the issue for a correct pose estimation with active touch sensing systems, analyzing how artificial kinaes-

thetic rendering of hand posture can be simplified by means of hand synergy concept. Up to now, *kinematic synergies* have been mainly used for the design and control of under-actuated robotic hands. This concept can be easily extended to the *observability* domain; i.e. if a reduced number of degrees of freedom is sufficient to control a human or artificial hand, it is reasonable to assume that a subset of measured hand DoFs is sufficient to guarantee a correct pose estimation as well. This idea was pioneered in [36] where postural synergies for grasping were exploited to animate a whole human hand avatar. In this thesis I follow an optimal estimation approach to solve the problem of human hand posture reconstruction using *sensing gloves*. Sensing gloves for hand tracking and configuration measuring are widely adopted in many applications fields like, for example, virtual reality, musical performance, video games, tele-operation and robotics, since they offer useful interfaces for human-machine and haptic interaction. However, the widespread commercialization of these systems imposes limits on the production costs and affects the quality of measurements, which can be limited under several regards. They can be generated through an imperfectly known model, can be subject to noise, and can be less than the number of degrees of freedom of the hand. Under these conditions, direct reconstruction of the hand pose is an ill-posed problem, and performance is reduced.

To obtain an acceptable level of accuracy without modifying the glove hardware, hence basically at no extra cost, I propose to use the information on most frequent human hand poses, as represented in a database of postural synergies for grasping built beforehand [16]. By following a minimum variance estimation approach (MVE), such an *a priori* information is fused with glove data in a consistent way, so as to provide a good hand pose reconstruction in spite of insufficient and inaccurate sensing data [A5].

As a second step, I analyze the problem of optimal glove design [A6]. Synergies-driven optimization leads to define, for a fixed number of measures (usually noisy and inferior to the mechanical kinematic space of the hand) and for a given *a priori* database, the

best linear combinations of DoFs as well as single DoFs of the hand model to be measured, which are able to maximize the knowledge on the whole hand posture. Simulations and experiments are reported which demonstrate the effectiveness of the proposed techniques.

In the third part, generalizing the "synergies as a basis" description [22] for softness discrimination, I venture to speculate about kinaesthesia and cutaneous sensing as the two main synergies of the *haptic synergies basis*, which completely describe the mechanics of touch and its perception. Moreover, in softness discrimination a gradient was found [37], whereas cutaneous cues are predominant, even if both the modalities are necessary to get precise perceptual information. Here, I study the problem of the fidelity by which softness can be artificially rendered with the number of "synergies" (i.e. kinaesthesia and cutaneous cues) employed in rendering [A7, A8]. This analogy is coherent with the idea that a large number of motor synergies is required to accomplish increasing complex motor tasks [16]. Therefore, I realized conceived specimens which can convey identical kinaesthetic but different cutaneous stimuli, or the other way around, asking subjects to probe them for softness. Results indicate that unimodal (i.e. when either modality is present by itself) touch alone is not sufficient to enable a satisfactory discrimination of softness, and that more elements of tactual information are necessary to elicit a more exhaustive perception. With this as a motivation, I discuss the implementation and control of an integrated device, where a conventional kinaesthetic haptic device is combined with a cutaneous CASR-based softness display. I investigated the effectiveness of the integrated display via a number of psychophysical tests and compared the subjective perception of softness with that obtained by direct touch on physical objects. Results show that the subjects interacting with the integrated haptic display are able to discriminate softness better than with either a purely kinaesthetic (basically a force display) or a purely cutaneous display (which conveys force, contact and shape information to the skin).

Chapter 1

Real Touch and Rendered Touch

The sense of touch is an astonishingly complex and heterogeneous information generator. This information is essential for humans, and animals in general, to properly perceive and interact with the environment, and hence to survive. As Aristotle affirmed in his *de Anima*: *Without touch it is impossible for animal to exist...the loss of this one sense alone must bring death.* Therefore, haptic perception represents a rich information manifold, as it results from the integration and processing of a wide number of signals from measurement locations and sensors distributed through human body. Even if thermal and pain information is also provided, haptics is mainly a mechanical sensory system. Various types of sensors can be individuated referring to the two fundamental functions of human nervous system which play a primary role in haptics: kinaesthesia and tactile (or cutaneous) sensing.

Tactile receptors (*mechanoreceptors*) can be found in the outer areas of glabrous and hairy skin, usually in exposed positions (e.g. fingertips). More specifically, these receptors are mainly located in the dermis[1], a fibrous layer which supports the epidermis, the outermost layer of the skin (where it is possible to find primarily protective horny structures, such as stratum corneum) [39]. Mechanoreceptors

[1] or in the dermo–epidermal junction [38]

basically react on the strains of the skin and their reaction can be proportional to velocity, acceleration or elongation [40]. Under a neurophysiological point of view, the classic manner to classify the sensory endings in the mammalian skin distinguishes between slow and fast adapting receptors [38]. Slow Adapting (SA) receptors exhibit a response during both the initial phase of the stimulus and steady pressure; fast (or Rapid) Adapting (RA) ones respond only at the onset of the mechanical indentation of the skin. Hereinafter, following classic engineering naming, the words receptors and sensors are used as synonyms. There are three typologies of SA receptors, which can be grouped in Type I receptors – which respond if the skin is stroked rapidly – and Type II – which respond to a constant displacement of the (stretched) skin – described as it follows [29, 38]:

- slow adapting Type I (SA1) afferents that end in Merkel cells. These receptors are distributed just beneath the epidermis. In response to a sustained indentation they exhibit a sustained, slowly adapting discharge, linearly related to the indentation depth. SA1 receptors are selectively sensitive to points, corners, edges and curvature as a consequence of their selective sensitivity to Strain Energy Density (SED) or closely related quantities (e.g. Equivalent von Mises Stress). For this reason and because of their high spatial resolution (0.5 mm in a receptive field with 2-3 mm diameter), SA1 sensors are able to transmit an acute spatial neural image of a tactile stimulus;

- slow adapting Type II afferents (SA2) that are thought to end in Ruffini corpuscles. The Ruffini corpuscles located in the deep tissues of the dermis have a relatively large spindle shaped architecture. They are two-four times more sensitive to skin stretch and six times less sensitive to displacement than SA1 afferents, thus transmitting a neural image of skin stretch to the central nervous system, with a minimized interference from eventual objects held in the hand;

- C-mechanoreceptors, with unmyelinated C-fibres originating from

the dermis. There is no differentiated sense endings associated with them. These sensors respond to steady indentation of the skin producing a slowly adapting discharge. However, C-fibres produce responses also to non mechanical stimuli, such as temperature and tissue damage.

On the contrary, rapid adapting receptors are defined as:

- rapidly adapting afferents that end in Meissner corpuscles. These relatively large cell assemblies distributed in the dermal ridges just beneath the epidermis, only in primate glabrous skin, are insensitive to static skin deformation but four time more sensitive to dynamic skin deformation than SA1 receptors, with larger receptive field but with lower spatial resolution;

- Pacinian afferents that end in Pacinian corpuscles. Pacinian corpuscles lie in the deeper tissues of the dermis in both glabrous and hairy skin and are sensitive to deformation in the nanometer range, with low spatial resolution and a receptive field that can include the entire hand. They also exhibit an intense filtering of low-frequency stimuli which could affect Pacinian sensitivity. Even if single afferent is not able to represent in an accurate manner the waveform of a complex stimulus, a whole Pacinian population which fires randomly can provide a good representation;

- Hair Follicle Receptors, i.e. the complex meshwork around hair follicle consisting of sensory nerve endings. They respond to any movement of the hair.

A more exhaustive description of these receptors and their functions can be found e.g. in [29, 38].

Let consider now kinaesthetic sensing. The word kinaesthesia was used for the first time by Bastian [41] in 1888, to indicate the intrinsic capability to sense the position of our limbs and trunk. Moreover, an other object of kinaesthesia is the state of contraction and or/tension

of body's muscles. This sense hence basically consists on force and displacement processing and can be seen as a "mysterious sense"; indeed, humans are generally unaware of it and the sensation it provides is hardly identifiable.

For this reason there is an ongoing debate – the so called debate on the *sensation of innervations*, which raged from 19th century – on which factors (and how they) contribute in an effective manner to produce kinaesthetic perception. Indeed, while for much of the 20th century it was assumed that receptors for joint positions and movements were located at the joints themselves, today, after the groundbreaking observations in [42], it is accepted that the primary role in kinaesthesia is played by muscle spindles with additional important contributions from skin and signals of central origin and very minor contributions from joint receptors (which, under some circumstances, can provide kinaesthetic inputs when signals from muscles and skin are not available [43]).

Therefore, the leading kinaesthetic receptor is the muscle spindle, which consists of a primary ending (responding to the size of muscle length change and as well as its speed) and secondary ending (which sense only position, with no velocity-related responsiveness) [44]. They are primary sensitive to vibration; however a significant contribution in kinaesthesia is provided also by passive tension in muscles [45].

Other contributions to kinaesthetic perception can come from some cutaneous receptors, the most likely is the skin stretch receptor, i.e. the slowly adapting Type II receptors served by Ruffini endings [46–49]. Indeed, it was demonstrated that when the skin of the hand over proximal joints is stretched and muscle vibration is applied, the movement illusions which arise from this stimulation are greater than when either stimulus is present by itself [50]. The conclusion that authors drawn from this finding is that cutaneous receptors contribute in an independent manner to kinaesthesia. Other observations have been done to further sustain this conclusion. For example, it was shown an occluding action of skin signals from local rapidly adapting receptors;

when these receptors are stimulated by low-amplitude high-frequency vibration, their response can affect the detection itself of the movements [51]. Furthermore, a fundamental role in kinaesthesia is played by those skin receptors located in the position adjacent finger joints, to disambiguate muscle afferent information. Indeed the latter information involves multiple joints; on the contrary, the proximity of the receptors adjacent to each joint enables for joint-specific sensing [50].

For a more exhaustive review of kinaesthetic receptors and their functionality see e.g. [45].

The aim of this biological introduction is to provide a concise description of these cutaneous and kinaesthetic sensors, since the correct understanding of their functionality will be important to introduce some aspects and considerations in next chapters. At the same time, this description should underline the complexity that characterizes tactual information manifold generated by the mechanics of touch.

What is noticeable from this brief description is that kinaesthesia and cutaneous sense are complex and strictly related each other. Indeed, some sensing elements can play an important role in both the haptic modalities. Under an engineering point of view, classification between kinaesthesia vs. tactile sensing has been usually adopted to describe haptic interfaces [11]. In general kinaesthetic systems can be *impedance* devices (they sense the position of the operator and then apply a force vector to her/him in order to match a proper deflection of the rendered object) or *admittance* devices (they sense operator's force and constrain her/his position to mimic rendered object deflection). Commonly used haptic devices are e.g. Phantom Device (Sensable, Wilmington, MA, USA) or Delta Haptic Device (Force Dimension, Nyon, Switzerland), see figure 1.1.

These kinaesthetic devices primarily act as force displays, although an inherent cutaneous sensation is provided through the contact with the device tool.

On the contrary, tactile displays are purposely used to stimulate skin, by conveying to it force, contact and shape information. They are developed for a specific purpose, such as display of local shape,

Figure 1.1: Phantom Desktop Device by Sensable (on the left) and Delta Haptic Device by Force Dimension (on the right).

shear or softness, see figure 1.2. Given the variety of cutaneous sensors with different characteristics and sensitivity, it is particular challenging to properly design tactile displays able to render realistic contact information.

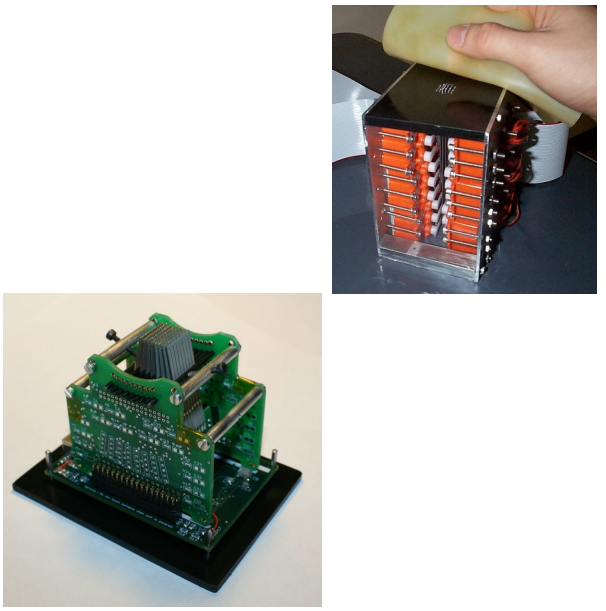

Figure 1.2: Latero Tactile Display by Tactile Labs [52] (on the lower left) and the 36 pin tactile shape display [53] (on the upper right).

Ideally, for touch to be real, it would be necessary to design haptic devices which should be able to reproduce each dimension of tactual sensation. However trying to render all these dimensions is a daunting tasks. Finding lower dimensional projections, that I will argue to refer to as *perceptual synergies* according to the concepts described in the Introduction, as well as suitable geometric reductions of design complexity, suggested e.g. by *hand kinematic synergies*, might lead to an useful trade-off between feasibility and quality of rendering. In next chapters, following the kinaesthesia/cutaneous sensing classification, I mainly focus on three types of haptic and artificial systems:

I tactile displays:

softness display;

lump display for Robot-assisted Minimally Invasive Surgery;

II active touch systems for gesture measurement, mainly relying on kinaesthetic perception;

hand pose sensing glove performance enhancement;

hand pose sensing glove optimal design;

III integrated device, where a conventional kinaesthetic haptic device is combined with a cutaneous softness display.

Part I

Cutaneous Cues: Softness Display and RMIS Applications

Chapter 2

Softness Displays: from Tactile Flow to Contact Area Spread Rate Paradigm.

Softness is the subjective measure of the *hardness* and *compliance* of an object. When an object is haptically explored, among the various types of information that can be conveyed, the material properties of hardness and texture appear to be of particular importance. According to [54], hardness, together with texture and thermal conductivity, is the maximally available dimension for processing after initial contact because, as opposed to geometric properties, they do not need to be coded with reference to a coordinate system. Indeed, it was observed that material properties provide faster perceptual access than the geometric properties of size and shape [55]. Further behavioural [56, 57] and neuroimaging [58] studies found out that, while remembering or imagining geometric features of an object evokes visual imagery, the interrogation of material features evokes the processing of semantic object representations. This suggests that these are fundamentally tactual-related properties, not easily accessed via vision or visual imagery.

In [37] human capabilities in tactual discrimination of softness were studied in order to isolate the involved information-processing mechanisms. The main findings of this work can be summarized as:

- tactile information alone is sufficient in softness discrimination for objects with deformable surfaces, since the spatial pressure distribution within the contact zone is dependent on both the force applied and the specimen compliance;
- on the contrary, kinaesthetic information alone is not sufficient for softness discrimination of objects with deformable surfaces;
- for compliant objects with rigid surfaces, the pressure distribution and skin deformation are independent of object compliance. As a consequence, both types of information are necessary to have a correct perception.

Given that cutaneous sensing has a predominant role in softness perception, I mainly focus on the mechanics of tactile information, analyzing hypotheses on how the nervous system can cope it.

When a fingertip (or other tactually endowed parts of the body) enters in contact with an object, a complex mechanical interaction occurs, which generates tactile stimuli for the various mechanoreceptors. However, even if tactile information is extremely rich in content and purposes, it might be not the case that all its richness is actually necessary to discriminate softness of different materials. Therefore, it is possible to argue about lower-dimensional projections of tactual information manifold, which may provide conceptual models of how softness information can be elicited from raw sensor data. These models should enable for a tractable, yet meaningful analysis, and hence driving the design of more effective softness displays.

Using simple mechanics, let $p(x)$ be the pressure exchanged at point x on the contact surface between two deformable bodies, and let the resultant contact force be denoted by P. Clearly, P equals the integral of $p(x)$ over the contact area A. Let also δ denote the overall (rigid) relative displacement between the two bodies, i.e. the relative

displacement of two reference frames attached to the two bodies in positions as remote from contact as not to be subject to any deformation. The displacement δ is set to zero in the relative configuration where the contact is first established. The resultant force P and rigid displacement δ are already very simple and useful abstractions of contact mechanics. Indeed, observing the process of tactile probing for softness discrimination, the relationship between their evolutions provides a direct and very relevant information on softness - analogous to the macroscopic force-displacement curve which characterizes deformability of material samples. Given that sensing resultant forces and kinematic motions are primary objects of kinaesthesia, the P/δ curve of a fingertip/object pair can be considered as the (abstract) content of kinaesthetic information elicited by probing for softness.

Furthermore, under a cutaneous point of view, contact pressures and displacements on the fingertip surface generate a distribution of stress and strain tensors in the dishomogeneous, anelastic material whose accurate modelling is very difficult. However, mechanoreceptors involved in softness discrimination (mainly SA1-Merkel corpuscles) appear to be predominantly sensitive to a single scalar mechanical parameter, the Strain Energy Density (SED). This specific sensitivity was used to define the following hypothesis about how nervous system operates to reduce tactile information for softness discrimination into a manageable computational model.

2.1 Tactile Flow Hypothesis

Tactile flow paradigm [26] can be regarded as the tactual 3-dimensional counterpart of the 2-dimensional optic flow model [28] for processing dynamic tactile stimuli, which would gather information about softness discrimination, shape recognition and relative motion between fingertip and explored object.

Let $\mathcal{E}(\xi, P)$ denotes the SED at a point ξ within the volume V_F occupied by the deformed object of reference, under a given resultant

force P (this relates to a specific pair finger pad/object, which is henceforth assumed to be given). $\mathcal{E}$ is defined as

$$\mathcal{E} = \frac{\sqrt{2}}{2} \cdot \sqrt{(\sigma_1 - \sigma_2)^2 + (\sigma_2 - \sigma_3)^2 + (\sigma_3 - \sigma_1)^2} = \sqrt{2} \cdot \sqrt{\tau_1^2 + \tau_2^2 + \tau_3^2} \tag{2.1}$$

where σ_1, σ_2 and σ_3 are the principal stresses and τ_1, τ_2 and τ_3 are the principal shear stresses. Consider now the locus of points within the volume V_F which have the same SED value. For instance, by $\Sigma_i = \left\{\xi \in V_F | \mathcal{E}(\xi, P) = \mathcal{E}_i\right\}$ will be denoted the iso-SED surface whose points have SED equal to $\mathcal{E}_i$. Assume that, from this condition, the resultant force P is changed to $P + \Delta P$: as a consequence, the SED will change at points within V_F. If for instance P is slightly increased in magnitude, it can be expected that the SED for points previously belonging to Σ_i will also increase. From another point of view, the surface Σ_i can be considered as it moves, under the new load conditions, to points that are farther away from the center of the contact region. To describe how an iso-SED surface moves across the volume V_F, a simple differential equation for the conservation of SED, analogous to optic flow equation in the form, is produced

$$\frac{d\mathcal{E}(\xi, P)}{dP} = 0 \tag{2.2}$$

and, by expanding the total derivative,

$$\frac{\partial \mathcal{E}}{\partial \xi} \frac{\partial \xi}{\partial P} + \frac{\partial \mathcal{E}}{\partial P} = 0 \tag{2.3}$$

or

$$\nabla \mathcal{E}\, \vec{\phi} = -\frac{\partial \mathcal{E}}{\partial P} \tag{2.4}$$

Here, $\nabla \mathcal{E} = \frac{\partial \mathcal{E}}{\partial \xi}$ is the spatial gradient of $\mathcal{E}$, i.e. a vector normal to the surface in ξ, and $\frac{\partial \mathcal{E}}{\partial P}$ is the differential change in SED which is obtained by measuring it at point ξ before and after applying the infinitesimal load change dP. Finally, the vector $\vec{\phi}(\xi) = \frac{\partial \xi}{\partial P}$ denotes the infinitesimal motion of a surface element in Σ_i, and will be referred to as the

flow of SED in the finger pad associated to the load change. Time-varying excitation of SED-sensitive mechanoreceptors embedded in V_F is thus directly related to the SED flow through their location, which might in turn be related to the perception of the spatial direction in which stimuli evolve. Notice that, analogously to optic flow equation, tactile flow equation exhibits an intrinsic ambiguity since it defines the 3-dimensional flow vector $\vec{\phi}$ only up to a 2-dimensional subspace (the tangent space to Σ at ξ)[1].

Moreover, as it was suggested in [26], the rate of expansion of iso-SED surfaces can be related to the rate of the expansion of contact area under increasing load. Therefore tactile flow computational model can be associated to the experimental paradigm of the Contact Area Spread Rate (CASR) [30].

2.2 Experimental CASR

In [30], it was conjectured that, despite of the extreme richness of tactile manifold, *a large part of haptic information necessary to discriminate softness of objects by touch is contained in the law that relates resultant contact force to the overall area of contact, or in other terms in the rate by which the contact area spreads over the finger surface as the finger is increasingly pressed on the object.*

This relationship is the so-called Contact Area Spread Rate (CASR); in [30] authors also ventured to hypothesize that the *area* of the zone itself is more relevant for softness discrimination than the actual *shape* and *location* of the contact area. As further motivation for this observation, standard Hertz theory for contact modelling between elastic bodies was exploited [59, 60]. This theory provides a simple model of the contact since it applies to homogeneous, isotropic bodies which have dimensions larger than that of the contact area, and usually that is not the case in common finger pad-object interactions. However it

[1]This ambiguity can provide an explanation for perceptual illusions psychophysically observed in tactile domain [27]

is useful to give a preliminary explanation of the phenomenon. In

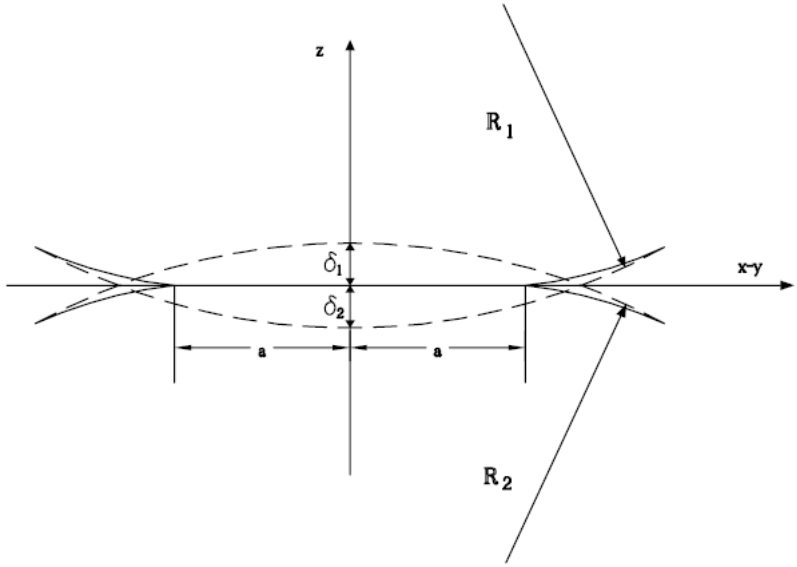

Figure 2.1: Two bodies in contact according to Hertz theory.

case of contact between two spheres, the shape of the contact area is circular with radius a, and the relative displacement of corresponding points of objects by within the contact area is

$$\bar{u}_{z1} + \bar{u}_{z2} = \delta - \frac{r}{2R^2} \tag{2.5}$$

with $\delta = \delta_1 + \delta_2$ representing the relative displacement, r the radial distance from the center of contact and $\frac{1}{R} = \frac{1}{R_1} + \frac{1}{R_2}$ defines the relative curvature. The resultant pressure distribution is obtained as

$$p(r) = p_0 \cdot [1 - \left(\frac{r}{a}\right)^2]^{\frac{1}{2}} \tag{2.6}$$

where p_0 is the pressure value at the center of the contact, while the displacements by within the contact area are given as

$$\bar{u}_{zi} = \frac{1 - \nu_i^2}{E_i} \cdot \frac{\pi p_0}{4a}(2a^2 - r^2) \tag{2.7}$$

with $r \leq a$ and ν_i, E_i indicate the Poisson coefficient and Young Modulus of the two specimens in contact, respectively. After some algebras the radius a is obtained as

$$a = \frac{\pi p_0 R}{2E^\star} \tag{2.8}$$

where $\frac{1}{E^\star} = \frac{1-\nu_1^2}{E_1} + \frac{1-\nu_2^2}{E_2}$.

Computing the total force involved in the contact P as

$$P = \int_0^a p(r) 2\pi r \, dr = \frac{2}{3} p_0 \pi a^2 \tag{2.9}$$

it can be found that the contact area A is related to the force P as

$$A = \pi \cdot a^2 = \pi \left(\frac{3PR}{4E^\star} \right)^{\frac{2}{3}} \tag{2.10}$$

Obviously CASR paradigm depends also from the geometrical properties of the specimens, even if this dependence is assumed to be weaker than the one with the elastic parameters (i.e. E_i and ν_i) [30]. Varying elastic parameters yields to different rates of spread of the contact area A with the contact force P.

Recognizing that a simple force P vs area A relation describes a large amount of cutaneous information involved in softness discrimination by probing has inspired the development of new compelling tactile displays.

2.3 First Discrete CASR-based Display

In [30] a prototype CASR display was also presented. Its role is to mimic the rate at which the contact area of the probed material grows over the surface of the probing finger pad. The implementation proposed in [30] consists of a set of cylinders of different radii, assembled in telescopic arrangement (see figure 2.3). Because of the disconti-

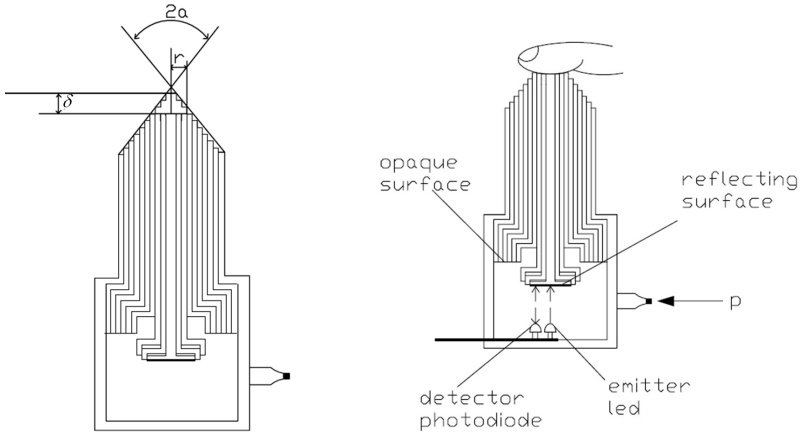

(a) Elements of the display (b) Geometry of the display

Figure 2.2: CASR display scheme.

Figure 2.3: The discrete prototype CASR display.

nuity in the structure due to the cylinders, this CASR display will be hereinafter referred as *discrete CASR display*. A regulated air pressure is inflated inside acting on one end of the cylinders according to the desired force to be perceived by subjects during indentation (see figure 2.2). Pressure is applied on all the cylinders. When the subject finger probes the display, pushing down against the cylinders, it comes into contact with a surface depending on the height of the cylinders

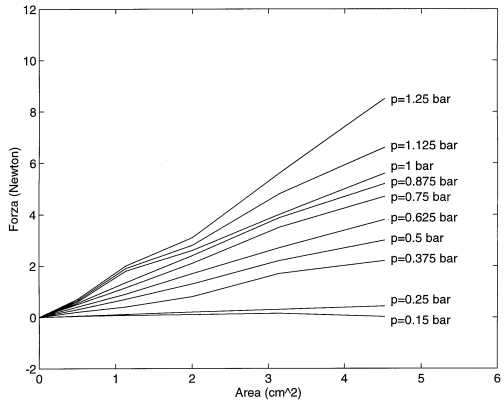

Figure 2.4: Experimental force-area curves of the prototype CASR display with constant pressure.

themselves and perceives a resultant force correlated to the pressure. The length of the cylinders is chosen such that, when the operator exerts no force, the active surface of the display can be approximated in a stepwise manner as a cone whose vertex has a total angle of $2a$. After the finger is pushed down by an amount of δ, the contact area A can be approximately computed as $A(\delta) = \pi\,\delta^2\,tan(\delta)^2$. Consequently, the resultant force P which is opposed to the finger is $P(\delta) = pA\,(\delta)$, with p is the pressure to be provided to the inner chamber by the external pressure regulator. In this prototype, the displacement δ can be measured with an optoelectronic sensor or a proportional Hall sensor placed at the bottom of the chamber. In [30], it was proved, by means of several psychophysical experiments, that the discrete CASR display is able to provide better performance in softness discrimination than the one achieved using a purely kinaesthetic display (i.e. the discrete CASR display covered with a hollow cylinder).

From figure 2.4 what is noticeable is that the experimental curves P/A obtained for the discrete CASR display, at a fixed pressure, are

linear; to mimic real object CASR curves, typically nonlinear, the display has to be controlled in feedback acting on the variable p. In Chapter 5, I will illustrate a control strategy based on the principle of virtual work.

2.4 A New CASR-based Display: the Fabric Yielding Display (FYD)

So far I have described the discrete CASR display which is able to replicate a desired force-area curve, enabling for a more realistic softness perception than the one achieved with a purely kinaesthetic device. However, the structure of this display does not provide subjects with a continuously deformable surface. This fact, especially for tele-operation applications, could lead to a not completely immersive experience due to edge effects. Moreover, the contact area involved in the interaction can be known only after some geometric considerations related to the measured displacement. To mimic in a more efficient manner real CASR curves, a real-time accurate measurement of the contact region represents an important requirement.

To overcome the aforementioned limitations, I propose a fabric-based display which allows subjects to interact with a deformable surface at different levels of stiffness[2]. In recent years, the role of the exploration of both real and virtual textiles and fabrics has became an important topic in haptic research [61–64]. For example HAPTEX Project [65] combines research in the field of haptic interfaces and textile simulations with the final objective of providing a virtual reality system for multi-point haptic interaction with a real-time simulated virtual fabric. To achieve this purpose, mechanical and physical parameters of textiles have to be evaluated. Here, I exploit the bi-elasticity of a real fabric to convey both cutaneous and kinaesthetic information; at the same time, a direct measurement of the contact

[2]The terms stiffness and compliance are here used as synonyms.

area involved in the interaction between the fingertip and the object is also provided.

2.4.1 FYD: Structure Description and Functionality Explanation

The here proposed system, called hereinafter FYD (Fabric Yielding Display) [A1, A2] is based on a layer of bi-elastic fabric which can be touched by subjects with their forefinger. Bi-elastic means that the fabric exhibits properties which render it elastic in at least two substantially perpendicular directions, and preferably in all directions. By changing the elasticity of the fabric, subjects are able to feel different levels of softness. The FYD prototype is comprised of a hollow plastic cylinder containing a DC motor. A thin layer of bi-elastic square shaped fabric (250×250 mm) is placed on the top of the hollow cylinder and it is tied to a circular crown which can run outside along the cylinder, with a minimum friction. When the motor pulls down the crown, the fabric is stretched and its apparent stiffness increases. Conversely, when the motor pushes up the crown, the fabric is relaxed and it is felt softer. The FYD also behaves like a contact area display, by suitably processing signals coming from a couple of photo-devices. A view of the display is reported in figures 2.5 and 2.7.

The FYD prototype is 300 mm high and 60 mm wide in diameter and consists of three sections (see figure 2.6:

1. Motor section (80 mm high). The motor is controlled using a Sabertooth Syren10 dual motor driver (Dimension Engineering, Akron, OH, USA). This driver allows to get a bidirectional rotation of the motor. Using the National Instrument (Austin, TX, USA) DAQ card PCI6036E, it is possible to acquire the position of the crown with an external potentiometer connected to it, and, consequently, apply the input voltage to the motor in order to reach the desired position, i.e. the desired stretching state of the fabric (see Section 2.4.2);

Figure 2.5: The FYD system: starting from the left side, it is possible to see the electronic box, which contains the motor driver and the DAQ card, the FYD prototype and a computer to control the system.

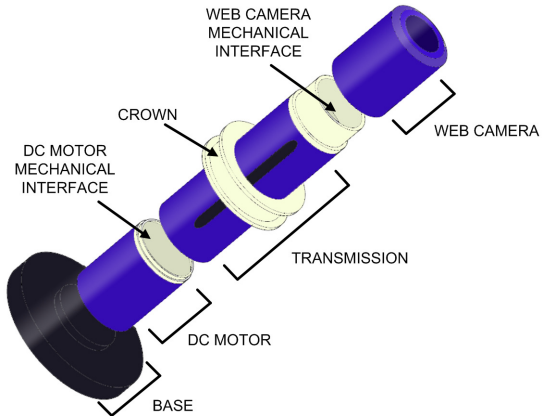

Figure 2.6: External view of the prototype. The potentiometric sensor connected to the crown is not reported to enable for a better visualization.

2. Transmission section (160 mm high). The transmission system converts the rotational movement of the motor into the translational movement of the crown. The system consists of a screw-female screw, the latter is attached to the crown by means of three, 120° spaced, metallic supports. They are moved with the

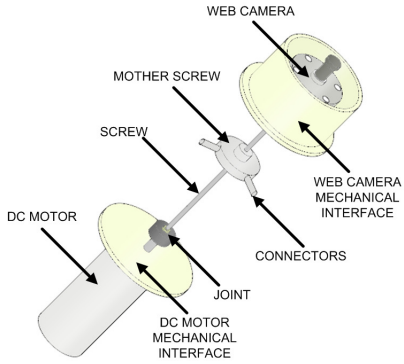

Figure 2.7: Prototype internal view. It is possible to see the transmission system and the DC motor position.

crown. The DC motor is connected to the screw with an Oldham joint, which is a homo-kinetic transmission joint, i.e. it is able to transmit the same angular position, velocity and acceleration from an input transmission shaft to an output one. The screw-female screw system is one of the principle mechanical system for linear or translational movement. It is adopted in order to have an acceptable trade-off between the velocity of the crown and the torque necessary to reach a good state of stretching of the fabric. In addition, the screw-female screw system enables for a bidirectional movement of the crown;

3. Web camera section (60 mm high). The camera (whose resolution is 320×240 pixels) is placed inside the hollow cylinder at the center of the mechanical interface, just beneath the fabric. The camera is endowed with high luminosity LEDs and frames the lower surface of the fabric. During the tactual indentation, the fabric is strained and the fabric area which comes into contact with the fingertip changes according to the applied force. The camera allows to acquire the image of the strained fabric and, by means of suitable processing algorithms, the contact area can be estimated (see Section 2.4.3).

The prototype as a whole is connected on a base (15 mm high and 90 mm diameter) in order to guarantee the physical stability.

Several materials (including commercial Lycra®, latex layer, and silicon rubber) were tested to verify their suitability for our purpose. The best performance was provided by Superbiflex HN by Mectex (Erba, Como, Italy) because it exhibits both a very good elastic behaviour with a large range of elasticity and a high resistance to traction.

2.4.2 Control

The control strategy is chosen in order to have a low computational workload and guarantee a real-time functioning.

Control is based on the comparison of two signals (see figure 2.8): Pos_{ref} and Pos_r that are, respectively, the reference position and the current position of the crown read by the potentiometer.

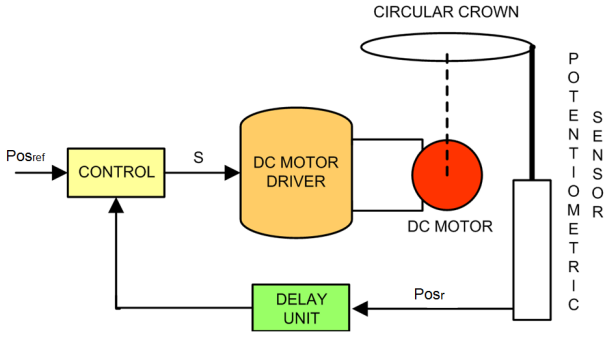

Figure 2.8: Control blocks architecture: Pos_r is the signal acquired by the potentiometric sensor, `S` is the signal produced by the comparison between Pos_{ref} and Pos_r.

The comparison produces a third signal (`s`) for the motor driver activation. In pseudo-code the situation is represented as

`if(`Pos_{ref}`==`Pos_r`){s=0}`

`if(`Pos_{ref}`>`Pos_r`){s=+1}`
`if(`Pos_{ref}`<`Pos_r`){s=-1}`

The signal `s` has three logical levels. When `s` $= -1$ the motor is driven to clockwise rotate, while when `s` $= +1$ the motor rotates counterclockwise. When `s` $= 0$, the DC motor is stopped at the current position. Pos_{ref} is the position of the circular crown, to which a specific level of stretching of the fabric is associated. It is calculated from the characterization curves (see Section 2.4.5). Pos_r is the signal recorded by the potentiometric sensor and gives the current position of the crown. At each simulation step, the control produces the signal `s` and the DC motor is moved until the actual crown position is equal to Pos_{ref}. In figure 2.8 the control block diagram is reported, where the delay unit is put in to prevent algebraic loop when the control starts to run.

2.4.3 Area Acquisition

The FYD system allows to visually display the contact area between the fabric and the finger. A suitable segmentation algorithm gives an estimation of the contact area which is visualized in real time. The contact area acquisition algorithm is based on RGB image binarization. More properly, only one image band (the R band, which is a 320×240 matrix of integer numbers) out of three is involved in the area detection algorithm to avoid a computational workload too high for assuring a real-time processing.

During the tactual probing, the indented fabric surface is closer to the camera with respect to the outer region. Consequently, this area will be more lighted up by the LEDs. The difference between background luminosity and contact area luminosity is discriminated by binarization thresholds (see figure 2.9), which are heuristically calculated. Using a linear interpolation, at each vertical position of the crown a binarization threshold is associated. In this manner, the pixels in the image which belong to the contact area are displayed as

white pixels.

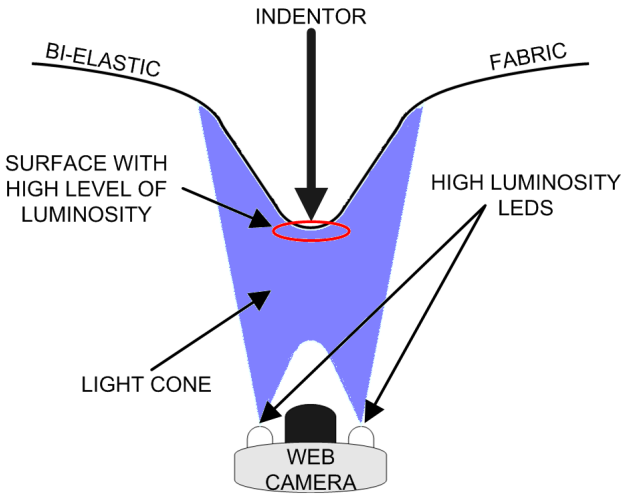

Figure 2.9: Scheme of the area acquisition and the illumination system.

The contact area in [cm^2] is estimated as

$$C_{\text{area}} = N_p \times \frac{A_c}{S_p}, \tag{2.11}$$

where N_p is the number of white pixels belonging to the contact area; A_c is the frame area in [cm^2] and S_p is the web camera resolution (i.e. 320 × 240 pixels). The accuracy of the contact area measurement is crucial because the indentation force and the indentation displacement are indirectly estimated using force-area, $P(A)$, and force-displacement, $P(\delta)$, characteristics. The result of the area detection algorithm is reported in figure 2.10.

2.4.4 Characterization and Interpolation

The device here proposed is controlled in order to simulate mechanical compliance of materials having specific $P(\delta)$ and $P(A)$ curves. By

Figure 2.10: The results of the contact area detection algorithm: the RGB acquisition (on the left side) and the result of the final binarization (on the right side).

exploiting the bi-elasticity properties an acceptably large range of levels of stiffness can be reproduced (from 0.45 N/cm to 2.05 N/cm).

In figure 2.11, the $P(\delta)$ and $P(A)$ curves of the fabric at different levels of stretching are reported. These levels were obtained changing the position of the crown, from 0 mm (0 mm indicates the position of the crown at the top of the cylinder) to 30 mm, with an incremental step of 5 mm. A load-cell was used to measure the force applied on the fabric during the indentation.

Indentation tests were performed by means of a compressional indentor driven by an electromagnetic actuator. The actuator is a Bruel & Kjear (Nærum, Denmark) minishaker, capable of applying a maximum displacement of 10 mm in the axial direction. The indentor was a wood model of the human fingertip of 15 mm in diameter and 100 mm in length, representing a first approximation of human fingertip. To achieve greater accuracy, differences between the wood indentor (which is a non-compliant object) and human fingertip (which is a compliant object) should be taken into account. However, since deformations induced onto a fingertip which interacts with the fabric are relatively small, the usage of a non compliant indentor is reasonable. The indentor was equipped with both a magnetic linear transducer, Vit KD 2300/6C by KAMAN Science Corporation (Bloomfield, Connecticut, USA), in order to measure the vertical dis-

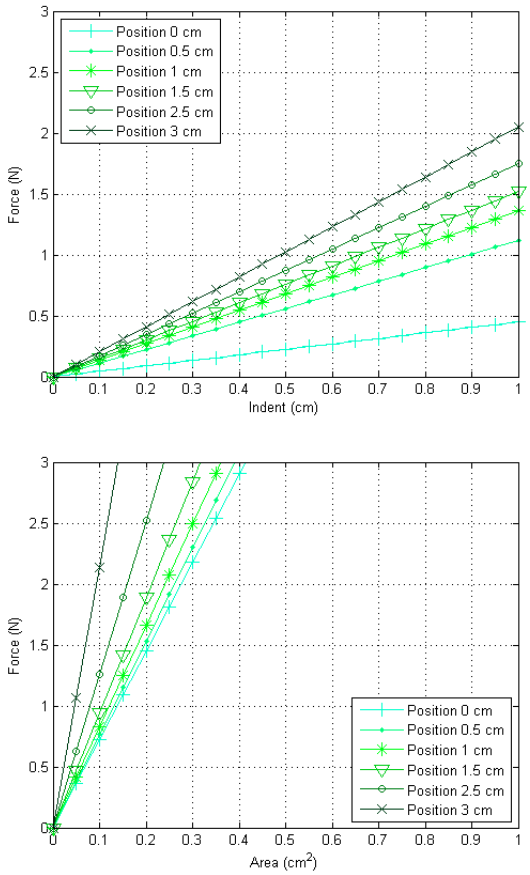

Figure 2.11: Characterization: $P(\delta)$ (upper figure) and $P(A)$ (lower figure) curves, obtained using a 5 mm step for the vertical crown displacement.

placement of the fabric surface, and a load cell sensor, ELH-TC15/100 by Entran (Hampton, Virginia, USA), which is able to detect forces up to ± 50 N. In this manner, I obtained a real-time measurement of $P(\delta)$ characteristics for each position of the crown.

At the same time, it was possible to acquire the image of the strained fabric, by means of the camera endowed with high luminosity

LEDs, placed just beneath the fabric surface (at a distance of 30 mm). Upon previously described processing algorithms, an estimation of the contact area under the indenting force was given. In this manner, a real-time measurement of $P(A)$ characteristics was obtained.

What is noticeable is that $P(A)$ and $P(\delta)$ curves are linear over all the positions of the crown.

During the characterization phase, only a finite set of positions was acquired. For intermediate values, an interpolation is necessary; since, as it results from figure 2.11, even if $P(A)$ and $P(\delta)$ curves are linear at fixed positions of the crown, fabric elasticity does not change in a linear manner across all these positions, a piecewise linear interpolant is adopted. It is possible to mimic a given material with a specific stiffness coefficient (which can be regarded as the angular coefficient of the $P(\delta)$ linear curve), by suitably identifying the corresponding position of the crown. Moreover, from the actual measure of the contact area, since $P(\delta)$ and $P(A)$ curves are coupled, an indirect estimation of the indented force and hence of the displacement can be obtained.

Notice that these estimations are strongly related to the nature of the contact. Indeed, in order to obtain coherent values, subjects should touch the fabric in the same manner as the wood indentor did during the characterization phase. However, this fact is not much reliable, since many factors can vary, e.g. the inclination of the fingertip w.r.t. fabric surface. Therefore the indirect estimations of P and δ have to be considered only as rough approximations, which can be useful to provide a general idea of the interaction, without any claim of exhaustiveness.

To overcome this problem, a second camera should be used, to accurately measure fabric indentation, e.g. by processing the length of a small line drawn on the lower surface of the fabric.

2.4.5 Graphical User Interface and Virtual Reality Implementation

A GUI (Graphical User Interface) is implemented in Matlab by MathWorks (Natick, Massachusetts, USA) to enable for a correct utilization of the display. The GUI presents a hierarchical structure and consists of four windows: two for the initialization of the prototype and two for the contact area measurement, and force and indentation indirect estimation (see figure 2.12).

The "Home" window has the main role of managing all the simulation levels. In fact, from the "Home", each level of the GUI can be reached using an easy drop-down menu. The "Initialization" window permits to insert a stiffness coefficient for the simulation of a particular material. This stiffness coefficient corresponds to an angular coefficient of an unknown $P(\delta)$ characteristic, which can be obtained interpolating the characterization curves. At the same time, the angular coefficient describing the related $P(A)$ characteristic is calculated. The "Measurement" window offers a complete environment for the real time visualization of the principal contact parameters (measured contact area, estimated force and indentation), with the possibility of visualizing both the results from the area detection algorithm and the RGB acquisition of the indented fabric surface. The "Measurement" window also enables for a control of the correct functionality of the display, in terms of motor performance monitoring. In the "Virtual Reality" window a simple virtual reality application is realized to geometrically describe both the contact area and the exerted indentation indirectly estimated from

The Virtual Reality is also implemented in Matlab, see figure 2.15. To describe the geometry of the indentation, two hypotheses are assumed:

a. Contact area shape: the contact area shape is a perfect circle with radius of $\sqrt{C_{\text{area}}/\pi}$ (C_{area} is calculated using the area detection algorithm);

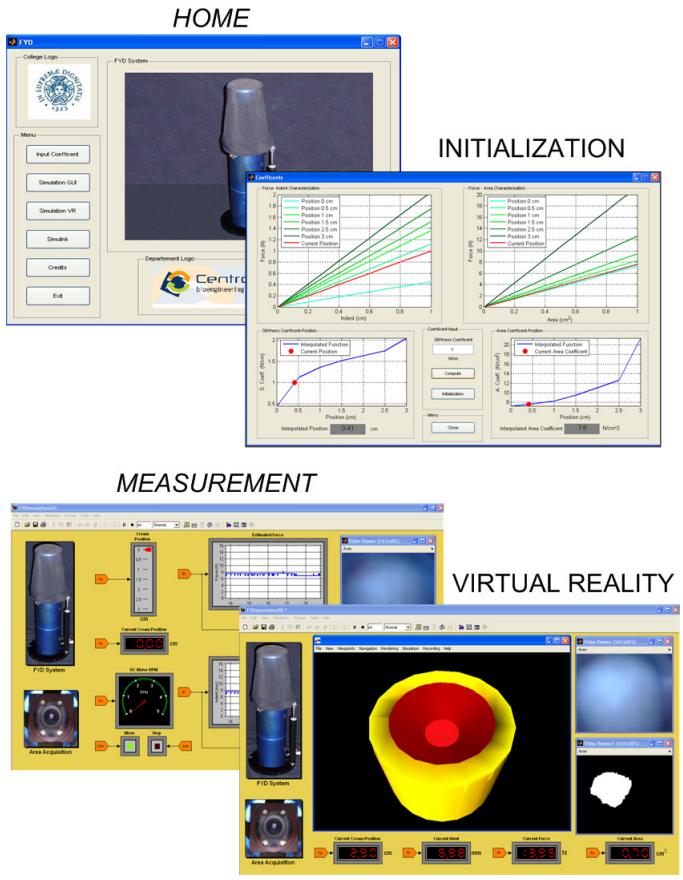

Figure 2.12: GUI: HOME and INITIALIZATION windows for the initialization of the prototype; MEASUREMENT and VIRTUAL REALTY windows to display the values of force, area and indentation.

b. Indentation: the axis of the indentation is the vertical axis of FYD.

Starting from assumptions (a) and (b), the indented surface is approximated using a set of truncated right cones nested together. They present the same larger base area (which is equal to the upper base of FYD), while the surface of the smaller base corresponds to the contact

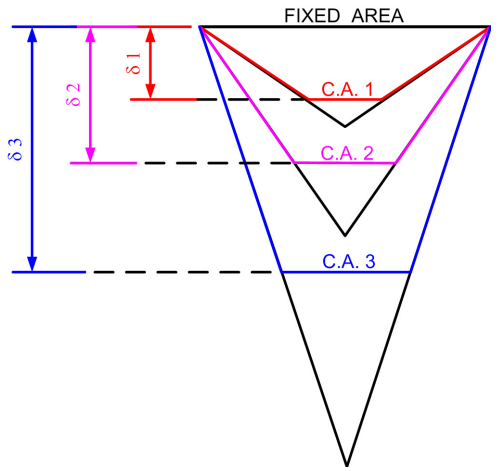

Figure 2.13: The set of truncated cones associated to different levels of indentation. The term "C.A." refers to the contact area. The term δ refers to the indentation.

area and it changes according to the value of indentation. Each value of indentation is associated with a truncated cone, i.e. each value of indentation describes the height of a truncated cone, figure 2.13. In this manner, only the internal lateral surface of the truncated cone is useful for a correct visualization in a virtual environment and so visible, while the rest of the cone is not displayed, even if drawn. To completely describe the lateral surface, the only parameter to determine is the total height of the cone, h. This parameter can be obtained by exploiting very simple geometric considerations. Referring to figure 2.14, it is possible to write

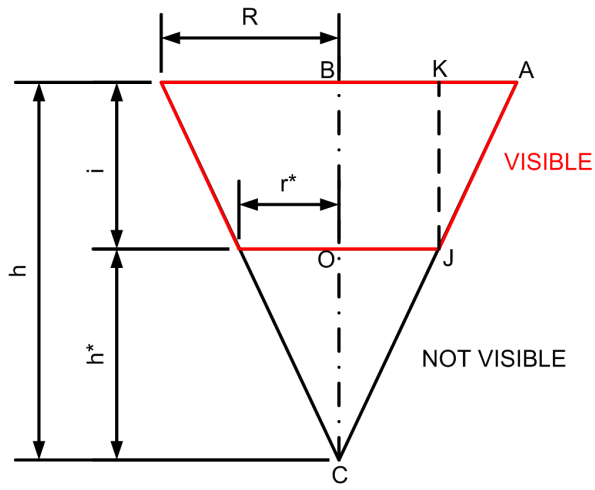

Figure 2.14: Cross section of a cone and some geometric parameters. h is the total height of the cone (to be determined), i the indentation and R and r^*, respectively, the radius of the larger base and the radius of the smaller base. h can be obtained by exploiting the similarity of the triangles $\widehat{JKA}$ and $\widehat{COJ}$.

$$\overline{AB} = R$$

$$\overline{BK} = \overline{OJ} = r^* \tag{2.12}$$

$$\overline{AK} = \overline{AB} - \overline{BK} = R - r^*,$$

with R ed r^*, respectively, the radius of the larger base and the radius of the smaller base (known from assumption (a)). Moreover

$$\overline{BO} = \overline{KJ} = i$$

$$\overline{OC} = h^* = \overline{BC} - \overline{BO} = h - i, \tag{2.13}$$

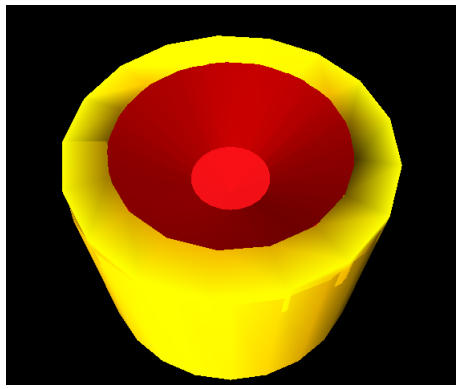

Figure 2.15: Final representation of the geometry of the indentation in the virtual reality.

with i ed h, respectively, the indentation (indirectly estimated) and the cone height (unknown). Exploiting the similarity of $\widehat{JKA}$ e $\widehat{COJ}$ triangles, it is possible to write

$$\overline{OC} = \frac{\overline{OJ} \cdot \overline{KJ}}{\overline{KA}} = \frac{r^* \cdot i}{R - r^*}. \tag{2.14}$$

Considering that cone height h is given by

$$\overline{BC} = \overline{BO} + \overline{OC}, \tag{2.15}$$

finally, h is calculated as

$$h = i + \frac{r^* \cdot i}{R - r^*} = \frac{R \cdot i}{R - r^*}. \tag{2.16}$$

2.4.6 Psychophysical Experiments

The experimental session was designed to evaluate the performance of the FYD, comparatively with a discrete CASR display [30]. The performance of the FYD is assessed both with the integration of the virtual reality rendering and without it, in order to evaluate if the system improves when visual stimuli are provided. Five simulated level

of stiffness ($SS1$, $SS2$, $SS3$, $SS4$ and $SS5$) were chosen to be rendered both with FYD and the discrete CASR display. The latter one was experimentally characterized by means of indentation tests at different constant pressures. A compressional indentor was driven by an electromagnetic actuator (Bruel & Kjear mini-shaker). The indentor was a metallic cylinder of 1.5 cm in diameter and 10 cm in length and was equipped with a magnetic linear transducer, Vit KD 2300/6C by KAMAN Science Corporation and a load cell sensor, ELH-TC15/100 by Entran.

In table 2.1 the input parameters for FYD and of the discrete CASR device necessary to reproduce the five simulated stiffness values are reported.

Stiffness	**Coeff.** (N/cm)	**Pressure (bar)**	**Position (cm)**
SS1	0.67	0.35	0.16
SS2	1.00	0.5	0.41
SS3	1.18	0.6	0.86
SS4	1.28	0.7	1.44
SS5	1.71	0.8	2.33

Table 2.1: Discrete CASR display (third column) and FYD (fourth column) parameters. The term "Position" refers to the vertical position of the crown of the FYD (position 0 is chosen near the top of the cylinder) associated to a given stiffness coefficient. The term "Pressure" refers to the pressure of the air inflated into the internal camera of the discrete CASR display to mimic a given stiffness coefficient. At each value of "Position" of FYD corresponds a value of "Pressure" of discrete CASR device, in order to render the same level of stiffness.

2.4.6.1 Subjects

After written consensus, 10 healthy volunteers participated in the study. Their age ranged from 23 to 40. None had a history of nerve injury or finger trauma and their finger pads were free of calluses. 5 volunteers participated only in the experiments with the discrete CASR display; 5 volunteers participated only in the experiments with the FYD display (with and without the virtual reality integration); 5 volunteers participated in all the experiments. In conclusion, each type of experiment was performed by 10 subjects. Their handedness was evaluated by the Edinburgh Handedness Inventory (EHI) [66] and they were allowed to use the dominant hand to perform the task. They always performed the tests comfortably sat, blindfolded (except for the tests performed with the integration of the virtual reality rendering, in which subjects were requested to look at a monitor visualizing the rendered tactile experience in the virtual environment) and with plugged up ears, to prevent the possible use of any other sensory cues and eliminate any diversion from the task. The chosen arm was locked to the table and the subject was able to move the wrist and fingers only.

2.4.6.2 Experiments: Design and Procedure

Subjects participating in these experiments were presented with rendered levels of stiffness and were asked to judge them by touch. They were instructed to do so by pressing vertically or tapping the index finger of their dominant hand against the displays. Subjects were recommended to not perform movements of the finger across the surface and to not apply lateral forces. In this manner, according to the literature [54], any anisotropic effect or distortion in softness perception due to the radial/tangential discrepancy in touch is eliminated, only focusing on normal indentation of the specimens. Experiments were designed to test the ability of subjects to tactually discriminate softness both through the discrete CASR display and through the FYD, with and without the integration of the virtual reality feedback. The

experiments included pairwise discrimination and ranking tasks. In all tests, subjects had no time limitations and were allowed to check each haptic stimulus as many times as they wished going back and forth between them at will. The design of the experiments, in evaluating ranking and pairwise discrimination performance, is similar to the approach reported by [37].

2.4.6.3 Pairwise discrimination

In each trial, a standard ($SS3$) and a comparison rendered level were presented to the subjects in random order. After probing the specimens, subjects were asked to report which of the two was softer. Each task was performed three times for each subject. Subjects were presented with new stimuli in less than a second.

2.4.6.4 Ranking

In the ranking experiment subjects were asked to probe and sort in terms of softness the set of 5 level $SS1$ to $SS5$, presented in random order. Ranking tasks were repeated three times for each subject. Subjects were presented with new stimuli in less than a second.

2.4.7 Experimental Results and Discussion

2.4.7.1 Pairwise discrimination

Results of pairwise discrimination experiments, for both the displays, are reported in figure 2.16. Answers are classified as $X = 1$ if the subject correctly identifies the softer specimen, or $X = 0$ otherwise. The average number of correct answers m_n is represented by the height of the histogram bars in figure 2.16. The number of correct answers is normalized, i.e. it is expressed in percentage terms as the ratio between the number of correct pairwise discriminations and the total number of the pairwise discriminations. Therefore, the maximum

possible value assumed by m_n is 1, equivalent to a percentage of correct recognition of 100%. The statistics of this binary experiment are described by its Bernoulli distribution. Confidence intervals for expected values $E(X)$ with statistical significance $(1 - \alpha)$ are also reported in figure 2.16. The intervals are computed as:

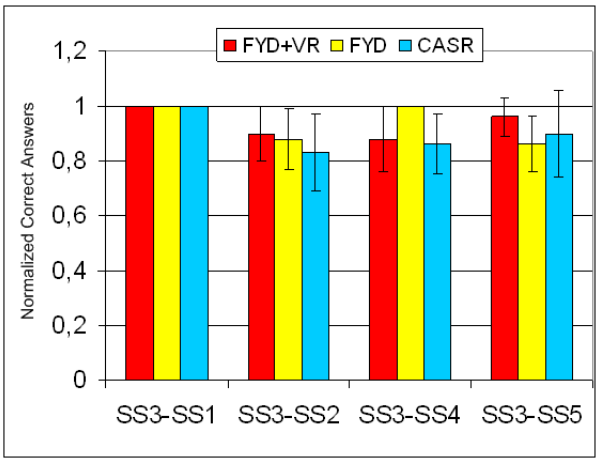

Figure 2.16: Results of pairwise test with CASR and FYD, with and without the virtual reality feedback.

$$E(X) \in \left[m_n - z_{\alpha/2}\sqrt{\frac{m_n(1-m_n)}{N}}, m_n + z_{\alpha/2}\sqrt{\frac{m_n(1-m_n)}{N}} \right], \tag{2.17}$$

with $\alpha = 5\%$, sample size $N = 30$, and critical value of the normalized standard distribution $z_{\alpha/2} = 1.96$ (from standard statistical tables). A chi-squared binary was performed to test the hypothesis of sample independence between the three conditions (i.e. discrete CASR, FYD with virtual reality environment, FYD without virtual reality environment), using chi2bintest function for Matlab (Peder Axensten, © 2007). In this case, p-value expresses the error risk to claim that the samples are independent. A significant level of $\alpha = 0.05$ is

assumed. It is worthwhile noting that for both the displays the normalized correct answers are very similar and comparable ($p > 0.05$).

2.4.7.2 Ranking

	SS1	**SS2**	**SS3**	**SS4**	**SS5**	$N°$	**Relative A.**
SS1	18	4	1	1	6	30	60%
SS2	0	19	8	3	0	30	63%
SS3	2	1	18	8	1	30	60%
SS4	8	1	1	17	3	30	56%
SS5	2	5	2	1	20	30	66%
							Total A.
$N°$	30	30	30	30	30	150	61%

Table 2.2: Confusion matrix of ranking experiments with the discrete CASR display. The term "Relative A." refers to the accuracy, i.e. the percentage of correct recognition, associated to a specific level. The term "Total A" refers to the total percentage of correct recognition, considering all the levels.

Results from ranking experiments are shown in tables 2.2, 2.3 and 2.4, where subjective softness is reported versus objective compliance in a confusion matrix structure [37] for the five levels, under the three different conditions. Values on the diagonal express the number of correct answers. The percentage of total accuracy is calculated considering the sum of all correct answers. The correspondence between an objective estimation of the compliance and the subjective evaluation in terms of numerical values in a given scale was already used in other work [37, 67]. The results obtained with the discrete CASR display exhibits a percentage of total accuracy of 61%. The results

	SS1	**SS2**	**SS3**	**SS4**	**SS5**	$N°$	**Relative A.**
SS1	22	4	0	2	2	30	73%
SS2	4	25	1	0	0	30	83%
SS3	0	1	27	0	2	30	90%
SS4	3	0	0	25	2	30	83%
SS5	1	0	2	3	24	30	80%
							Total A.
$N°$	30	30	30	30	30	150	82%

Table 2.3: Confusion matrix of ranking experiments with FYD display, without the virtual reality feedback. The term "Relative A." refers to the accuracy, i.e. the percentage of correct recognition, associated to a specific level. The term "Total A." refers to the total percentage of correct recognition, considering all the levels.

obtained with FYD, without virtual feedback, exhibits a percentage of total accuracy of 82%. When subjects were allowed to exploit the virtual reality rendering, a total accuracy of 84% is observed. In addition, the dispersion of the matrix for FYD display is reduced and the matrix appears to be diagonal. The latter result is more evident when visual cues are provided.

2.4.8 Conclusions

Results show that FYD seems to enable for a better softness perception than the discrete CASR display. In pairwise discrimination results between these two devices are comparable, but in ranking experiments FYD exhibits the best performance. This enhancement is probably due to the absence of edge effects during the interaction between fingertip and fabric surface. This new device appears to pro-

	SS1	**SS2**	**SS3**	**SS4**	**SS5**	$N°$	**Relative A.**
SS1	24	6	0	0	0	30	80%
SS2	6	24	0	0	0	30	80%
SS3	0	0	30	0	0	30	100%
SS4	0	0	0	24	6	30	80%
SS5	0	0	0	6	24	30	80%
							Total A.
$N°$	30	30	30	30	30	150	84%

Table 2.4: Confusion matrix of ranking experiments with FYD and the virtual reality feedback. The term "Relative A." refers to the accuracy, i.e. the percentage of correct recognition, associated to a specific level. The term "Total A." refers to the total percentage of correct recognition, considering all the levels.

vide cues for a more reliable and realistic perception, since the fabric is deformable in a controlled way under the fingertip. This fact can help to develop in a more effective manner haptic memory required for multiple comparisons.

Furthermore, the real-time contact area measurement might allow to mimic real CASR curves in a more efficient way.

Notice that FYD structure, in which everything is controlled by measuring the position of the external crown, is simpler than the one required for discrete CASR display, where the telescopic arrangement of the cylinders as well as the embedded sensor placement can be quite difficult to realize.

When FYD is used with the integration of the virtual reality feedback, the best results are observed, especially in ranking experiments when haptic memory is integrated with visual memory. Indeed, since visual information is related to the contact area and local deformation

Figure 2.17: The last version of FYD (dimensions: 110 x 90 x 222 mm) and a subject's fingertip interacting with the display.

of the fabric it can provide helpful cues in discriminating softness, with many possible applications, e.g. medical training and video-games.

The above discussed results are very encouraging and further support the CASR paradigm in softness discrimination.

A new version of FYD with reduced dimensions has also been realized, as it is shown in figure 2.17. In this version, a linear actuator L12 with integrated controller (Firgelli Technologies Inc., Victoria, BC, USA) has been used instead of the screw-female screw system, improving dynamic characteristics and control. Device miniaturization will be useful to enlarge the range of applications characterized by a limited workspace, e.g. RMIS.

Chapter 3

New Strategies to Convey Cutaneous Information: a RMIS Application

In previous chapters, methods to harness cutaneous information manifold have been discussed. More specifically, referring to discrimination of softness, a fabric-based device has been proposed, which is able to produce a more compelling perceptual experience.

In this chapter, the geometrical approach that has been followed so far is used to individuate simple design primitives and strategies to vehiculate information about stiffness and geometry of hard lumps (cancer) embedded in soft tissues. This information has to be conveyed to surgeons during palpation tasks performed in Robot-assisted Minimally Invasive Surgery (RMIS) to enhance diagnostic performance.

RMIS represents a very challenging application field, since the need to restore tactile feedback during typical surgical exploration is a well-documented problem [32, 68, 69]. Common tasks like localization of hard lumps embedded in soft tissues are extremely affected by the complete lack of tactile feedback, since robot-assisted surgery prevents direct contact between surgeon's hand and tissues.

With numerous tactile display mechanisms and even more proposed applications, there is seemingly an infinite number of possible tactile devices to be used.

Pin-based tactile arrays [31–33] represent commonly explored technology for this problem; these systems are built in various forms and are able to produce a wide range of perceptual stimuli upon the finger pad. However, their somewhat bulky size [34] as well as the design complexity are not well suited for typical RMIS applications, in which the main requirements are simplicity in design, reduced dimensions and footprint, in order to avoid any limitations to master manipulator workspace. For this reason, a more targeted approach is necessary.

The idea is to search for reductions from the high-dimensional complexity of the technological devices so far exploited to a low-dimensional space, where the perception of the lump is related in a more direct and natural manner to the technological solution adopted to render it.

Therefore I propose a pneumatic air-jet approach in which a pressurized air is directed to the finger pad through a small circular aperture, creating a somewhat hemispherical "lump-like" indentation upon the finger pad, see figure 3.1.

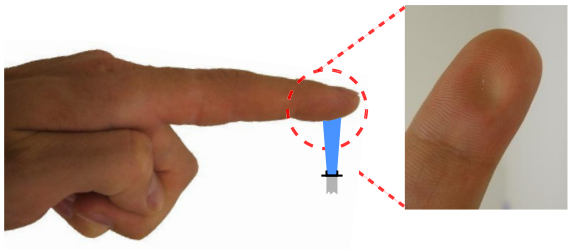

Figure 3.1: Proposed lump display method.

This idea was previously explored in [35], but not rigorously tested quantitatively or evaluated psychophysically. In [35] authors directed an air-jet into a thin membrane and varied lump size by changing the distance between the jet and the finger. This technique provides a

sensation of feeling a lump within tissue, which is clinically realistic, but may restrict the range of stiffness that can be achieved. Moreover, RMIS workspace limitation can prevent an easily implementation this approach which relies on changing the distance w.r.t. user's finger to convey different lump perceptual cues.

In this work, the basic concept is to adopt two independent control parameters, which are hypothesized to enable for the manipulation of the perceived stiffness and size of the lump, respectively. These parameters are (1) the supply pressure of the air and (2) the size of the aperture through which that air escapes. This format allows somewhat compact design and may eventually result to be more suitable for RMIS integration.

Notice that the term pneumatic "air-jet" here indicates a stimulus in which air flows out of a nozzle over a distance until it contacts the finger. There are other pneumatic-based devices in literature and sometimes they are referred to as "air-jet"; however, they act more like a pin-based or balloon arrays [33, 70, 71].

Air-jet techniques have been already used in tele-manipulation to provide general touch feedback cues to the operator [72]. Moreover, large arrays of air jets have also been used as stimulation devices for functional somatotopic mapping in conjunction with fMRI machines [73]. These applications use air-jets for general instructional or directional cues, while RMIS requires a more targeted approach. Furthermore, an air-jet as a haptic stimulus is largely unexplored and untested. The more it is possible to understand about it and how it is controlled and the perception it induces, the larger the number of applications in which it can be used.

With this as a motivation, in this chapter I describe the development of the pneumatic lump display apparatus. Capacitive tactile sensors were used to measure the output of the display, which is quantitatively analyzed by using classic fluid dynamics tools. Moreover, psychophysical experiments were conducted to individuate the smallest changes in supply pressure and aperture size which are detectable to the human finger.

Part of the results of this characterization was illustrated in [A3]. These results have provided the theoretical framework and guidelines for the development of a novel air-jet pneumatic lump display [A4].

As already said in the Introduction, the work described in this chapter was done in collaboration with James C. Gwilliam, a Biomedical Engineering PhD candidate from Johns Hopkins University School of Medicine, who equally contributed to it, and will be included also in his PhD dissertation.

This collaboration refers to my visiting period (January-June 2011) at the Laboratory for Computational Sensing and Robotics (LCSR) - Johns Hopkins University, under the supervision of Prof. Allison M. Okamura (Research Professor in the Department of Mechanical Engineering and Vice Chair, Johns Hopkins University till June 2011; from July 2011, Associate Professor in the Department of Mechanical Engineering, Stanford University).

3.1 Theoretical Background

To describe air-jet lump display, turbulent jet theory is exploited [74]. A jet is defined as a system in which a fluid (e.g. air) issued unidirectionally from a localized source enters a quiescent medium of the same fluid, causing turbulence in the process.

In the case here analyzed, the jet impinges against an obstacle during its motion, more precisely against a finger pad.

In figure 3.2 the three distinct regions of turbulent jet impingement flow are illustrated: (1) the zone of flow establishment begins at the jet nozzle and ends 4-6 A downstream, where A is the diameter of the jet nozzle. This region contains the "potential core", where there remain regions of jet fluid which have not mixed with the surrounding fluid. (2) The second region is referred to as the established jet region, where the asymptotic scaling for jet spread and velocity decay pertains [75]. (3) The third region, called the impingement zone, exhibits very different characteristics from the first two regions. It

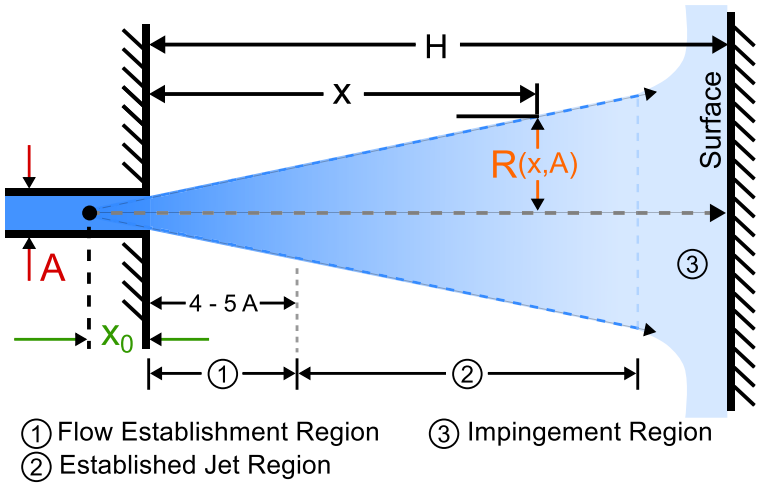

Figure 3.2: A typical round jet develops as a conical shape with a jet spreading rate, S. The jet radius (R) is a function of the distance from the outlet (x) and the aperture diameter (A). The jet exhibits properties which can be divided into three distinct regions of interest.

begins when the pressure and velocity of the flow are altered by the presence of the obstacle and includes the stagnation point, at which the local velocity of the flow is zero.

Beyond the establishment region, free-jets spread linearly with distance from the nozzle exit and the centerline velocity decays inversely with this distance. The jet velocity decay with distance can be defined by

$$\frac{U_0(x)}{U_J} = \frac{B}{(x - x_0)/A} \tag{3.1}$$

where $U_0(x)$ is the jet centerline velocity at a distance x from the jet nozzle, U_J is the jet centerline velocity at exit, x_0 is the virtual origin, A is the aperture diameter, and B is an empirical constant called the velocity decay coefficient [74]. The linear spreading rate

(S) of the jet can be defined by

$$S = \frac{dr_{1/2}(x)}{dx} \tag{3.2}$$

where $r_{1/2}(x)$ is the radial distance at which axial velocity falls to half of centerline speed.

The goal of the measurements performed in this study is to characterize the specific flow setup contained in the air-jet lump display. Classical jet theory serves only as a reference point from which to view the results of this study.

3.2 Design and Characterization

An experimental apparatus was built to measure distributed pressure patterns on a tactile sensor array while air supply pressure and outlet aperture size are controlled. The apparatus (figure 3.3) consists of three main components: (1) an electronically controlled air pressure regulator, (2) a set of interchangeable aperture diameters through which the air escapes, and (3) a tactile sensor array to measure the output.

The electronically controlled pneumatic regulator (SMC-ITV2031-21N2L4, SMC Corporation, Noblesville, IN, USA) provides step-less control of air pressure (0.05 - 0.5 MPa) proportional to an electrical signal (0 - 5 V), with a maximum flow rate of 1500 L/min. Linearity between the input signal and set pressure is within ±1% full scale (F.S.), hysteresis within ±0.5% F.S. and sensitivity within 0.2% F.S.

The aperture size was set with six acrylic plates (5.4 mm thick), each with a single drilled hole diameter ranging from 1.0 - 4.5 mm (as reported in table 3.1). These values were chosen in order to match common dimensions of small-medium lumps embedded in tissues. A plate was clamped to the underside of the apparatus with the aperture centered over the air source aperture, separated by a rounded rubber washer to prevent air leaks. The regulator-supplied air was then forced through the fixed aperture onto the tactile sensors.

Table 3.1: Parameters for tactile sensor measurements

Aperture Diameters (mm)						
A1	**A2**	**A3**	**A4**	**A5**	**A6**	**A7**
1.0	1.9	2.3	2.75	3.2	3.6	4.5

Supply Pressures (psi)						
P1	**P2**	**P3**	**P4**	**P5**	**P6**	**P7**
10	20	30	40	50	60	70

The tactile sensor array is composed of three smaller sensors (DigiTacts, Pressure Profile Systems, Los Angeles, CA, USA) arranged contiguously to form a 6×12 array of tactile sensing elements, occupying a total footprint of 12×25 mm (figure 3.3, left). Each individual sensor contains 24 sensing elements (each element measuring 1.8×1.8 mm). The sensors are capacitive and provide a linear response with a sensing range of 0 - 0.14 N/mm^2 and a sensitivity of 6.9×10^{-4} N/mm^2.

A graphical user interface was developed in the QT environment (QT Creator, Nokia, Helsinki, Finland) to send pre-calibrated voltage levels from the computer via a NI-DAQ card (DAQCard-6024E by National Instruments) to the electronic pressure regulator. The tactile sensor array was centered 14 mm below the output aperture on a flat rigid surface. Seven discrete and equally spaced supply pressure levels between 10 and 70 psi (68.9 - 482.6 kPa) were used (cf. table 3.1) to output air from the display onto the sensor array. Given the supply pressure values as well as the turbulence nature of the jet, gravity effects are assumed to be negligible. Pressure values were heuristically chosen in order to enable for the simulation of a wide range of pressure stimuli on the finger pad, thus avoiding too much high pressure that

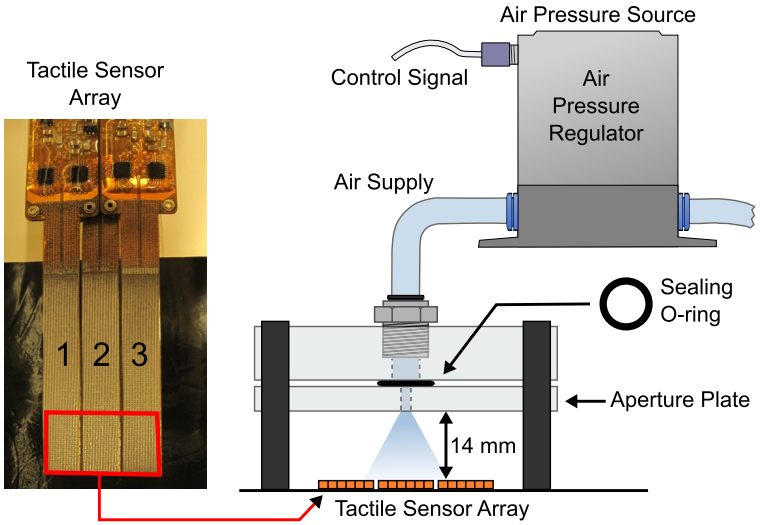

Figure 3.3: Setup for tactile sensor measurement. The air pressure regulator forces pressurized air through the aperture plate. It connects directly to the air source aperture and controls supply pressure. Tactile sensors placed under the aperture record distributed pressure as supply pressure and aperture size are varied.

can induce pain. The distance of 14 mm was heuristically chosen since it provides a safety distance for user's finger pad and do not affect master manipulator dexterity.

3.2.1 Quantitative Characterization

The pneumatic lump display can be characterized by determining the complex relationships between the supply pressure of the air, the aperture size, and the resulting output pressure upon the finger (or in this case, the tactile sensor array). This characterization occurs as the two independent variables (supply pressure, aperture size) are varied in a systematic manner, while the independent variable (output pressure) is measured on the tactile sensor array.

Ideally, the display output pressure would be determined using

models of fluid dynamics. However, an accurate model is difficult to obtain since the system is affected by many factors, including air temperature, the type of air flow (e.g., laminar, turbulent), and resistive pressure losses due to friction along the length of the tubing. Therefore, given the simplicity of the test apparatus system (and hence display mechanism), the measured tactile data is a valuable substitute for a full fluid dynamics system model. The output pressure of the pneumatic lump display is evaluated in terms of (1) the peak pressure value obtained during a measurement and (2) the distributed pressure profile produced as the air impinges on the surface of the tactile sensors.

Additionally, the sensor-based characterization is necessary for establishing the desired output pressures for subsequent human psychophysical experiments.

Tactile sensors were used to measure air-jet output using every permutation of seven apertures sizes and seven supply pressures (table 3.1). A single trial consisted of a tactile sensor recording at 35 Hz for 30 seconds, after which recording stopped. Prior to each measurement, the tactile sensor array was set to a zero baseline to remove any residual pressures and increase the signal-to-noise ratio (SNR) of the measurement. For each aperture size, measurements began with the smallest supply pressure (10 psi) and proceeded ascending order of supply pressures, followed by descending order of supply pressure measurements. Values assumed by tactile sensor elements were averaged across the duration of the recording (referred to hereafter as a "tactile image", T), and the maximum (peak) pressure value (T_{peak}) extracted from the resulting tactile image (figure 3.4, left).

Moreover, for each measurement, the column (T_c) of sensor elements which contains the peak pressure value is used to analyze the resulting pressure profile distributions. In all cases, T_{peak} (and hence T_c) is expected to be near the center of the tactile sensor array since the air-jet was centered over the sensors. The values assumed by elements from T_c were used to fit the distributed pressure profile produced as the air impinges on the surface of the tactile sensors. Al-

though, using a column of sensor elements provides less elements for curve fitting (due to sensor array footprint), it ensures that elements used span a single sensor, thus eliminating inter-sensor variabilities.

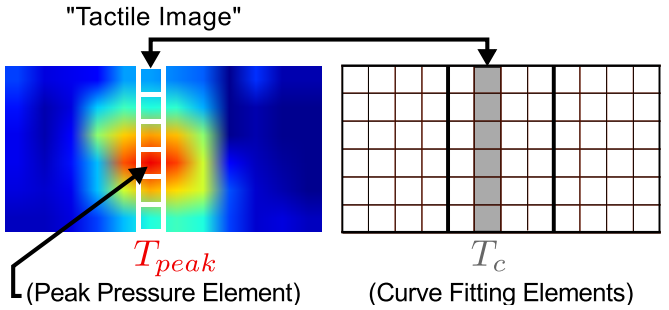

Figure 3.4: Example of peak pressure value and corresponding column of tactile sensor elements. (Left) Sensor element data are averaged, resulting in a "tactile image" with a peak pressure value at element T_{peak}. (Right) T_{peak} determines which column of sensor elements (T_c) is used to fit the distributed pressure profile.

3.2.2 Tactile Sensor Results

Figure 3.5 shows tactile sensor peak pressure values for every combination of aperture size and supply pressure. Each marker represents a tactile sensor peak pressure value from a particular aperture size and supply pressure. Aperture sizes increase from left to right on the horizontal axis, while supply pressures are indicated by unique line colors and marker types. Several observations can be made from these data. First, increasing the supply pressure for a single aperture size results in somewhat consistent incremental increases in the resulting tactile sensor peak pressure. Second, the peak pressure values are minimum at the smallest and largest aperture diameters, and maximum in between. This effect is especially exaggerated for larger supply pressures and much more subtle for smaller supply pressures. At small aperture sizes, resistive forces dominate, resulting in high

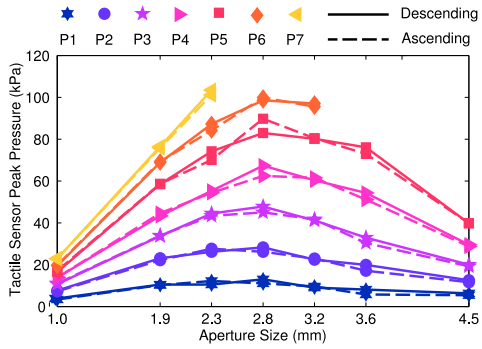

Figure 3.5: Peak pressure values obtained from tactile sensor measurements. Aperture sizes increase from left to right. Each line and marker type represent a unique supply pressure. Solid and dashed lines represent measurements obtained during descending and ascending series of supply pressures, respectively.

flow impedance and subsequently smaller pressure outputs, as seen in the left half of figure 3.5. However, as aperture size increases, the impingement zone becomes closer to the nozzle exit, where the velocity profile is flatter [75], thus resulting in a decreasing of the peak pressure amplitudes, as observed in the right half of figure 3.5. Third, there is little hysteresis in the sensor measurements, as evidenced by nearly identical traces of ascending and descending series recordings. Finally, the highest supply pressures (P6, P7) were not attainable using the larger aperture sizes with the experimental equipment, as shown by the incomplete traces shown at the higher supply pressure levels.

Figure 3.6 shows the pressure profiles obtained from the set (T_c) of tactile sensor elements containing the peak pressure value, with each point representing an individual tactile sensor pressure value. Since the static pressure profile of an air-jet at an impinging surface is normally considered to be Gaussian [76], a two-dimensional Gaussian curve was fit to these averaged pressure profile values (figure 3.4) using the ezyfit curve fitting toolbox for Matlab (Frèdèric Moisy, © 2010).

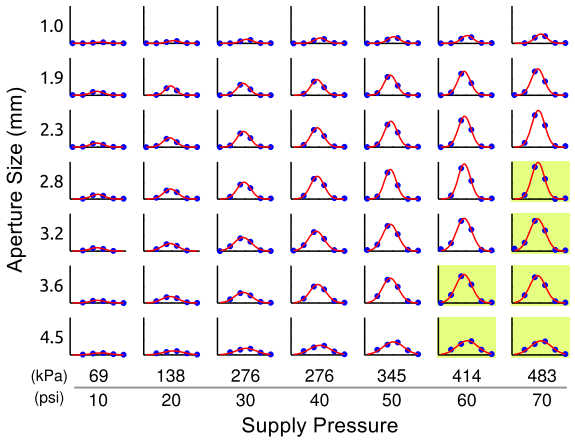

Figure 3.6: Gaussian curve fits for each tactile measurement. The curve is fit to the profile of the row of tactile sensor elements containing the peak pressure value.

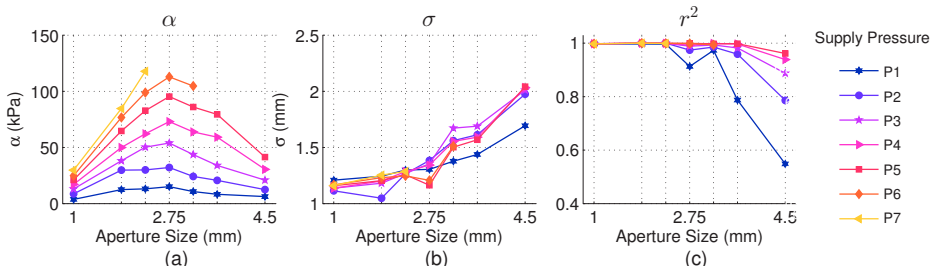

Figure 3.7: Gaussian fit parameters and r^2 values for all aperture sizes and supply pressures. (a) Gaussian fit amplitudes (α) show similar responses to peak pressure values. (b) Gaussian fit variance (σ) shows consistent increases in spatial spread as aperture size increases. For a single aperture, σ is largely independent of supply pressure. (c) Coefficient of determination (r^2) values show how each Gaussian curve fits to corresponding tactile sensor pressure profile.

The Gaussian equation is given by

$$y = \alpha e^{\frac{(x-\mu)^2}{2\sigma^2}}, \tag{3.3}$$

where α is the amplitude of the curve, μ represents the centering of the curve with respect to the tactile sensor array, and σ defines the spatial spread, or standard deviation of the curve. Each individual plot in figure 3.6 represents the pressure profile and curve fit for a specific aperture size and supply pressure. Plots with shaded backgrounds indicate measurements for which the specified supply pressure is not completely attainable at the given aperture size. Figure 3.6 qualitatively illustrates the changing shape of the pressure profiles. What is noticeable is that the magnitude of the curve increases as the supply pressure increases, as expected. However, to quantitatively assess the change in pressure profiles shape as a function of the stimulus parameters, the Gaussian fit parameters were also evaluated (figure 3.7). Figure 3.7a shows the amplitude (α) of the Gaussian curve fits, which are consistent with the general shape of the peak pressure value curves in figure 3.5. Figure 3.7b shows the spatial spread (σ) of each Gaussian fit. Two important observations can be made from this data. First, σ increases monotonically as aperture size increases, with few exceptions. Second, for a single aperture size, σ is largely independent of the supply pressure. Figure 3.7c shows (r^2) values for each fit, indicating how closely the Gaussian curves fit the tactile sensor pressure profile data. Results indicate that as aperture size increases, r^2 values decrease rapidly, especially for smaller supply pressures. This may be partially explained by two factors. First, jet theory shows that when the downstream impingement distance (H) is less than 4-5 times as large as the aperture size (A), the impingement occurs in the potential core of the flow establishment region (figure 3.2), where the flow profile has not yet become Gaussian [75]. Second, at lower supply pressures, the sensor signal to noise ratio (SNR) is at a minimum, allowing the sensor noise to become more dominant in the prescribed fit of the curve. The term μ in (3.3) describes the offset distance between the center of the Gaussian fit with respect to the center of the tactile sensor array. This term might physically represent the position error during placement of the aperture over sensor array. In all cases, this error is within $\pm\,0.5$ mm. The extreme aperture sizes show Gaussian

fits centered slightly right of center, while all others were slightly left of center. No meaningful trend is established from this parameter.

Results from figure 3.7 have important implications for the control of an air jet lump display mechanism. Figure 3.7a indicates that the amplitude, or desired peak output pressure (α) of the display is effected by both the aperture size and the supply pressure. The curves on this plot represent the "display-space" of the mechanism given the current range of parameters, and describe the space of achievable peak output pressures. Changes in peak output pressure are most sensitive to changes in aperture size at larger supply pressures. In contrast, figure 3.7b shows that the width of the pressure profile (σ) is largely independent of supply pressure, and is primarily a linear function of the aperture size. If psychophysical perception of lump size is indeed dictated by the width of the Gaussian pressure profile, then this result suggests that perceived lump size could be controlled only by adjusting the aperture size. The width of a Gaussian curve described by (3.3) at a height of $\alpha/2$ is referred to as the full width at half-maximum (FWHM), and is denoted here by $2b$, where b is the half-width of the Gaussian curve at $\alpha/2$. Figure 3.8 shows the non-dimensionalized variation of $2b/H$. For $H/A > 5$ approximately, b is proportional to H (linear fit, $r^2 = 0.99$), indicating a linear rate of air-jet expansion with increasing distance from the source. For $H/A \leq 5$ (i.e., for impingements of the potential core occuring in the flow establishment region), $2b/A$ approaches a value of 1. Figure 3.8 also shows data from Tu et *al.* [76] acquired from a plane jet over a slightly larger range of H/A, which compares favorably with the measured data of the air-jet lump display.

Moreover, notice that ratio b/H is found to be $S = 0.091$, which is very comparable to the values obtained in [77] - (0.096) - and in [78,79] - (0.102, 0.094, respectively) - in previous jet literature. An important consideration in this comparison to previous work is that the jet spread rate, S was defined by the rate at which the radial distance of the profile achieved half of the centerline velocity ($r_{1/2}$). Since no direct velocity measurements was performed, the radial distance

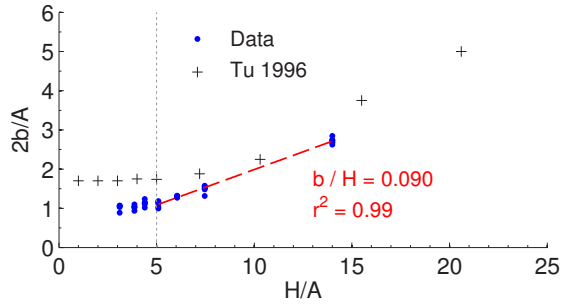

Figure 3.8: Dependence of pressure profile width on H/A. For H/A > 5, approximately, b is proportional to A ($r^2 = 0.99$). For H/A ≤ 5 (i.e, for impingement of the potential core), 2b/A is nearly constant with a value approaching 1.

(b) at which the Gaussian pressure profile achieves half-width is used instead.

3.3 Human Subject Experiments

All human subjects participating in this study were right handed volunteers and gave informed consent to perform psychophysical experiments. No subjects had any physical limitations that would affect experimental outcomes. All data collected in this study was approved by the Johns Hopkins University Homewood Institutional Review Board. Details for the three human subject experiments performed in this study are summarized in table 3.2.

3.3.1 Preliminary Open Paradigm Experiment

A preliminary perceptual experiment was conducted to evaluate how effectively the pneumatic display could produce a compelling lump percept. Subjects were provided with four different pneumatic stimuli ($A_{P1}, A_{P2}, B_{P1}, B_{P2}$), summarized in table 3.3. Letters correspond

Table 3.2: Summary of human subjects experiments

Experiment	M	F	Age
Open Paradigm	6	4	20 - 30
Pressure JND	5	5	20 - 28
Size JND	11	5	20 - 32

to the size of the aperture diameter (A= 1.6 mm, B= 2.5 mm) and subscripts indicate the output peak pressure ($P1$ = 20 kPa, $P2$ = 60 kPa). The remaining numbers show the supply pressures required to produce the desired peak pressures. These values were chosen to investigate the perceptual effects on the mid-range of the control variables. A subject's finger was fixed in a finger holder 14 mm from the aperture. Subjects were allowed to move the finger horizontally over the aperture but any vertical movement of the finger was prevented by applying skin-specific adhesive tape (Trutape LLC, USA) to the back side of the finger distal and middle phalanges to restrict movement about the distal interphalangeal joint. This constraint fixed the

Table 3.3: Stimuli for Open Paradigm Experiment

Stimuli		Aperture Size (mm) A (1.6 mm)	Aperture Size (mm) B (2.5 mm)
Peak Pressure (kPa)		**Supply Pressure (psi)**	
P1	20 (kPa)	20	14
P2	60 (kPa)	62	36

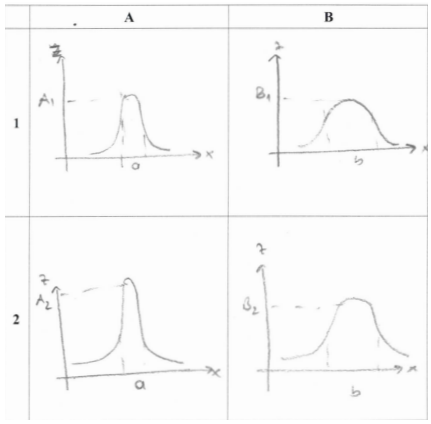

(a) Typical Response

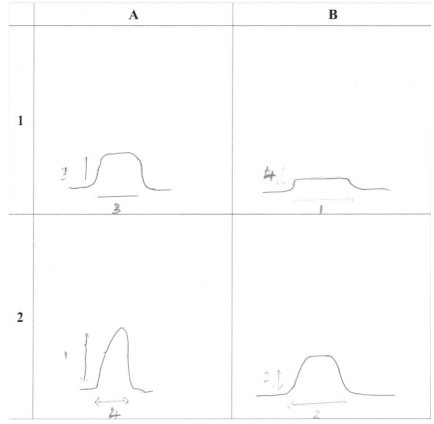

(b) Exception: Round Corners

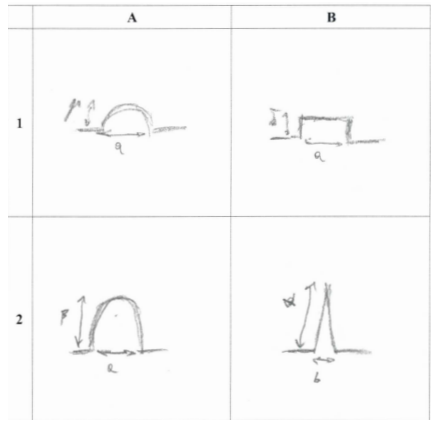

(c) Exception: Sharp Corners

Figure 3.9: Subject interpretations of open paradigm experiment stimuli. Subjects experienced four unique stimuli spanning a wide range of aperture size and output pressure, after which they were asked to draw the perceived indentation shape upon their finger pad. Three subjects' renderings are shown here for all four of the stimuli.

distance between the finer-pad and the nozzle for all the experiments. The experiment administrator alternated the stimulus between the

two aperture sizes (A or B) and the two pressure stimulus level ($P1$ or $P2$) as verbally requested by the subject. At all times, subjects could view the current stimulus parameters on a computer display. Subjects wore in-ear headphones playing white noise to avoid bias from auditory cues. Subjects were allowed to experience each stimulus as many times as desired (each stimulus lasting 1.5 seconds). After a subject deemed their exploration of the four experiment stimuli sufficient, they were asked to draw on paper the profile of the shape they perceived by interacting with each stimulus. Eight of the ten subjects drew "lump-like" shapes for all four stimuli, similar to those shown in figure 3.9a. Subject 1 drew a rectangular shape for stimulus B_1 but with rounded edges (figure 3.9b), while subject 10 drew a sharp triangular profile for stimulus B_{P2} and a wide rectangular profile for stimulus B_{P1} (figure 3.9c). Results suggest that the majority of subjects perceived profiles which were curved in shape, many of them resembling a Gaussian curve. Furthermore, most subjects varied their depiction of the profile amplitude and width (relative to the other stimuli), indicating that subjects perceived changes in the peak pressure and pressure profile width. Though it is not clear how well subjects can translate a pressure profile felt at the fingertip to a drawing canvas, it is reasonable to assume from the results obtained here that the sensation conveyed by these stimuli were reasonably associated with a lump profile in the majority of cases. This preliminary psychophysical experiment indicates that the sensation conveyed by the pneumatic display for different peak pressure levels and aperture sizes can be reasonably associated with a lump profile.

Next described experiments assess the magnitude of change in stimulus parameters required for subjects to notice differences in lump profile perception.

3.3.2 Psychophysical - Pressure JND

The aim of this experiment was to determine the minimum change in air supply pressure required to detect a just noticeable difference

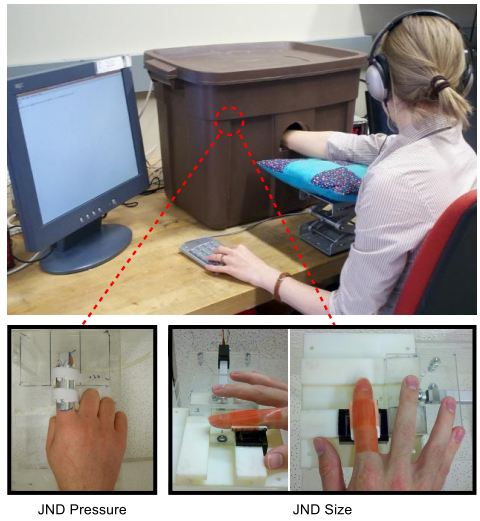

Figure 3.10: Setup for both psychophysical experiments. A subject's right index finger is fixed in place 14 mm above the aperture. Subjects enter responses about paired stimuli using a numerical keypad with the left hand. The display apparatus is placed within a sound-reducing box and subjects wear in-ear headphones playing white noise and over-ear protection to prevent auditory cues.

(JND) at each aperture size. Subjects were seated comfortably with the right index finger fixed in a finger holder, palm down, with the center of the distal finger pad centered over the aperture (figure 3.10, left). A skin-safe adhesive tape (Trutape LLC, USA), was applied to the back of the index finger distal and middle phalanges to restrict any movement of the distal interphalangeal joint. An additional finger brace was fastened around the back side of the finger to prevent motion of the proximal interphalangeal joint. Securing the finger in this manner prevents the introduction of unwanted experimental biases. The distance from the exposed finger pad to the aperture was fixed at 14 mm, consistent with the distance used in the tactile sensor experiment. Subjects received air-jet pressure to the finger pad in the form of separate but paired supply pressure stimuli, and they were asked to

indicate which stimulus in the pair produced the larger output pressure percept. Each pair consisted of a reference stimulus (RS) of 45 psi (310.3 kPa) and a comparison stimulus (CS), presented in random order. Seven equally spaced comparison stimuli were used ranging from 30 to 60 psi (206.8 - 413.7 kPa). The minimum and maximum supply pressure levels used were chosen in a preliminary study such that they were almost always judged as less than or greater than the RS, respectively [80], and in order to not be painful for subjects. The experiment consisted of five sub-parts, one for each of the five aperture sizes tested (1.3, 1.6, 1.9, 2.2, 2.5 mm). These values were chosen since the highest supply pressures were not attainable using the larger aperture sizes. The order of aperture sizes tested was randomized for each subject. An aperture plate was fixed to the apparatus in the same manner as described in the tactile experiment (Section 3.2). A single trial consisted of: the first stimulus (150 ms), an inter-stimuli interval (50 ms), and the second stimulus (150 ms), followed by the subject's response. An external monitor displayed "1" or "2" during the presentation of the first or second stimulus, respectively, followed by "Respond Now" at the conclusion of paired stimuli. Subjects then indicated the perceived greater pressure stimulus ("1" or "2") using an external numerical keypad, which was stored and written to a file. Subjects were permitted to experience a particular paired stimuli as many times as necessary by inputting an invalid response, which would repeat the previous paired stimuli. The procedure was automated, such that a subject's response automatically initiated the next trial using the randomly pre-generated stimulus set. Each sub-part consisted of 168 paired stimuli presented randomly (7 stimulus levels $\times$ 24 pairwise discriminations), and lasted approximately 15 minutes, with at least a two-minute break afterward. For all trials, subjects wore in-ear headphones playing white noise and over-ear hearing protection to prevent auditory cues (figure 3.10, top). Prior to the experiment, subjects were trained briefly using manually selected pressure pairs. These responses were not recorded.

Table 3.4: Summary of JND Pressures (kPa)

Subject	Aperture Diameter				
	1.3 mm	**1.6 mm**	**1.9 mm**	**2.2 mm**	**2.5 mm**
1	24.1	22.3	21.3	25.1	19.7
2	15.8	23.1	16.3	15.2	14.7
3	∗25.8	20.0	15.6	18.2	21.7
4	27.7	26.3	27.7	24.1	19.7
5	30.2	37.1	27.9	29.0	33.4
6	27.4	17.0	15.6	14.4	18.6
7	31.8	30.7	40.6	35.2	18.2
8	25.7	31.2	21.5	23.8	20.6
9	17.1	14.7	13.8	3.3	18.2
10	19.7	12.9	∗20.2	18.6	11.9
Mean	**24.4**	**23.5**	**22.3**	**20.7**	**19.6**
Std. Dev.	**5.7**	**7.8**	**8.6**	**8.9**	**5.6**

* Indicates JND obtained from a psychometric curve which did not demonstrate goodness of fit to the response proportion (P) data. Values with $*$ are excluded from mean values.

3.3.2.1 Results

A subject's response proportion (P) was computed for each stimulus level and expressed as $P = \sum y_i/n$, where $y_i = 1$ if the comparison stimulus (CS) was perceived as greater than the reference stimulus (RS), and $y_i = 0$ otherwise, and n is the number of pairwise discriminations performed for each CS. In trials where the RS was compared against itself, the first stimulus was randomly predefined as the RS in half of the trials, and the second stimulus in the other half of trials.

A psychometric function was fit to each data set using the pypsignifit toolbox version 3.0 (http://psignifit.sourceforge.net/), with the default logistic function, which implements the maximum-likelihood

method described by Wichmann and Hill [81] [82]. The pypsignifit toolbox is also used to evaluate the goodness of fit for each curve in terms of deviance and deviance residuals.

Results for pressure JND are reported in table 3.4. Each numerical result is the pressure JND obtained from the psychometric function fit to that data set using the psypsignifit toolbox. Those subjects for which goodness of fit is not obtained are denoted by (*) and are not used in the resulting mean or standard deviation values reported in the table. JND values for pressure range from 19.6-24.4 kPa. A one-way analysis of variance (ANOVA) reveals that no statistical difference exists between the JNDs for different aperture sizes ($p=0.62$), indicating that the pressure JND does not change significantly with aperture size. Although no statistically significant difference is observed, it should be noted that the mean JND values monotonically decrease as the aperture size increases.

3.3.3 Psychophysical - Aperture Size JND

The aim of this experiment was to determine the minimum change in aperture size required to detect a JND. In the pressure JND experiment (Section 3.3.2), changing supply pressure had no effect upon aperture size. However, in this study, changing the aperture size *does* effect the output pressure, as illustrated in the aforementioned tactile data measurements (figure 3.5). Since the focus of this experiment was to perceive changes in the size of the stimulus, it was crucial to decouple the aspects of perceived pressure and size, such that subjects were only making judgments about the stimuli size (and not the changes in perceived pressure). This required using separately calculated supply pressure levels for each aperture size tested. The tactile measurements allow this relationship to be determined empirically since it relates the supply pressures, aperture sizes, and the resulting peak output pressures in the same data set (figure 3.5). Supply pressure levels for each aperture size were calculated by selecting a constant peak pressure and interpolating to find the necessary sup-

Table 3.5: JND size psychophysical experiment

	Aperture Diameter (mm)				
	1.9	**2.3**	**2.75**	**3.2**	**3.6**
Peak Pressure (kPa)	Supply Pressures (psi)				
10 kPa	10	9	8	11	13
30 kPa	27	22	21	24	29
50 kPa	44	36	32	35	39

ply pressures to achieve that particular peak pressure. For example, supply pressure levels required to achieve a peak output pressure of 30 kPa can be obtained by drawing a horizontal line on figure 3.5 at 30 kPa and then linearly interpolating between supply pressures where the horizontal peak pressure (e.g. 30 kPa) intersects with each aperture size.

Subjects were asked to perform the experiment in three subparts, one for each selected peak pressure (10, 30, 50 kPa). Supply pressures used for each subpart are summarized in table 3.5.

The experimental apparatus (figure 3.10, right) consisted of a linear actuator (Firgelli L16, Victoria, BC Canada) endowed with analog position feedback signal, connected to a 4 mm thick acrylic plate with five different aperture sizes (table 3.5). The acrylic plate slides in a track along the direction of motor actuation over the air supply aperture. A rubber washer seated in the base sliding track created an airtight seal between the base and the acrylic plate when the system was pressurized, forcing all supplied air through the acrylic plate aperture. A voltage signal controlled the stroke distance of the linear actuator which moved the acrylic plate between aperture sizes (20 mm/s max speed). Predetermined voltage values corresponding to linear actuator stroke positions allowed the acrylic plate apertures to

be placed over the source aperture accurately and repeatably.

Subjects were seated comfortably with the right index finger fixed in a finger holder, palm down, with the center of the distal finger pad centered 14 mm over the aperture. A skin-safe adhesive tape (Trutape LLC, USA) was applied to the back of the index finger distal and middle phalanges to restrict any movement of the distal interphalangeal joint, as before. In this experiment, subjects were allowed to move their finger horizontally approximately 3 mm in each horizontal direction, thus allowing the finger to explore the stimulus size while maintaining a fixed stimulus-finger distance.

Subjects received pairs of air-jet stimuli to the finger pad in the form of separate, but distinct stimuli, separated by an inter-stimulus duration. Each stimulus pair consisted of a reference stimulus (RS) of 2.75 mm and a comparison stimulus (CS), presented in random order. Five equally spaced comparison stimuli were used, centered at 2.75 mm, and separated by approximately 0.44 mm (table 3.5). The minimum and maximum aperture sizes were selected from preliminary results of a pilot study suggesting that they could be almost always judged as less than, and greater than the RS, respectively. Moreover, they were chosen to span as much as possible the range of apertures used in the experiments with sensors. Notice that in this kind of psychophysical experiments the number of stimuli can be 7 or 5 [80].

The order of levels was randomized for each subject. A single trial consisted of: the first stimulus (1.5 seconds), an inter-stimuli interval (2 seconds), and the second stimulus (1.5 seconds), followed by the subject's response. Moreover, a delay of 30000 micro-seconds between the command that imposes a zero pressure (at the end of each stimulus presentation) to the regulator and the successive command that determines slide displacement was added, for safety reason.

An external monitor displayed "1" or "2" during the presentation of the first and second stimulus, respectively, followed by "Respond Now" at the conclusion of paired stimuli. Subjects then indicated which stimulus was perceived as containing a larger contact area upon the finger-pad ("1" or "2") using an external numerical keypad, which was

stored and written to a file. Subjects were permitted to experience a particular stimulus pair as many times as necessary by inputting an invalid response, which would repeat the previous stimulus pair. The procedure was automated, such that a subject's response automatically initiated the next trial using the randomly pre-generated stimulus set. Each level of the experiment consisted of 120 paired-stimuli trials presented randomly (5 stimulus levels $\times$ 24 pairwise discriminations), and lasted approximately 15 minutes. Throughout the experiment, all subjects wore 32 dB reduction ear plugs and over-ear noise canceling headphones playing white noise to prevent auditory cues. Vibrations from motor movement were difficult to perceive, but were present and similar enough in duration to be safely ignored (figure 3.10, right). Prior to the experiment, subjects were briefly trained with the span of individual stimuli to be used in the experiment.

3.3.3.1 Results

Results for aperture size JND are reported in Table 3.6. Each JND value is obtained using pypsignifit toolbox v3.0 by fitting the optimal psychometric function to each data set using the logistic function, which implements the maximum likelihood method described by Wichmann and Hill [81] [82]. Those subjects for which goodness of fit was not obtained are denoted by (*) and are not used in the resulting mean or standard deviation values reported in Table 3.6. Mean values for aperture size JND range from 0.50-0.66 mm. A one-way ANOVA reveals no statistical differences between the aperture size JNDs at different peak pressure levels ($p=0.37$)[1].

[1]Notice that in both the JND size and pressure experiments, some subjects commented that their stimulated finger pad began to feel cold in the latter stages of the experiment. To prevent or minimize these types of effects, both psychophysics studies were broken into small blocks with subjects taking breaks in between blocks. Additionally, the order in which different experiment levels were performed was always randomized, so that any possible effects of finger skin temperature on tactile discrimination were distributed equally throughout the experiment.

Table 3.6: Summary of JND Size (mm)

Subject	Peak Pressure (kPa)		
	10 kPa	**30 kPa**	**50 kPa**
1	0.36	0.30	1.23
2	0.60	0.39	0.46
3	∗1.05	∗1.74	0.76
4	∗0.43	0.85	0.51
5	0.56	0.33	∗0.33
6	0.37	0.31	0.92
7	0.74	∗0.43	0.70
8	∗0.61	0.66	∗0.71
9	1.16	0.62	0.79
10	0.24	0.12	0.26
11	0.19	0.22	0.24
12	0.71	0.43	0.60
13	∗0.38	∗0.03	0.43
14	∗1.19	1.23	0.83
15	∗0.83	0.51	∗0.61
16	0.45	∗0.14	0.82
Mean	**0.54**	**0.50**	**0.66**
Std. Dev.	**0.29**	**0.31**	**0.28**

* Indicates JND obtained from a psychometric curve which did not demonstrate goodness of fit to the response proportion (P) data. Values with $*$ are excluded from mean values.

3.4 Conclusions

An air-jet lump display is a promising technique to elicit the percept of a lump to the skin. This display type is simple in design and can display a wide variety of "lump-like" pressure profiles to the finger by controlling only two control parameters (pressure, aperture size). The results of the characterization study indicate that output peak pres-

sure is dependent on both supply pressure and aperture size, while the pressure profile width is solely dependent on the aperture size. In this manner, different combinations of perceptual cues of rendered lumps can be reproduced. JND experiments provide benchmark values for future psychophysical experiments with this display type. An important consideration is that the intended target of the pneumatic lump display is the human finger, which is (in comparison with the tactile sensor array used for the characterization) not firm or flat, exhibiting compliance and curvature which change the local shape of the finger as it is stimulated. The psychophysical studies implicitly account for these complex factors of skin compliance, finger curvature, and perceptual capabilities as a function of the stimulus parameters, which can not be accounted for during tactile quantitative characterization, whereas the tactile sensor array characterize the output of the pneumatic air-jet display and capture the isolated effects of the control parameters upon the display output. As previously mentioned, this characterization has furnished the theoretical framework for the development of an actual haptic device [A4] used in a training platform for surgeons. Next steps will be aimed at a proper integration in a RMIS systems.

Part II

Kinaesthetic Cues: Hand Pose Sensing Devices

Chapter 4

Synergy-based Hand Pose Sensing

I deal now with the problem of correct hand posture estimation from hand pose sensing devices. According to the definition of Bastian [41], since kinaesthesia represents the intrinsic capability to sense the position of our limbs and trunk and hence it is associated to posture processing, this problem can be regarded as a kinaesthetic problem. As already described for cutaneous sensing, here the goal is to find suitable reductions and simplifications, with minimum loss of information, in order to guarantee a consistent pose reconstruction even if measurements are inaccurate and insufficient. This can be the case of low-cost glove-based systems. Indeed, cost limits affect the quality of measures which can be generated through an imperfectly known model, subject to noise and usually less than the number of the hand DoFs. In these situations, the concept of synergies in motor domain is very useful, because it affirms that the dimensionality of the kinematic space of the human hand is significantly smaller than that individuated by its mechanical DoFs.

In this chapter, after an introduction about kinematic hand synergies, I describe sensing gloves and provide solutions to improve their reconstruction performance and design by exploiting the knowledge on how humans most frequently use their hands. Firstly, to increase

the accuracy of pose estimation without modifying the glove hardware (hence basically at no extra cost) I propose to collect, organize, and exploit information on the probabilistic distribution of human hand poses in common tasks [A5]. I discuss how a database of such an *a priori* information can be built, represented in a hierarchy of correlation patterns or synergies, and fused with glove data in a consistent way, so as to provide a good hand pose reconstruction in spite of insufficient and inaccurate sensing data.

In the second part, I focus on the problem of optimal design of pose sensing gloves, i.e. the problem of individuating which DoFs (generally a reduced number of total DoFs of the hand kinematic model subject to noise) have to be measured in order to maximize the information acquired by the measurement process, and hence increasing reconstruction performance [A6]. To achieve the optimal design configuration, closed-form solutions relying on the geometrical synergy definition (i.e. principal components of the *a priori* covariance matrix) as well as gradient flow-based techniques are provided and discussed, for both noise-free and noisy sensors. Simulations and experiments on a given low-cost glove are reported, which demonstrate the effectiveness of the proposed strategies.

Notice that all these methods are valid to reconstruct hand postures in static grasping tasks, since they depend on the structure of the *a priori* database. In the case I analyze this database consists of grasp poses and can be represented by means the so-called *postural synergies* [16], (see Introduction). However, since human hands share many commonalities in how they are shaped and used across everyday tasks, the here discussed strategies can be generalized to other types of poses, e.g. for sign language applications [83, 84], by suitably extending the *a priori* set. Moreover, since modulation of the coefficients of linear combinations of PCs can take into account for a wide range of basic grasping movements [16, 36], the techniques I propose can be used also for dynamic hand configuration estimation, in which hand movement is analyzed as a series of static grasp frames.

The performance enhancement and optimal design solutions I dis-

cuss in this chapter are contained in an Italian patent proposal submitted on behalf of University of Pisa [A10].

4.1 Kinematic Synergies and Their Applications

As already said in the Introduction, despite hand complexity, simultaneous motion and force of the fingers occurs in a consistent fashion and is characterized by coordination patterns that reduce the number of independent degrees of freedom to be controlled [14]. This experimental evidence, which can be explained in terms of central (neural inputs are shared by different units acting on different digits) and peripheral (e.g. interconnections between tendons of hand muscles) constraints in the neuromuscular apparatus, summarizes well the concept of *hand synergies*, which in a broad sense indicate the aforementioned covariation schemes observed in digit movements and contact forces.

Under a kinematic point of view, many studies have analyzed and exploited this concept for the description of simultaneous movement patterns of fingers and thumb, e.g. in the early stage of development (palmar grasp reflex) [85] and for grasp posture classification [86]. Spatial and temporal coordinations of digit movements were then studied in serial tasks with one digit isolated motion [87, 88] (as typing) and more digits (as finger spelling); these coordination schemes were proved to facilitate hand shape recognition [89]. The main finding of the aforementioned studies is that in addition to the *focal movement* of the finger used to type, unnecessary motion for task accomplishment were observed at other fingers, with higher correlation for adjacent digits.

Moreover, in [88] it was shown that, due to musculoskeletal and neural constraints, the number of DoFs independently controlled by the nervous system is reduced since only a few principal components (PCs)[1] characterize motion of 17 DoFs of the hand.

[1]The concept of synergies has been often quantified and defined through dimen-

Referring to grasping tasks, systematic covariations of joint angular excursions of hand postures were described in terms of synergies as well. Indeed, it was shown that individuated finger motions were phylogenetically superimposed on basic grasping movements [90]. The paper that has mainly inspired my work is [16], which first analyzed hand *postural synergies* for grasping by means of PCA. In this work, authors focused on central contributions to hand posture modulation, analyzing a large number of different imagined grasped object, thus avoiding any mechanical interference as it would result from the contact with real elements. Subsequent analogous work with physical objects led to coherent observations [91]. In [16] it was demonstrated that only a few linear combinations of hand DoFs (in this case a 15 DoF kinematic model was considered) is sufficient to take into account most of the variance in the set. Moreover, a *gradient* in PCs was individuated; lower order PCs take into account covariation patterns for metacarpophalangeal (MCP) and interphalangeal (IP) joints, which are mainly responsible for coarse hand opening and closing, while higher order PCs are used for fine hand shape adjustments.

Therefore, even if PCs do not have any physical significance and can not be used to quantitatively evaluate the contributions of peripheral and central constraints, they can somehow furnish an expression of the covariation patterns that, as previously reported, exist and are not obligatory for task accomplishment. Furthermore, although task-dependencies w.r.t. the type and number of elicited PCs have been observed [92–94], some commonalities of digit movement coordination schemes exist across tasks, as it results e.g. from [95], in which PCs employed in haptic exploration provide also grasp pose reconstruction. For a more complete review of kinematic synergies see e.g. [14].

The main idea shared by all the above discussed studies is that there are some inner hand representations of increasing complexity, which allow to reduce the number of hand DoFs to be used according to the desired level of accuracy required for a motor task. From

sionality reduction techniques (principal components analysis, PCA and singular value decomposition, SVD)

a *controllability* point of view, this idea has been then adopted in robotics to define simplified approaches for the design and control of artificial hands with a reduced number of controls [18–21, 96, 97]. Among the others, in pioneer papers such as [20,21], synergy concept is used to reduce the dimensionality of the search space for automated grasp synthesis and applied in an effective manner to derive pre-grasp shapes for complex robotic hands. In [97] synergistic finger coupling is exploited using a dimensional reduction technique to drive a 12 DoF hand with only 8 independent actuators; in [19] principal component analysis of real/world data on a variety of human hand postures was used to calculate characteristic patterns of actuation, or synergies, which were combined to control a 17 DoF 5 fingered robot hand (which was proved to be able to reproduce a wide range of hand shapes with only 2 DC motors).

On the other hand, from the *observability* point of view, these considerations also suggest that it is possible to reduce the number of independent DoFs to be measured in order to obtain hand pose estimation with a given level of approximation. An application of this concept was developed in [36] for hand avatar animation. The key of this approach was to exploit synergy variables [98] to approximate principal motion components, thus improving the realism of animation. Virtual springs, which couple the avatar tips to the corresponding operator's tips, were used to compute the forces necessary (for the avatar fingertips) to track real finger trajectories. These forces were then transformed in the synergy-space general forces and used to recursively estimate the new synergy variables, which characterize the whole-hand configuration. This kind of estimation, which is dependent on the number of synergy variables, was proved to be good enough in qualitative terms but no numerical evaluation was furnished.

In this work, the idea is to use the information embedded in a known grasp set, which expresses the postural constraints for multi-fingers joints, to improve the reconstruction of the hand posture in static grasping tasks when only a limited and inaccurate number of

measures are available by low-cost sensing gloves for gesture measurement. Moreover, this information is also used to inspire an optimal design of these systems in a minimum variance (MV) sense.

Glove-based devices[2] consist of an array of sensors, electronics for data processing and acquisition, and a support for the sensors, typically a cloth glove of Lycra®/where sensors are sewn (see figure 4.8). This kind of glove is worn by the user and can record data related to his/her hand configuration/motion. Sensing gloves provide useful interfaces for human-machine and haptic interaction in many fields like, for example, virtual reality, musical performance, video games, tele-operation and robotics [83, 84]. However, the widespread commercialization of electronic gloves imposes limits on the production costs in terms of the amount and the quality of the sensors adopted. As a consequence, the correctness of the hand pose reconstruction obtained by these devices might be compromised. To overcome this problem, in the next section I provide an optimal hand pose estimation technique based on Bayes'inference.

4.2 Performance Enhancement

Two different approaches have been followed to achieve this goal. The first one, which solves a constrained optimization problem of multinormal probability density function (pdf), is mainly adopted with accurate measured data. The second approach deals with noisy measured data and relies on classic Minimum Variance Estimation (MVE). To validate this technique I considered limited measurements from a set of grasp postures acquired with a low cost sensing glove and an optical tracking system, the latter one representing an accurate reference for pose reconstruction. Effects of noise are also taken into account.

[2]Hereinafter the words "glove-based systems", "sensing gloves", "electronic gloves" will be used as synonyms

4.2.1 The Hand Posture Estimation Algorithm

Let consider a set of measures $y \in \mathbb{R}^m$ given by a sensing glove. By using a n degree of freedom kinematic hand model, I assume a linear relationship between joint variables $x \in \mathbb{R}^n$ and measurements y given by

$$y = Hx + \nu \,, \tag{4.1}$$

where $H \in \mathbb{R}^{m \times n}$ $(m < n)$ is a full rank matrix which represents the relation between measures and joint angles, and $\nu \in \mathbb{R}^m$ is a vector of measurement noise. The goal is to determine the hand posture, i.e. the joint angles x, by using a set of measures y whose number is lower than the number of DoFs describing the kinematic hand model in use. Equation (4.1) represents a system where there are fewer equations than unknowns and hence is compatible with an infinite number of solutions, described e.g. as

$$x = H^{\dagger} y + N_h \xi \,, \tag{4.2}$$

where $H^{\dagger}$ is the pseudo-inverse of matrix H, N_h is the null space basis of matrix H and $\xi \in \mathbb{R}^{(n-m)}$ is a free vector of parameters. Among these possible solutions, the least-squared solution resulting from the pseudo-inverse of matrix H for system (4.1) is a vector of minimum Euclidean norm given by

$$\hat{x} = H^{\dagger} y \,. \tag{4.3}$$

However, the hand pose reconstruction resulting from (4.3) can be very far from the real one. My purpose is to improve the accuracy of the pose reconstruction, choosing, among the possible solution to (4.2), the most likely hand pose. As previously described in Section 4.1, the basic idea is to exploit the fact that human hands, although very complex and possibly different in size and shape, share many commonalities in how they are shaped and used in frequent everyday tasks. Moreover, studies on the human hand in grasping tasks showed that finger motions are strongly correlated according to some coordination patterns, or synergies [16].

To achieve this goal, I use the *a priori* information obtained by collecting a large number N of grasp postures x_i, consisting of n DoFs, into a matrix $X \in \mathbb{R}^{n \times N}$. This information can be summarized by means of a covariance matrix $P_o \in \mathbb{R}^{n \times n}$, which is a symmetric matrix computed as

$$P_o = \frac{(X - \bar{x})(X - \bar{x})^T}{N - 1}\,, \tag{4.4}$$

where $\bar{x}$ is a matrix $n \times N$ whose columns contain the mean values for each joint angle arranged in vector $\mu_o \in \mathbb{R}^n$. I assume that the above described *a priori* information is multivariate normal distributed, and hence can be described by the covariance matrix P_o.

4.2.1.1 Probability Density Function Maximization

I initially consider the case that measurement noise is negligible. The best estimation of the hand posture is given by choosing as optimality criterion the maximization of the probability density function (pdf) of the multivariate normal distribution which describes the *a priori* set, expressed by [99]

$$f(x) = \frac{1}{\sqrt{2\pi \|P_o\|}} \exp\left\{-\frac{1}{2}(x - \mu_o)^T P_o^{-1}(x - \mu_o)\right\}\,. \tag{4.5}$$

This is equivalent to solving the following optimal problem:

$$\begin{cases} \hat{x} = \arg\min\limits_{\hat{x}} \frac{1}{2}(x - \mu_o)^T P_o^{-1}(x - \mu_o) \\ \text{Subject to} \quad y = Hx\,. \end{cases} \tag{4.6}$$

It is interesting to give a geometrical interpretation of the cost function in (4.6), which expresses the square of the Mahalanobis distance [100].

The concept of Mahalanobis distance, which takes into account data covariance structure, is widely exploited in statistics, e.g. in

PCA, mainly for outlier detection [101]. Accordingly, to assess if a test point belongs to a known data set, whose distribution defines an hyper-ellipsoid, its closeness to the centroid of data set is taken into account as well as the direction of the test point w.r.t. the centroid itself. In other words, the more samples are distributed along a given direction, the higher is the probability that the test point belongs to the data set even if it is further from the center.

Taking into account (4.2), the optimal problem defined in (4.6) becomes

$$\begin{cases} \hat{\xi} = \arg\min_{\hat{\xi}} (H^{\dagger}y + N_h\xi - \mu_o)^T P_o^{-1} (H^{\dagger}y + N_h\xi - \mu_o) \\ \text{Subject to} \quad y = Hx\,. \end{cases} \tag{4.7}$$

By using classical optimization procedures I obtain $\hat{\xi} = (N_h^T P_o^{-1} N_h)^{-1} N_h^T P_o^{-1}(\mu_o - H^{\dagger}y)$ and, substituting in (4.2), after some algebras, the estimation of the hand joint angles is

$$\begin{aligned} \hat{x} = [I - N_h(N_h^T P_o^{-1} N_h)^{-1} N_h^T P_o^{-1}] H^{\dagger}y + \\ + N_h(N_h^T P_o^{-1} N_h)^{-1} N_h^T P_o^{-1} \mu_o\,. \end{aligned} \tag{4.8}$$

Problem (4.6) can be also solved through the method of Lagrange multipliers. Let introduce a new variable $\lambda \in \mathbb{R}^m$ and consider

$$L = \frac{1}{2}(x - \mu_o)^T P_o^{-1}(x - \mu_o) + \lambda^T (Hx - y)\,. \tag{4.9}$$

By imposing $\frac{\partial L}{\partial x} = \frac{\partial L}{\partial \lambda} = 0$, it is obtained

$$\hat{x} = \mu_o - P_o H^T (H P_o H^T)^{-1} (H\mu_o - y)\,. \tag{4.10}$$

This solution can be easily shown to be equivalent to (4.8).

Finally, it is interesting to observe that the least-squared and pdf maximization methods have a direct application in case of only single-DoF sensors are used in the devices (discrete sensing gloves, see Section 4.3). In this case, H is a selection matrix whose rows are vectors

of the canonical basis in $\mathbb{R}^n$ and the least-squared solution is simply given as $\hat{x} = H^T y$. In order to improve the hand pose reconstruction by the *a priori* information, it is possible to easily maximize $E[x|y]$ in terms of multinormal conditional distribution [102]. Indeed, in this case vector y defines a precise subset of the state variables, being X_1, whose values are known by means of the measurement process, while X_2 indicates the rest of state variables to be estimated. This definition allows to partition the *a priori* covariance matrix as

$$\left(\frac{X_1}{X_2}\right) \Longrightarrow P_o = \left(\frac{P_{o11}|P_{o12}}{P_{o21}|P_{o22}}\right) \tag{4.11}$$

as well as the *a priori* mean $\mu_o = (\mu_{o1}|\mu_{o2})$. The estimation of X_2 is easily derived as

$$\hat{X_2} = E[X_2|X_1 = y] = \mu_{o2} + P_{o21}P_{o11}^{-1}(y - \mu_{o1})\,. \tag{4.12}$$

4.2.1.2 Minimum Variance Estimation

Results in previous section are valid in the condition of $\nu \approx 0$. When noise is not negligible, the role of *a priori* is more emphasized. Here I consider noise effects and propose an algorithm based on the Minimum Variance Estimation (MVE) technique. This method minimizes a cost functional which expresses the weighted Euclidean norm of deviations, i.e. cost functional $J = \int_X (\hat{x} - x)^T S(\hat{x} - x)dx$, where S is an arbitrary, semidefinite positive matrix. Under the hypothesis that ν has zero mean and Gaussian distribution with covariance matrix R, the solution for the minimization of J is achieved as $\hat{x} = E[x|y]$, where $E[x|y]$ represents the *a posteriori* pdf expectation value. The estimation $\hat{x}$ can be obtained as in [103] by

$$\hat{x} = (P_o^{-1} + H^T R^{-1} H)^{-1}(H^T R^{-1} y + P_o^{-1}\mu_o)\,, \tag{4.13}$$

where matrix $P_p = (P_o^{-1} + H^T R^{-1} H)^{-1}$ is the *a posteriori* covariance matrix, which has to be minimized to increase information about the system. This result represents a very common procedure in applied

optimal estimation when there is redundant sensor information. In under-determined problems, it is only thanks to the *a priori* information, represented by P_o and μ_o, that equation (4.13) can be applied (indeed, $H^T R^{-1} H$ is not invertible).

When R tends to assume very small values, the solution described in equation (4.13) might encounter numerical problems. However, by using the Sherman-Morrison-Woodbury formulae,

$$(P_o^{-1} + H^T R^{-1} H)^{-1} = P_o - P_o H^T (H P_o H^T + R)^{-1} H P_o \tag{4.14}$$

$$(P_o^{-1} + H^T R^{-1} H)^{-1} H^T R^{-1} = P_o H^T (H P_o H^T + R)^{-1}\,, \tag{4.15}$$

equation (4.13) can be rewritten as

$$\hat{x} = \mu_o - P_o H^T (H P_o H^T + R)^{-1} (H\mu_o - y)\,, \tag{4.16}$$

and the *a posteriori* covariance matrix becomes $P_p = P_o - P_o H^T (H P_o H^T + R)^{-1} H P_o$ (see (4.14)). By placing $R = 0$ in (4.16), it is possible to obtain equation (4.10) and the *a posteriori* covariance matrix becomes

$$P_p = P_o - P_o H^T (H P_o H^T)^{-1} H P_o \tag{4.17}$$

Notice that probability density function maximization approach is a peculiar case of the here described MVE technique. For this reason in the following sections I will always refer to the reconstruction technique as MVE for both noise-free and noisy measures and solution (4.16) is used for the reconstruction, with $R = 0$ or $R \neq 0$, respectively.

4.2.2 Model and Data capture

To assess hand pose reconstruction effectiveness, I adopted, without loss of generality, the 15 DoF model[3] used in [16, 96] and reported

[3]The human hand, considering only fingers and metacarpal joints, has 23 DoFs [83]. Various models have been proposed in literature, which try to reproduce hand and wrist kinematics at different levels of approximation, e.g. [104,105]

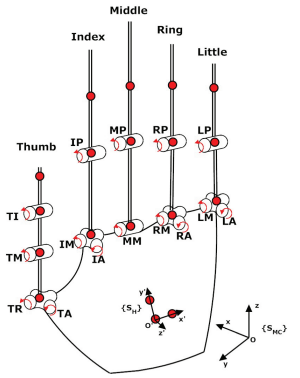

DoFs	Description
TA	Thumb Abduction
TR	Thumb Rotation
TM	Thumb Metacarpal
TI	Thumb Interphalangeal
IA	Index Abduction
IM	Index Metacarpal
IP	Index Proximal
MM	Middle Metacarpal
MP	Middle Proximal
RA	Ring Abduction
RM	Ring Metacarpal
RP	Ring Proximal
LA	Little abduction
LM	Little Metacarpal
LP	Little Proximal

Figure 4.1: Kinematic model of the hand with 15 DoFs. Markers are reported as red spheres.

in figure 4.1. A large number of static grasp positions were collected using 19 active markers and an optical motion capture system (Phase Space, San Leandro, CA, USA). More specifically, all the grasps of the 57 imagined objects described in [16] were performed twice by subject AT (M,26), in order to define a set of 114 *a priori* data. Moreover, 54 grasp poses of a wide range of different imagined objects were executed by subject LC (M,26) [4]. The set of the latter poses will be referred hereinafter as *validation set*, since these poses can be assumed to represent accurate reference angular values for successive comparisons with the obtained hand pose reconstructions. For this reason, these data were recorded in parallel with the sensing glove and the Phase Space system, to achieve also a glove calibration.

I consider the processed hand poses acquired with Phase Space as reliable approximations of real hand positions, given the high accuracy provided by this optical system to detect markers (the amount of static marker jitter is inferior than 0.5 mm, usually 0.1 mm) and assuming a linear correlation (due to skin stretch) between marker

[4] All these data and more information about hand pose acquisitions are available at http://handcorpus.org/

motion around the axes of rotation of the joint and the movement of the joint itself [106]. Since the sensing glove perfectly adapts to subject hand shape when it is worn, the latter assumption is still reasonable also in this case, even if departures from real reference configurations can happen.

None of the subjects had physical limitations that would affect the experimental outcomes. Data collection from subjects in this study was approved by the University of Pisa Institutional Review Board. Markers were placed on the glove, at joint locations, referring to [104]

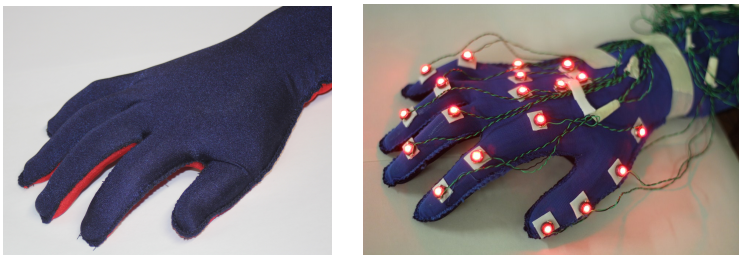

Figure 4.2: The sensing glove by University of Pisa (on the left) and sensing glove with added markers (on the right).

(see figure 4.2). Four markers were used for the thumb and three markers for each of the rest of the fingers. Additional three markers placed on the dorsal surface of the palm defined a local reference system S_H. Marker positions were sampled at 480 Hz and were given referring to the global reference system S_{MC}, as it was defined during the calibration phase of the acquisition system.

Joint angles were computed w.r.t. S_H by means of the *ikine* function of Robotics Toolbox for Matlab. This function implements an iterative algorithm of kinematic inversion, which has been suitably modified by adapting computational tolerance to guarantee numerical convergence. A moving average filter was exploited for data pre-filtering, thus enhancing Signal Noise Ratio (SNR). As a preliminary phase, the hand was posed in a reference position, where fingers flexion-extension is nearly zero, and phalanges length and eventual

offset angles were computed.

I test the normality assumption on the acquired *a priori* set by means of a Q-Q plot-based graphical method for multidimensional variables [107, 108]. The quantile plot is usually obtained by plotting the ordered estimated Mahalanobis measures against the chi-square distribution quantiles. If normality is met, the graph should display a fairly straight line on the diagonal (i.e. 45° slope line). In my case, the linear fitting with straight 45° slope line provides an adjusted r-squared coefficient of 0.6. This result suggests that the normality assumption is reasonable even if not fully met. However, the Gauss-Markov theorem [109] ensures, that the MVE is the Best Linear Unbiased Estimate (BLUE) in the minimum-variance sense even for non-Gaussian a priori distributions [110]. In addition, central limit theorem [102] can guarantee, to some extents, the application of MVE method to cases that depart from the strict linear-Gaussian hypothesis for *a priori* (and noise distribution as well).

4.2.3 Simulation Results

I simulated an ideal glove which is able to measure only metacarpal joints (see figure 4.1) by using the acquisitions from the *validation set*. MVE reconstruction performance is compared with the one obtained by means of the pseudo-inverse based method (hereinafter referred as Pinv) (4.3).

The measurement matrix for this simulated glove is referred as H_s. Estimation results obtained with the reconstruction algorithms are compared with the corresponding reference values from the *validation set* to compute errors.

An additional random zero-mean Gaussian noise with standard deviation of 7° is considered on each measure. This value is chosen in a cautionary manner, based on data about common technologies and tools used to measure hand joints positions [111]. More specifically, this datum expresses the reliability threshold of manual goniometry with skilled therapists in measures for rehabilitation procedures [112].

DoF	Mean±Std		Max Error		p-values
	MVE	**Pinv**	**MVE**	**Pinv**	
TA	10.74±8.45	14.04±11.10	31.65	32.74	**0.1794**
TR	7.16±4.54	27.62±10.24	19.50	45.65	0
TM∗	0	0	0	0	–
TI	4.81±3.68	6.74±5.54	19.69	23.16	**0.1179**
IA	11.96±5.33	6.27±3.27	26.35	14.90	0
IM∗	0	0	0	0	–
IP	13.26±7.06	28.87±13.79	27.46	59.41	0
MM∗	0	0	0	0	–
MP	12.35±7.75	29.84±13.64	29.94	57.78	0
RA	3.45±2.43	10.17±3.78	9.51	16.45	0
RM∗	0	0	0	0	–
RP	13.40±9.65	34±13.88	39.33	65.43	0
LA	11.33±5.87	24.28±5.18	24.47	37.89	0 ⋄
LM∗	0	0	0	0	–
LP	11.94±9.50	26.50±13.65	26.58	63.64	0

1 ←——————— 0

p-values

∗ indicates a measured DoF.

Table 4.1: Average estimation errors and standard deviations for each DoF [°] for the simulated acquisitions without noise. MVE and Pinv methods are considered. Maximum errors are also reported as well as p-values from the evaluation of DoF estimation errors between MVE and Pinv. A color map describing p-values is also added to simplify result visualization. ⋄ indicates that T_{eq} test is exploited for the comparison. ‡ indicates a T_{neq} test. When no symbol appears near the tabulated values, it means that U test is used. **Bold** value indicates no statistical difference between the two methods under analysis at 5% significance level. When the difference is significative, values are reported with a 10^{-4} precision. p-values less than 10^{-4} are considered equal to zero.

DoF	Mean±Std		Max Error		p-values
	MVE	**Pinv**	**MVE**	**Pinv**	
TA	8.93±6.64	14.04±11.10	31.12	32.74	0.0496 ‡
TR	8.10±5.66	27.62±10.24	22.53	45.65	0
TM*	2.96±2.16	5.62±4.25	8.25	17.01	0.0009
TI	6.80±4.95	6.74±5.54	20.10	23.16	**0.66**
IA	10.69±5.50	6.27±3.27	25.45	14.90	0
IM*	4.21±3.24	5.40±3.57	13.71	13.86	**0.07**
IP	14.63±7.86	28.87±13.79	34.16	59.41	0
MM*	4.80±2.74	5.23±3.97	10.35	20.03	**0.95**
MP	13.87±8.39	29.84±13.64	38.19	57.78	0
RA	3.13±2.18	10.17±3.78	9.00	16.45	0
RM*	4.62±3.42	5.28±3.73	13.75	17.56	0.34 ◇
RP	16.98±11.47	34.00±13.88	50.58	65.43	0
LA	8.99±5.16	24.28±5.18	20.44	37.89	0 ◇
LM*	4.27±3.14	5.78±4.30	15.47	18.71	**0.09**
LP	14.89±9.95	26.50±13.65	48.10	63.64	0 ‡

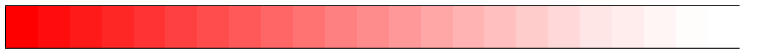

1 ←——————— 0

p-values

* indicates a measured DoF.

Table 4.2: Average estimation errors and standard deviations for each DoF [°] for the simulated acquisitions with noise. MVE and Pinv methods are considered. Maximum errors are also reported as well as p-values from the evaluation of DoF estimation errors between MVE and Pinv. A color map describing p-values is also added to simplify result visualization. ◇ indicates that T_{eq} test is exploited for the comparison. ‡ indicates a T_{neq} test. When no symbol appears near the tabulated values, it means that U test is used. **Bold** value indicates no statistical difference between the two methods under analysis at 5% significance level. When the difference is significative, values are reported with a 10^{-4} precision. p-values less than 10^{-4} are considered equal to zero.

The estimation performance is evaluated in terms of estimation errors. Pose estimation errors (i.e. the mean of DoF absolute estimation errors computed for each pose), and DoF absolute estimation errors are considered and averaged over all the number of reconstructed poses in the *validation set*. I perform these two types of analysis in order to furnish a more clear result comprehension. Indeed, pose estimation errors provide an useful but only global indication about the technique outcomes, potentially leading to some biased observations. For example, it might be the case in which a hand pose reconstruction with all the fingers in a "slightly right" position produces the same average error of a hand pose reconstruction with all the fingers but one in the right position and the one mispositioned very distant from the real one. Therefore, to overcome this limitation I also analyze each DoF estimation accuracy. In addition, some reconstructed poses are displayed w.r.t. the reference ones, to provide a qualitative representation mainly focused on reconstruction *likelihood* exhibited by reconstructed poses with common grasp postures. However, it is important to notice that MV techniques are designed to minimize error statistics but may lack robustness to outliers. Therefore they might not be the preferable choice when the main goal to achieve is to minimize worst-case sensing errors rather than error statistics.

Statistical differences between estimated pose and joint errors obtained with above described techniques were computed by using classic tools, after having tested for normality and homogeneity of variances assumption on samples (through Lilliefors' composite goodness-of-fit test and Levene's test, respectively). Standard two-tailed t-test (hereinafter referred as T_{eq}) is used in case of both the assumptions are met, a modified two-tailed T-test is exploited (Behrens-Fisher problem, using Satterthwaite's approximation for the effective degrees of freedom, hereinafter referred as T_{neq}) when variance assumption is not verified and finally a non parametric test is adopted for the comparison (Mann-Whitney U-test, hereinafter referred as U) when normality hypothesis fails. Significance level of 5% is assumed and p-values less than 10^{-4} are posed equal to zero.

In case of noise-free measurements, mean absolute pose error obtained with MVE is $6.69 \pm 2.38°$, while with Pinv it is equal to $13.89 \pm 3.09°$, with observed statistical difference between the two methods ($p \simeq 0$, T_{eq}). What is noticeable is that MVE provides a better pose estimate than the one obtained using Pinv in terms of both mean pose absolute estimate error and considering maximum absolute pose estimation error (MVE: 13.18° vs. Pinv: 20.82°).

In case of noisy measurements, mean absolute pose estimation error with MVE is $8.52 \pm 2.86°$, while with Pinv is $15.71 \pm 3.08°$. Also in this case statistical difference is observed between MVE and Pinv ($p \simeq 0$, T_{neq}). Notice that MVE still provides the best pose estimate and the smallest pose absolute maximum error (MVE: (17.14° vs. Pinv: 23.39°).

In table 4.1 absolute average estimation errors for each DoF with their corresponding standard deviations are reported for MVE and Pinv procedures. Noise-free measures are considered. Significant statistical differences between the two techniques are found for all DoFs estimation errors, except for those directly measured and for TA and TI, the latter ones referring to thumb finger. This fact might be partially explained by the difficulties in modelling thumb phalanges under a kinematic point of view. MVE exhibits an estimation performance in terms of mean error which is better or not statistically different from the one achieved by Pinv, except for IA DoF; however, in this case the difference between the mean errors for the two methods is the smallest (less than 6°) among all the differences computed for the significantly different estimated DoFs. MVE provides the smallest maximum errors except for IA DoF; however the difference with maximum error obtained using Pinv is less than 12°.

In table 4.2 values of each DoF estimation absolute error averaged over all poses, with their corresponding standard deviations, are reported in case of noise. Maximum errors are calculated and statistical significance in result comparison for each DoF estimation, between the aforementioned techniques, is indicated in table 4.2. Notice that MVE furnishes the best performance with average estimation errors which

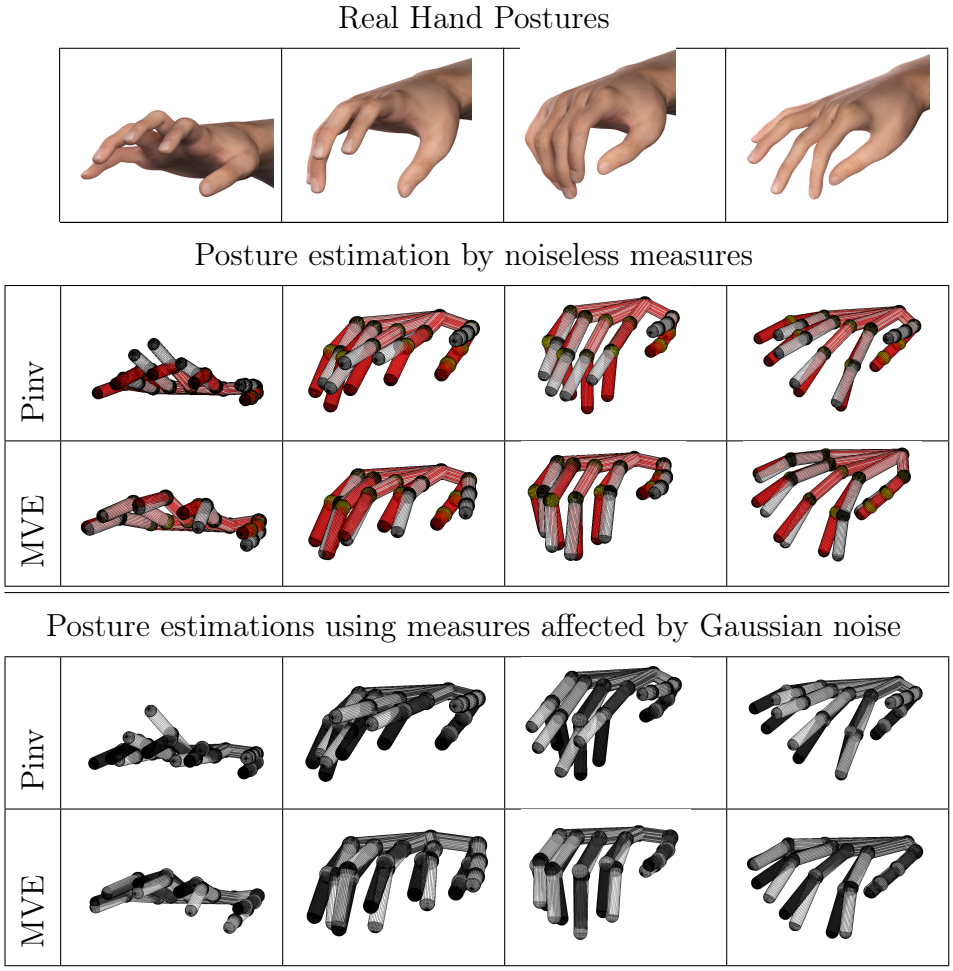

Figure 4.3: Hand pose reconstructions with Pinv and MVE algorithms by using a selection matrix H_s which allows to measure TM, IM, MM, RM and LM (see figure 4.1). In color the "real" hand posture whereas in white the estimated one.

are always inferior or not statistically different from the ones obtained using Pinv algorithm, except for IA DoF for which Pinv produces the

smallest average estimation error. However, the difference between IA mean errors calculated with the two procedures is less than 3°. No statistically significant difference are found between MVE and Pinv for TI, IM, MM, RM and LM DoFs. Notice that the DoFs for which no statistical difference is observed between MVE and Pinv are DoFs directly measured or they refer to thumb finger phalanx. Considering maximum errors, MVE still exhibits the best results, except for IA DoF. This fact is important, since MVE is suited for error statistics minimization and can be sensitive to worst-case sensing cases.

In figure 4.14 some reconstructed poses are displayed in comparison with their corresponding reference values achieved with Phase Space system, with and without noise. What is noticeable is that MVE qualitatively shows the best reconstruction results, thus maintaining the likelihood with common grasping poses because of the *a priori* information, unlike Pinv.

4.2.4 Experimental Results

I tested for the effectiveness of the reconstruction procedure using a sensorized glove based on Conductive Elastomer (CE). CE strips are printed on a Lycra®/cotton fabric in order to follow the contour of the hand, see figure 4.2. Connection to 20 different sensor segments of the polymeric strip is realized using additional conductive elastomer elements printed on the dorsal side of the glove [113], which will be also referred as University of Pisa glove.

Since CE materials present piezo-resistive characteristics, sensor elements corresponding to different segments of the contour of the hand length change as the hand moves. These movements cause variations in the electrical properties of the material, which can be revealed by reading the voltage drop across such segments. The sensors are connected in series thus forming a single sensor line while the connections intersect the sensor line in the appropriate points. An *ad hoc* electronic front-end was designed to compensate the resistance variation of the connections, made by the same material of the sensors,

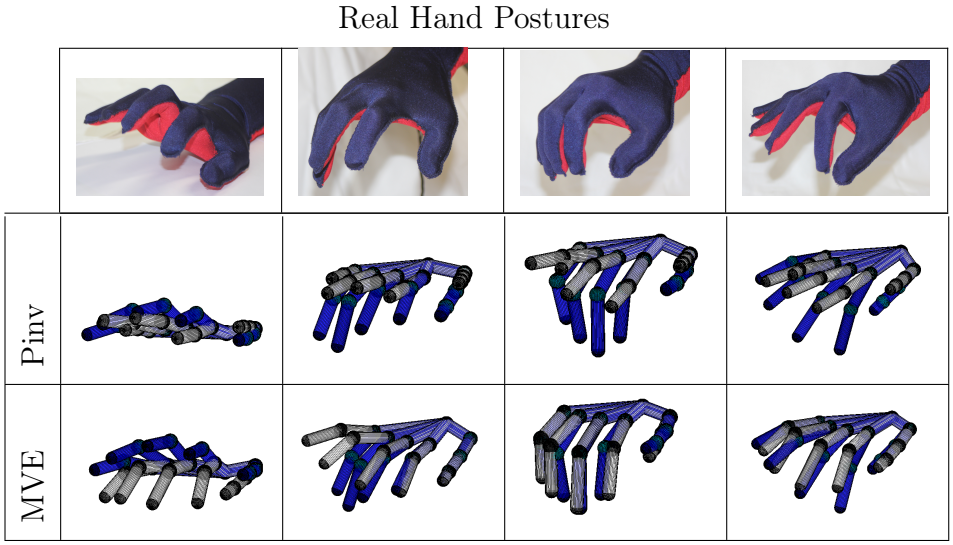

Figure 4.7: Hand pose reconstructions with Pinv and MVE algorithms, with measures given by sensing glove. In blue the "real" hand posture whereas in white the estimated one.

using an high input impedance stage.

Data coming from the front-end are then low pass filtered, digitalized and acquired by means of a general purpose DAQ card, and finally elaborated on a computer.

This glove can be considered as a continuous sensing device as it will be more clearly described in Section 4.3 since each sensor consists of a single sensing line all over different joints. Data processing is based on the assumption that changes in the electrical characteristics of the sensor elements, corresponding to different segments of the contour of the hand, are associated with changes in the angle of the joint such sensor elements cut across. Furthermore, it was assumed that the hand aperture linearly relates to changes in the electrical characteristics of the sensor elements occurring as joint angles change. Considering this, a function that maps the sensor raw

DoF	Mean±Std		Max Error		p-values
	MVE	**Pinv**	**MVE**	**Pinv**	
TA	12.12±9.98	14.37±10.78	36.63	34.28	**0.28**
TR	9.20±7.13	26.46±10.49	26.34	46.43	0
TM∗	4.36±3.73	6.43±4.44	13.25	18.50	0.0093
TI	14.56±9.96	7.84±5.47	33.25	22.38	0.0008
IA	9.82±6.89	7.10±5.08	29.60	21.18	0.0381
IM∗	15.27±11.86	16.48±12.62	46.76	43.58	**0.58**
IP	9.60±7.65	31.47±14.70	27.40	61.11	0
MM∗	14.40±12.84	19.88±14.58	53.03	51.47	0.0232
MP	6.80±6.49	24.36±9.85	24.74	43.72	0
RA	6.20±4.31	5.69±4.72	15.72	20.90	**0.51**
RM∗	19.00±13.44	19.22±11.81	61.98	46.32	**0.67**
RP	8.98±8.91	31.51±13.98	32.24	60.62	0
LA	11.42±8.50	32.24±6.98	29.59	48.11	0
LM∗	17.37±12.51	17.98±11.81	58.40	45.05	**0.26**
LP	8.43±6.36	23.90±12.53	26.07	56.21	0

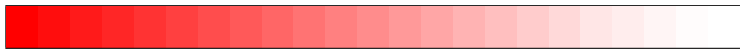

1 ←——————— 0

p-values

* indicates a measured DoF.

Table 4.3: Average estimation errors and standard deviations for each DoF [°], for the sensing glove acquisitions. MVE and Pinv methods are considered. Maximum errors are also reported as well as p-values from the evaluation of DoF estimation errors between MVE and Pinv. A color map describing p-values is also added to simplify result visualization. ⋄ indicates that T_{eq} test is exploited for the comparison. ‡ indicates a T_{neq} test. When no symbol appears near the tabulated values, it means that U test is used. **Bold** value indicates no statistical difference between the two methods under analysis at 5% significance level. When the difference is significative, values are reported with a 10^{-4} precision. p-values less than 10^{-4} are considered equal to zero.

data to joint angles was designed. A linear regression model having hand aperture as dependent variable and the output of the sensor elements as independent variables was built. Fitting of the model was achieved using a calibration phase. Subjects were instructed to perform two fixed hand gesture, flat and grip, corresponding respectively to the minimum and maximum elongation of sensor's length. In the present study, long finger flexion-extension recognition has been obtained by means of an updated multi-regressive model having the metacarpophalangeal (MCP) flexion-extension angles of the five long fingers as dependent variables and the outputs of CE sensor covering MCP joints as independent ones. According to the hand kinematic model adopted in this work they are referred as to TM, IM, MM, RM, LM. The model parameters are identified by measuring the sensor status in two different position: (1) hand totally closed (90 degrees), (2) hand totally opened (0 degrees). For more information about the design and structure of the here described sensing glove and the signal processing system employed see e.g. [113–115].

This sensorized glove represents one of the most recent and inexpensive envisions in glove device literature. However, this solution is limited by some factors which can reduce its performance, e.g cloth support which affects measurement repeatability as well as hysteresis and non linearities due to piezo-resistive material properties. Indeed, this kind of glove is suitable for general opening/closening hand movement measurement but not for fine hand adjustments. Moreover, the assumptions done for data processing (the relationship between joint angle and sensors as well the linearity between hand aperture and electrical property changes) and the calibration phase which is based only on two-points fitting can act like potential sources of errors. To overcome the latter point a new calibration was performed to estimate the measurement matrix.

4.2.4.1 Results and Discussions

Firstly I obtained an estimation of the glove measurement matrix H_g, i.e. $\hat{H}_g$. For this purpose, a calibration phase was performed by collecting a number of poses N in parallel with the glove and the position optical tracking system. This number has to be larger or equal than the dimension of the state to estimate, i.e. $N \geq 15$. $X_c \in \mathbb{R}^{15\times 15}$ collects the reference poses, while matrix $Z_c \in \mathbb{R}^{5\times 15}$ organizes the measures from the glove. These measures represent the values of the signals referred to measured joints, averaged over the last 50 acquired samples. For the acquisition a DAQ card which works at 250 kS/s (NI PCI-6024E by National Instruments) has been used within Matlab/Simulink environment.

Matrix $\hat{H}_g$ is obtained by exploiting the relation $Z_c = \hat{H}_g X_c$ as

$$\hat{H}_g = Z_c((X_c^T)^\dagger)^T \,. \tag{4.18}$$

Measurement noise has been characterized in terms of fluctuations w.r.t. the aforementioned average values of the measures, thus obtaining noise covariance matrix R . Noise level is less than 10% measurement amplitude; however consistent errors in the measurement matrix estimation might be obtained due to intrinsic non-linearities and hysteresis of glove sensing elements.

The average absolute pose estimation error with MVE is $10.94 \pm 4.24°$, while it is equal to $19.00 \pm 3.66°$ by using Pinv. Statistical difference is observed between the two techniques (p = 0, T_{eq}). Notice that MVE exhibits best pose reconstruction performances also in terms of maximum errors (25.18 ° for MVE vs. 30.30 ° for Pinv). Absolute average reconstruction errors for each DoF are reported in table 4.3. MVE produces the best results which are statistically different w.r.t. Pinv algorithm, see table 4.3, except, respectively, for those DoFs which are directly measured (i.e. IM, RM and LM), for RA DoF, which exhibits a limited average estimation error ($\approx 6°$), and finally TA. For TI the smallest average estimation is observed with Pinv; a possible explanation for this might be still related to

the difficulties in kinematic modelling thumb phalanx kinematics, as previously observed. IA DoF presents the smallest absolute average estimation error with Pinv, although p-values from the comparisons between the two techniques for the estimation of this DoF are close to the significance threshold. All these observations are coherent with the discussions developed in Section 4.2.2).

Maximum DoF reconstruction errors for MVE are observed especially for those measured DoFs with potentially maximum variations in grasping tasks; this fact may be probably due to the non linearities in sensing glove elements leading to inaccurate estimation of H_g, and hence to inaccurate measures. Furthermore, MVE aims at minimizing the error statistics and some worst-case sensing results can be found.

Conclusions that can be drawn is that, except for some singular poses, best estimation performance is provided by MVE for which a good robustness to errors in measurement process modelling is also observed. However, the latter errors are not taken numerically into account in these analyses.

Moreover, as it can been seen in figure 4.7, reconstructed hand configurations obtained by MVE preserve likelihood with real poses, as opposed to pseudo-inverse based algorithm.

4.3 Optimal Design

In this section, I extend the analysis also to the optimal design of sensing gloves, i.e. to find the optimal sensor distribution, providing, for a given *a priori* information and fixed number of measurements, the optimal design in MV sense, which minimizes in average the reconstruction error and error statistics. This problem becomes particularly relevant when limits on the production costs of sensing gloves are taken into account. These cost constraints may limit both the number and the quality of sensors used and hence, an optimal distribution of sensors during the design phase is mandatory in order to obtain good performance.

It is important to notice that this optimization procedure is strictly related to the reconstruction algorithm described in Section 4.2. The pose reconstruction obtained using optimal sensor design is actually optimal only if MV reconstruction approaches previously described are used.

Optimal experimental design represents a challenging and widely discussed topic in literature [116]. Among all optimal design criteria, Bayesian methods are ideally suited to contribute to experimental design and error statistics minimization, when some information is usually available prior to experimentation (see [110, 117, 118] for a review). On the contrary, non Bayesian criteria are adopted when the the linear Gaussian hypothesis is not verified at all and when the designer's primary concern is to minimize worst-case sensing errors rather than error statistics. Criteria on explicit worst-case/deterministic bounds on the errors and tools from the theory of optimal worst-case/deterministic estimation and/or identification are discussed e.g. in [110, 119–121].

However, most of these approaches refer to cases with a number of basic sensors which is redundant or at least equal to the number of variables to be estimated. Moreover, even if they are general and easily extended to many practical applications, no one is able to take into account in its formulation the peculiar structure of human hand embodiment.

Considering sensing glove design, a more targeted method is required in order to enable for optimal device construction also when sensor elements provide insufficient and inaccurate measures. In [122] the problem of choosing the most appropriate number and locations of sensors for glove devices was proposed. The approach was based on the analysis of the DoFs of the application and their match to the DoFs of the glove. In [123] authors discussed the properties, advantages, and design aspects associated with piezoelectric materials for sensing glove design, in an application where the device was used as a keyboard. In this case, authors determined the location and hence the number of sensors by recording and analyzing typing motion of

(a) University of Pisa sensing glove.

(b) Humanglove. Image courtesy by Humanware.

Figure 4.8: Examples of gloves: on the left a continuous sensing glove with sensing elements measuring a linear combination of joint angles and on the right a discrete sensing glove whose sensors measure single-DoFs.

subjects wearing the glove. When the glove was used to control neuroprosthesis [124], the location and number of sensors was determined by classifying sensor locations based on the quality of their outputs measured in terms of reproducibility and usefulness of the force information produced during subject grasping.

Finally, [125] authors explored how to methodically select a minimal set of hand pose features from optical marker data for grasp recognition. The objective was to determine marker locations on the hand surface that was appropriate for grasp classification of hand poses.

All the aforementioned approaches rely on experimental observations: from actual sensor data, locations that provide the largest and most useful information on the system are chosen.

Here I investigate in depth the problem, obtaining the optimal distribution of sensors able to minimize in average the reconstruction error of hand poses, by using a classic Bayesian method which minimizes the *a posteriori* covariance matrix norm and hence, maximizes the information on the real hand posture available by the glove measurement.

The *a posteriori* covariance matrix, $P_p = P_o - P_o H^T (H P_o H^T + R)^{-1}$

HP_o, which depends on measurement matrix H, represents a measure of the amount of information that an observable variable carries about unknown parameters. Here I explore the role of the measurement matrix H on the estimation procedure, providing the optimal design of a sensing device able to get the maximum amount of the information on the actually measured hand posture.

I first consider the *continuous sensing* case, where individual sensing elements in the glove can be designed so as to measure a linear combination of joint angles. An example of this type is the sensorized glove developed in [113] (see figure 4.8a), or the 5DT Data Glove (5DT Inc., Irvine, CA, USA).

However, depending on the sensing technology adopted in the glove the implementation of the continuous sensing can be difficult and/or costly. For this reason, I consider also the *discrete sensing* case, where each measure available by the glove corresponds to a single joint angle. An example of this type is the Humanglove (Humanware s.r.l., Pisa, Italy) shown in figure 4.8b or the Cyberglove (CyberGlove Systems LLC, San Jose, CA, USA).

To validate the proposed techniques I considered reduced set of measurements from grasp postures in the *validation set*, as they are provided by a discrete sensing device. Of course the locations of optical markers are chosen coherently to the optimal discrete sensing device. Moreover, effects of noise are also taken into account. Experiments and statistical analyses demonstrate the improvement of the estimation techniques proposed in Section 4.2 by using the optimal design here described.

4.3.1 Problem Definition

In the ideal case of noiseless measures ($R = 0$), P_p becomes zero when H is a full rank n matrix, meaning that the available measures contain a complete information about the hand posture. In the real case of noisy measures and/or when the number of measurements m is less than the number of DoFs n, P_p can not be zero. In these cases, the

following problem becomes very interesting: find the optimal matrix H^* such that the hand posture information contained in a reduced number of measurements is maximized. Without loss of generality, let assume H to be full row rank and consider the following problem.

Problem 4.1 *Let H be an $m \times n$ full row rank matrix with $m < n$ and $V_1(P_o, H, R) : \mathbb{R}^{m \times n} \to \mathbb{R}$ be defined as $V_1(P_o, H, R) = \|P_o - P_o H^T (H P_o H^T + R)^{-1} H P_o\|_F^2$, find*

$$H^* = \arg\min_H V_1(P_o, H, R)$$

where $\|\cdot\|_F$ denotes the Frobenius norm defined as $\|A\|_F = \sqrt{tr(A\,A^T)}$, for $A \in \mathbb{R}^{n \times n}$.

Frobenius norm has been already used in literature for optimization in measurement problem, e.g. [126]. Here I adopt squared Frobenius norm to exploit its useful relation with matrix trace operator, in order to simplify the derivation of the matrix gradient flow later defined. To solve problem 4.1 means to minimize the entries of the *a posteriori* covariance matrix: the smaller the values of the elements in P_p, the greater is the predictive efficiency.

Let me introduce some useful notations. If M is a symmetric matrix with dimension n, let its Singular Value Decomposition (SVD) be $M = U_M \Sigma_M U_M^T$, where Σ_M is the diagonal matrix containing the singular values $\sigma_1(M) \geq \sigma_2(M) \geq \cdots \geq \sigma_n(M)$ of M and U_M is an orthogonal matrix whose columns $u_i(M)$ are the eigenvectors of M, known as Principal Components (PCs) of M, associated with $\sigma_i(M)$. For example, the SVD of the *a priori* covariance matrix is $P_o = U_{P_o} \Sigma_{P_o} U_{P_o}^T$, with $\sigma_i(P_o)$ and $u_i(P_o)$, $i = 1, 2, \ldots, n$, the singular values and the principal components of matrix P_o, respectively.

4.3.2 Continuous Sensing Design

In this case, each row of matrix H is a vector in $\mathbb{R}^n$ and hence can be given as a linear combination of a $\mathbb{R}^n$ basis. Without loss of generality, I can use the principal components of matrix P_o, i.e. columns

of previously defined matrix U_{P_o}, as a basis of $\mathbb{R}^n$. Consequently, naming H_c such a type of matrix related to a continuous sensing device, the measurement matrix can be written as $H_c = H_e U_{P_o}^T$, where $H_e \in \mathbb{R}^{m \times n}$ contains the coefficients of the linear combinations. Given that $P_o = U_{P_o} \Sigma_{P_o} U_{P_o}^T$, the *a posteriori* covariance matrix becomes

$$P_p = U \left[\Sigma_o - \Sigma_o H_e^T (H_e \Sigma_o H_e^T + R)^{-1} H_e \Sigma_o \right] U^T , \tag{4.19}$$

where, for simplicity of notation $\Sigma_o \equiv \Sigma_{P_o}$.

I analyze the optimal continuous sensing design both under a numerical and analytical point of view. For this purpose, let me introduce the set of $m \times n$ (with $m < n$) matrices with orthogonal rows, i.e. satisfying the condition $HH^T = I_{m \times m}$, and let denote it as $\mathcal{O}_{m \times n}$.

4.3.2.1 Numerical Solution: Gradient flows on $\mathcal{O}_{m \times n}$

A differential equation that solve problem 4.1 is proposed. The following proposition describes an algorithm that minimizes the cost function $V_1(P_o, H, R)$, providing the gradient flow which can be used to improve the method of steepest descent.

Proposition 4.1 *The gradient flow for the function* $V_1(P_o, H, R) : \mathbb{R}^{m \times n} \to \mathbb{R}$ *is given by,*

$$\dot{H} = -\nabla \|P_p\|_F^2 = 4 \left[P_p^2 P_o H^T \Sigma(H) \right]^T , \tag{4.20}$$

where $\Sigma(H) = (H P_o H^T + R)^{-1}$.

For sake of completeness, I report the calculation to obtain the gradient in the Appendix of this chapter.

Let me observe that rows of matrix H can be chosen, without loss of generality, such that $H_i P_o H_j^T = 0$, $i \neq j$ which imply that measures are uncorrelated, i.e. satisfying the condition $HH^T = I_m$. Of course, in case of noise-free sensors, this constraint is not strictly necessary. On the other hand, in case of noisy sensors, the minimum of $V_1(P_o, H, R)$ can not be obtained since it represents a limit case

that can be achieved when H becomes very large (i.e. an infimum) and hence increasing the signal-to-noise ratio in an artificial manner. Therefore, it is possible to use the constraint $HH^T = I_m$ to reduce the search space in order to find solutions.

To solve this the constrained problem it is possible to use the Rosen's gradient projection method for linear constraints [127], which is based on projecting the search direction into the subspace tangent to the constraint itself. Hence, given the steepest descent direction for the unconstrained problem, this method consists on finding the direction with the most negative directional derivative which satisfies the constraint on the structure of the matrix H, i.e. $HH^T = I_m$. This can be obtained by using the projecting matrix

$$W = I_m - H^T(HH^T)^{-1}H\,, \tag{4.21}$$

and then projecting unconstrained gradient flow (4.20) into the subspace tangent to the constraint, obtaining the search direction

$$s = W\ \nabla\|P_p\|_F^2\,. \tag{4.22}$$

Having the search direction for the constrained problem, the gradient flow is given by

$$\dot{H} = -4W\ \left[P_p^2 P_o H^T \Sigma(H)\right]^T \tag{4.23}$$

where $\Sigma(H) = (HP_oH^T + R)^{-1}$. The gradient flow (4.20) guarantees that the optimal solution H^* will satisfy $H^*(H^*)^T = I_m$, if $H(0)$ satisfies $H(0)H(0)^T = I_m$, i.e. $H \in \mathcal{O}_{m\times n}$ [5].

Notice that both $\mathcal{O}_{m\times n}$ and $V_1(P_o, H, R)$ are not convex, hence the problem could not have a unique minimum. Therefore, I can only assure that the proposed algorithm converges to a local minimum. To overcome this common problem in gradient methods, a multi-start search represents a classic procedure.

The here described gradient-based technique can be useful to characterize optimal solutions also for discrete sensing design, in case of

[5] $H(0)$ indicates the starting point at t = 0 for the gradient flow.

large dimension problem. Moreover, they can furnish interesting suggestions about a possible hybrid approach later discussed.

In case of noise-free measures, the invariance of the cost function w.r.t. changes of basis, i.e. $V_1(P_o, H, 0) = V_1(P_o, MH, 0)$ with $M \in \mathbb{R}^m$ an invertible full rank matrix, suggests that there might exist a subspace in $\mathbb{R}^n$ where the optimum is achieved. Indeed, gradients become zero when rows of matrix H are any linear combination of a subset of m principal components of the *a priori* covariance matrix. Unfortunately, this does not happen in case of noisy measures and gradients become zero only for a particular matrix H which depends also on the principal components of the noise covariance matrix.

4.3.2.2 Analytical Solutions

Here, I give a closed-form solution providing the optimal choice among all matrices in case of noise-free and noisy measures, respectively.

Noise-Free Measures. I firstly consider the case of noiseless measures, i.e. $R = 0$. Let A be a non-negative matrix of order n. It is well known (see [126]) that, for any given matrix B of rank m with $m \leq n$,

$$\min_B \|A - B\|_F^2 = \alpha_{m+1}^2 + \cdots + \alpha_n^2 \,, \tag{4.24}$$

where α_i are the eigenvalues of A, and the minimum is attained when

$$B = \alpha_1 w_1 {w_1}^T + \cdots + \alpha_m w_m {w_m}^T \,, \tag{4.25}$$

where w_i are the eigenvector of A associated with α_i. In other words, the choice of B as in (4.25) is the best fitting matrix of given rank m for A. By using this result I can determine when the minimum of (4.19), and hence of

$$\|\Sigma_o - \Sigma_o H_e^T (H_e \Sigma_o H_e^T)^{-1} H_e \Sigma_o\|_F^2 \,, \tag{4.26}$$

can be reached. Let me preliminary observe that the row vectors $(h_i)_e$ of H_e can be chosen, without loss of generality, to satisfy the condition

$(h_i)_e \, \Sigma_o \, (h_j)_e = 0, \ i \neq j$, which implies that the measures are uncorrelated. As previously said, $\mathcal{O}_{m\times n}$ denotes the set of $m \times n$ matrices, with $m < n$, whose rows satisfy the aforementioned condition, i.e. the set of matrices with orthonormal rows ($H_e H_e^T = I$). By using (4.24), the minimum of (4.26) is obtained when (see [126])

$$\begin{aligned}\Sigma_o H_e^T (H_e \Sigma_o H_e^T)^{-1} H_e \Sigma_o = \sigma_1(\Sigma_o) u_1(\Sigma_o) u_1^T(\Sigma_o) + \cdots + \\ + \sigma_m(\Sigma_o) u_m(\Sigma_o) u_m^T(\Sigma_o)\,.\end{aligned} \tag{4.27}$$

Since Σ_o is a diagonal matrix, $u_i(\Sigma_o) \equiv e_i$, where e_i is the *i-th* element of the canonical basis. Hence, it is easy to verify that (4.27) holds for $H_e = [I_m \,|\, 0_{m\times(n-m)}]$. As a consequence, row vectors $(h_i)_c$ of H_c are the first m principal components of P_o, i.e. $(h_i)_c = u_i(P_o)^T$, for $i = 1, \ldots, m$.

From these results, a principal component can be defined as a linear combination of optimally-weighted observed variables meaning that the corresponding measures can account for the maximal amount of variance in the data set. As reported in [126], every set of m optimal measures can be considered as a representation of points in the best fitting lower dimensional subspace. Thus the first measure gives the best one dimensional representation of data set, the first two measures give the best two dimensional representation, and so on.

Noisy Measures. Equation (4.25) can not be verified with noisy measures since it represents a limit case that can be achieved when H becomes very large and hence increasing the signal-to-noise ratio. To avoid this, I present an optimal solution for problem 4.1 in the set $\mathcal{A} = \left\{H \,:\, HH^T = I_m\right\}$. This problem was discussed and solved in [128], providing that, for arbitrarily noise covariance matrix R,

$$\min_{H\in\mathcal{A}} V_1(H) = \sum_{i=1}^{m} \frac{\sigma_i(P_o)}{1 + \sigma_i(P_o)/\sigma_{m-i+1}(R)} + \sum_{i=m+1}^{n} \sigma_i(P_o)\,, \tag{4.28}$$

and it is attained for

$$H = \sum_{i=1}^{m} u_{m-i+1}(R) u_i(P_o)\,. \tag{4.29}$$

Hence, if $\mathcal{A}$ consists of all matrices with mutually perpendicular, unit length rows, the first m principal components of P_o are always the optimal choice for H rows. As shown in [128] this situation changes under the more restrictive Frobenius norm constraint, i.e. $\mathcal{A} = \left\{H : \|H\|_F \leq 1\right\}$ (see [128] for details).

4.3.3 Discrete Sensing Design

Let me consider now the case that each measure y_j, $j = 1, \ldots, m$ from the glove corresponds to a single joint angle x_i, $i = 1, \ldots, n$. The problem here is to find the optimal choice of m joints or DoFs to be measured.

Measurement matrix becomes in this case a full row rank matrix where each row is a vector of the canonical basis, i.e. matrices which have exactly one nonzero entry in each row: let H_d be such a type of matrix. The optimal choice H_d^* can be easily computed, by substituting all the possible sub-sets of m vectors of the canonical basis in the cost function $V_1(P_o, H, R)$. However, a more general approach to compute the optimal matrix is provided in order to obtain the solution also when a model with a large number of DoFs is considered, and eventually extended to all human body.

Let $\mathcal{N}_{m\times n}$ denote the set of $m \times n$ element-wise non-negative matrices, then $\mathcal{P}_{m\times n} = \mathcal{O}_{m\times n} \cap \mathcal{N}_{m\times n}$, where $\mathcal{P}_{m\times n}$ is the set of $m \times n$ permutation matrices (see lemma 2.5 in [129]). This result implies that if I restrict H to be orthonormal and element-wise non-negative, I get a permutation matrix. In this work I extend this result in $\mathbb{R}^{m\times n}$, obtaining matrices which have exactly one nonzero entry in each row. Hence, the problem to solve becomes:

Problem 4.2 *Let H be a $m \times n$ matrix with $m < n$, and $V_1(P_o, H, R) : \mathbb{R}^{m \times n} \to \mathbb{R}$ be defined as $V_1(P_o, H, R) = \|P_o - P_o H^T (H P_o H^T + R)^{-1} H P_o\|_F^2$, find the optimal measurement matrix*

$$H^* = \arg\min_H V_1(P_o, H, R)$$
$$s.t. \quad H \in \mathcal{P}_{m \times n} .$$

4.3.3.1 Numerical Solution: Gradient Flows on $\mathcal{P}_{m \times n}$

A solution for this problem can be obtained defining a cost function that penalizes negative entries of H. In [129] authors defined a function $V_2(P)$ with $P \in \mathbb{R}^{n \times n}$ that forces the entries of P to be as "positive" as possible. In this chapter, I extend this function to measurement matrices $H \in \mathbb{R}^{m \times n}$ with $m < n$ and hence, I consider a function $V_2 : \mathcal{O}_{m \times n} \to \mathbb{R}$ as

$$V_2(H) = \frac{2}{3} \text{tr} \left[H^T (H - (H \circ H)) \right] , \tag{4.30}$$

where $A \circ B$ denotes the *Hadamand* or elementwise product of the matrices $A = (a_{ij})$ and $B = (b_{ij})$, i.e. $A \circ B = (a_{ij} b_{ij})$. The gradient flow of $V_2(H)$ is given by [129]

$$\dot{H} = -H \left[(H \circ H)^T H - H^T (H \circ H) \right] , \tag{4.31}$$

which minimizes $V_2(H)$ converging to a permutation matrix if $H(0) \in \mathcal{O}_{m \times n}$.

Up to this point, I have introduced two gradient flows given by (4.20) and (4.31), both on the space of orthogonal matrices, that respectively minimize their cost function, while the second one also converges to a permutation matrix. By combining these two gradient flows a solution for Problem 4.2 can be achieved. Of course, I can combine the gradient flows in two different ways: by adding them in a convex combination or firstly ignoring the non-negativity requirement and switching to the permutation gradient flow when the objective function has been sufficiently minimized [129].

Theorem 4.1 *Let $H \in \mathbb{R}^{m\times n}$ with $m < n$ the measurement process matrix and let me assume that $H(0) \in \mathcal{O}_{m\times n}$. Moreover, I suppose that $H(t)$ satisfies the following matrix differential equation,*

$$\begin{aligned}\dot{H} = 4\,(1-k)W\ \left[P_p^2 P_o H^T \Sigma(H)\right]^T + \\ + k\ H\left[(H\circ H)^T H - H^T(H\circ H)\right]\,,\end{aligned} \tag{4.32}$$

where $k \in [0,\,1]$ is a positive constant and $\Sigma(H) = (HP_oH^T + R)^{-1}$. For sufficiently large k (near one), $\lim_{t\to\infty} H(t) = H_\infty$ exists and approximates a permutation matrix that also minimizes the squared Frobenius norm of the a posteriori *covariance matrix, $\|P_p\|_F^2$.*

A proof for this theorem can be obtained directly by using results from [129].

From theorem 4.1, in order to exactly obtain a permutation matrix I should choose $k = 1$. At the same time, with this choice, I loose track of the main objective function to be minimized, i.e. $\|P_p\|_F^2$. For this reason, as in [129], I consider the following scheme in order to solve Problem 4.2:

Phase I: Starting from $H(0) \in \mathcal{O}_{m\times n}$, I apply the gradient flow (4.20) to obtain a solution H^* for Problem 4.1, which minimizes function V_1 in $\mathcal{O}_{m\times n}$.

Phase II: Starting from matrix H^* obtained in *Phase I*, I apply the gradient flow (4.32) with k near to 1, converging toward a permutation matrix.

4.3.3.2 Analytical Approach

Here, I discuss some suggestions on how to characterize the optimal permutation matrix obtained. As $\|P_p\|_F^2 \equiv \mathrm{tr}(P_pP_p^T)$, to get a solution for Problem 4.2 is equivalent to minimize

$$\begin{aligned}\mathrm{tr}[(P_o - P_o H^T (HP_oH^T + R)^{-1} HP_o)^2] = \mathrm{tr}(P_o P_o^T) + \\ - \left[2\mathrm{tr}(P_o P_o H^T (HP_oH^T + R)^{-1} HP_o) + \right. \\ \left. -\mathrm{tr}(P_o H^T (HP_oH^T + R)^{-1} HP_o P_o H^T (HP_oH^T + R)^{-1} HP_o)\right] ,\end{aligned} \tag{4.33}$$

and hence, it is the same as maximizing

$$\begin{aligned}2\mathrm{tr}(P_o P_o H^T (HP_oH^T + R)^{-1} HP_o) + \\ - \mathrm{tr}(P_o H^T (HP_oH^T + R)^{-1} HP_o P_o H^T (HP_oH^T + R)^{-1} HP_o) .\end{aligned} \tag{4.34}$$

Noise–free Measures. In case of noise–free measurements ($R = 0$), by exploiting property $\mathrm{tr}(ABC) = \mathrm{tr}(CAB)$, equation (4.34) can be rewritten as

$$2\frac{HP_oP_oP_oH^T}{HP_oH^T} - \left(\frac{HP_oP_oH^T}{HP_oH^T}\right)^2 , \tag{4.35}$$

and considering m measures,

$$2\sum_{i=1}^{m} \frac{H_i P_o P_o P_o H_i^T}{H_i P_o H_i^T} - \left(\sum_{i=1}^{m} \frac{H_i P_o P_o H_i^T}{H_i P_o H_i^T}\right)^2 . \tag{4.36}$$

As $H \in \mathcal{P}_{m\times n}$, its rows are elements of the canonical basis and hence, $H_i T H_i^T$ is the *ith* entry on the diagonal of T, i.e. T_{ii}. As a consequence, in this case, the optimal choice of matrix H depends on the entries of the *a priori* covariance matrix instead on its PCs as it happens for the continuous sensing case.

Noisy Measures. With noisy measures, noise covariance matrix R can be written in terms of its principal components and singular

values as $R = U_R \Sigma_R U_R^T$. Hence, named $H_R = U_R^T H$, equation (4.34) becomes

$$2\frac{H_R P_o P_o P_o H_R^T}{H_R P_o H_R^T + \Sigma_R} - \left(\frac{H_R P_o P_o H_R^T}{H_R P_o H_R^T + \Sigma_R}\right)^2, \tag{4.37}$$

meaning that the optimal measurement matrix H depends also on the PCs of noise covariance matrix R.

4.3.4 Hybrid Sensing Design

Up to this point, I have provided optimal solutions for continuous and discrete sensing case. However, in order to take advantage from both of them (the amount of information achievable vs low-cost implementation and feasibility) an hybrid sensing device which combines continuous and discrete sensors might represent a valid improvement, as it can be found also in biology. Indeed, human hand is an example of hybrid sensory system. In [47], among the cutaneous mechanoreceptors in the hand dorsal skin that were demonstrated to be involved in the responses to finger movements, and hence that possibly contribute to kinaesthesia, it is possible to find Fast Adapting (FA) type ones, which mainly respond to movements around one or at most two nearby joints and that can be regarded as "discrete" sensors, as well as the discharge rate of Slow Adapting (SA) afferents, which are influenced by several joints and can be regarded as "continuous" type sensors. Further investigations might use the results from this work of thesis, e.g. by suitably combining gradient flow solutions previously described to enable for an optimal hybrid solution.

4.3.5 Continuous and Discrete Sensing Optimal Distribution

As previously shown, in case of continuous sensing design the optimal choice H_c^* of the measurement matrix $H \in \mathbb{R}^{m \times n}$ is given by the first m principal components of the *a priori* covariance matrix P_o. Figure 4.9 shows the hand sensor distribution for a number $m =$

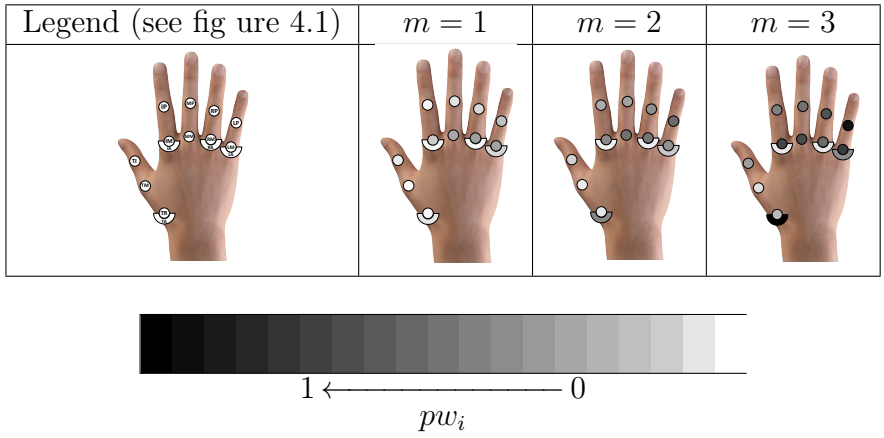

Figure 4.9: Optimal continuous sensing distribution for $m = 1$, i.e. the first PC of P_o, for $m = 2$, i.e. the first two PCs of P_o and for $m = 3$, i.e. the first three PCs of P_o. The greater is the weight pw_i of the joint angle in the optimal measures, the darker is the color of that joint. I assume the weight of the i-th joint in the optimal measures given as $pw_i = \sum_{k=1}^{m} |h_{k,i}|$, where $h_{k,i}$ is the $(k,i)^{th}$ entry of matrix H, normalized w.r.t. the maximum value of pw_i. For example, for $m = 3$, weight of LA joint is 0.53, whereas for LM joint is 0.74 and the maximum value is for TA joint.

1, 2, 3 of noise-free measures (for lack of space I omit the case of more than 3 measures). Moreover, in figure 4.10, the first three synergies are reported, with the corresponding coefficients for each joint.

In case of discrete sensing, the optimal measurement matrix H_d^*, related to a discrete sensing device, for a number of noise–free measures m ranging from 1 to 14, is reported in table 4.4. Notice that, H_d^* does not have an incremental behavior, especially in case of few measures. In other words, the set of DoFs which have to be chosen in case of m measures does not necessarily contain all the set of DoFs chosen for $m - 1$ measures.

Figures 4.11 and 4.12 show the values of the squared norm of the

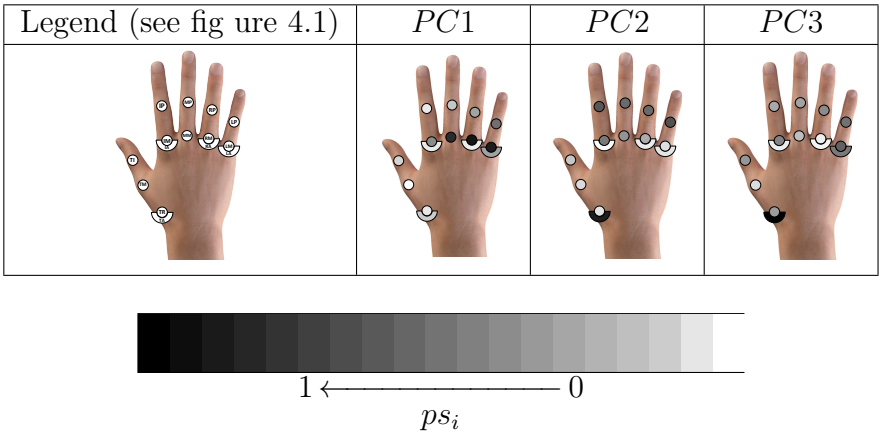

Figure 4.10: Optimal continuous sensing distribution the first PCs of P_o ($PC1$, $PC2$, $PC3$). The greater is the absolute coefficient ps_i of the joint angle in the PC, the darker is the color of that joint. I assume the coefficient of the i-th joint in the PC to be normalized w.r.t. the maximum absolute value of the coefficients achieved across $PC1$, $PC2$, $PC3$.

m	TA	TR	TM	TI	IA	IM	IP	MM	MP	RA	RM	RP	LA	LM	LP	V_1
1											X					$7.12 \cdot 10^{-2}$
2							X				X					$2.39 \cdot 10^{-2}$
3	X										X	X				$6.59 \cdot 10^{-3}$
4	X							X				X		X		$3.30 \cdot 10^{-3}$
5	X							X				X	X	X		$1.90 \cdot 10^{-3}$
6	X			X				X				X	X	X		$5.32 \cdot 10^{-4}$
7	X			X				X	X				X	X	X	$2.92 \cdot 10^{-4}$
8	X			X	X			X	X				X	X	X	$1.98 \cdot 10^{-4}$
9	X			X	X		X	X				X	X	X	X	$1.30 \cdot 10^{-4}$
10	X			X	X	X	X	X				X	X	X	X	$6.86 \cdot 10^{-5}$
11	X	X		X	X	X	X	X				X	X	X	X	$2.70 \cdot 10^{-5}$
12	X	X		X	X	X	X	X	X			X	X	X	X	$1.40 \cdot 10^{-5}$
13	X	X	X	X	X	X	X	X	X			X	X	X	X	$3.39 \cdot 10^{-6}$
14	X	X	X	X	X	X	X	X	X	X		X	X	X	X	$1.32 \cdot 10^{-6}$

Table 4.4: Optimal measured DoFs for H_d^* with increasing number of noise–free measures m (see fig ure 4.1).

a posteriori covariance matrix for increasing number m of measures. In particular, in figure 4.11 values of V_1 for matrices H_c^* and H_d^*

are reported, for both noise-free and noisy measures. In figure 4.12, values of V_1 in case of noisy measures, each affected by Gaussian zero-mean noise with standard deviation of 7°, are reported. These values are compared with the ones related to four random matrices S_i, $i = 1, \ldots, 4$, corresponding to non optimal discrete sensing devices.

Notice that, in case of noise-free measures (see figures 4.11), V_1 values decrease with the number of measures, tending to assume nearly zero values in case of both continuous and discrete sensing. This fact is trivial because increasing the measurements the uncertainty of the measured variables is reduced. When all the measured information is available, V_1 assumes zero value with perfectly accurate measures. In case of noisy measures, V_1 values decrease with the number of measures but, in this case, they tend to a value which is larger (see figures 4.11 and 4.12), depending on the level of noise.

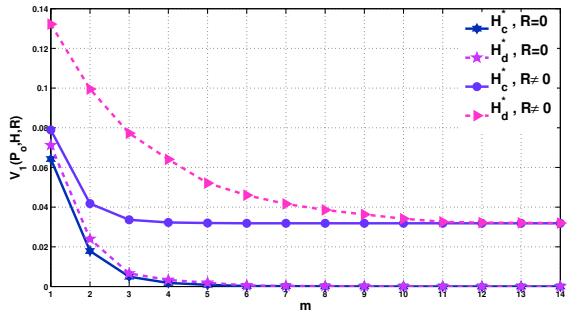

Figure 4.11: Squared Frobenius norm of the *a posteriori* matrix with noise–free and noisy measures (with standard deviation of 7°) for both H_c^* and H_d^*.

By analyzing how much V_1 reduces with the number of measurements w.r.t. the value it assumes for one measure, reduction percentage with three measured DoFs is greater than 80% for both H_c^* and H_d^*. This result suggests that with only three measurements, also in presence of noise, the optimal matrix can furnish more than 80% of uncertainty reduction. This is equivalent to say that a reduced num-

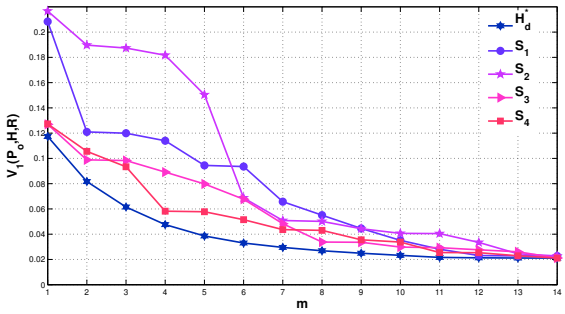

Figure 4.12: Squared Frobenius norm of the *a posteriori* matrix with noisy measures for the discrete case. The optimal measurement matrix H_d^* is compared with 4 random matrices adding the same quantity of noise (with standard deviation of 7°).

ber of measurements is sufficient to guarantee a good hand posture estimation. In [16,96], under the *controllability* point of view, authors stated that three postural synergies are crucial in grasp pre-shaping as well as in grasping force optimization since they take into account for more than 80% of variance in grasp poses. Here, the same result can be obtained in terms of measurement process, i.e. from the *observability* point of view: a reduced number of measures coinciding with the first three principal components enable for more than 80% reduction of the squared Frobenius norm of the *a posteriori* covariance matrix. The above reported result seems logic considering the duality between observability and controllability.

4.3.6 Estimation Results with Optimal Discrete Sensing Devices

In this subsection, I compare the hand posture reconstruction obtained by applying the hand pose reconstruction algorithm described in Section 4.2 to $m = 5$ measures provided by matrix H_s, also defined in Section 4.2, and by optimal matrix H_d^*. Measures were provided

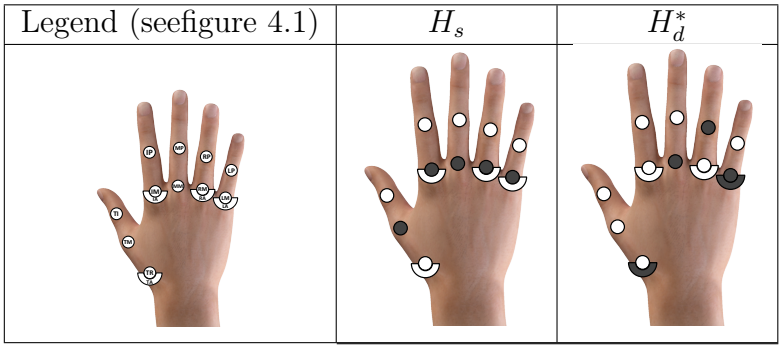

Figure 4.13: Discrete sensing distribution for matrix H_s (TM, IM, MM, RM and LM), on the left, and H_d^* (TA, MM, RP, LA and LM), on the right (see fig ure 4.1). The measured joints are highlighted in color.

by grasp data from the *validation set*, where degrees of freedom to be measured were chosen on the basis of optimization procedure outcomes, while the entire pose was recorded to produce an accurate reference posture. In figure 4.13 sensor locations related to matrix H_s and H_d^* are represented. In order to compare reconstruction performance achieved with H_s and H_d^* I use as evaluation indices the average pose estimation error and average estimation error for each estimated DoF. Maximum errors are also reported. These errors as well as statistical tools are chosen according to the ones considered in Section 4.2, where it is also possible to find a complete description of the here adopted naming. Both noise-free and noisy measures are discussed.

4.3.6.1 Noise-Free Measures

In terms of average absolute estimation pose errors ([°]), performance obtained with H_d^* is always better than the one exhibited by H_s (3.67 ± 0.93 vs. 6.69 ± 2.38). Moreover, H_d^* exhibits smaller maximum error than the one achieved with H_s (i.e. 8.25° for H_d^* vs. 13.18° for

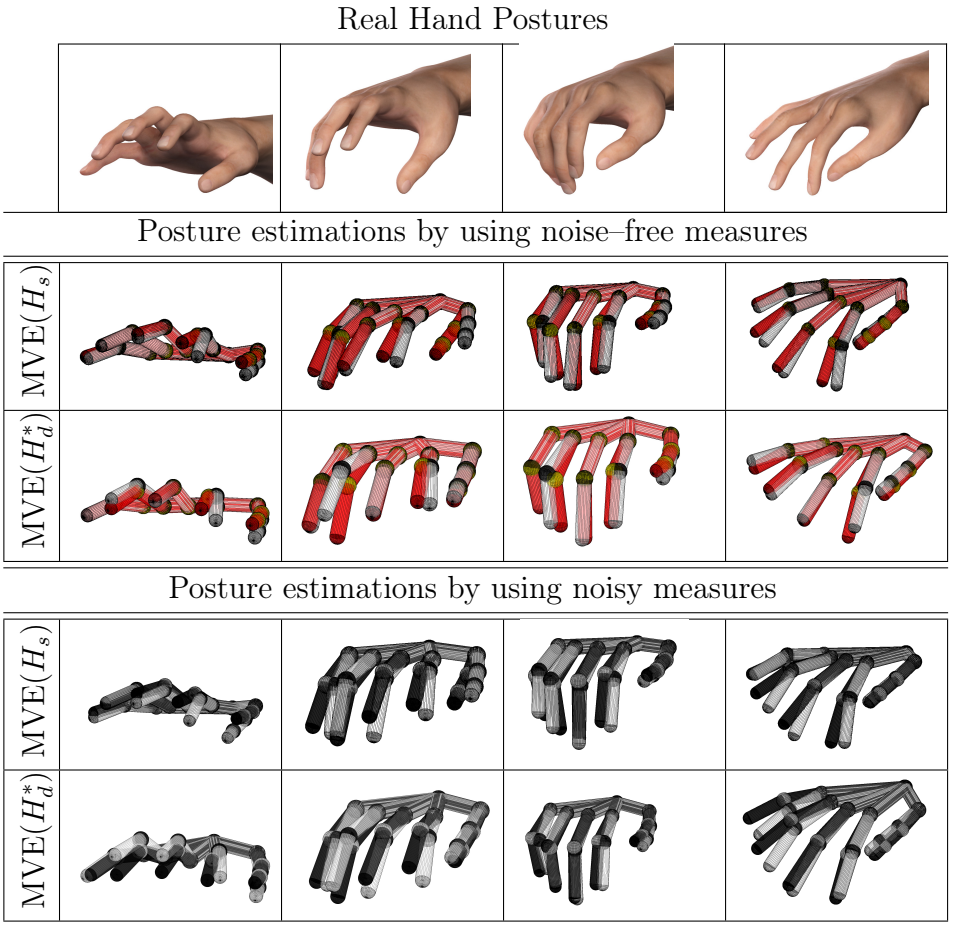

Figure 4.14: Hand pose reconstructions MVE algorithm by using matrix H_s which allows to measure TM, IM, MM, RM and LM and matrix H_d^* which allows to measure TA, MM, RP, LA and LM (see figure 4.1). In color the real hand posture whereas in white the estimated one.

H_s). Statistical differences between results from H_s and H_d^* are found ($p \simeq 0$, T_{neq}). In table 4.5 average absolute estimation errors with

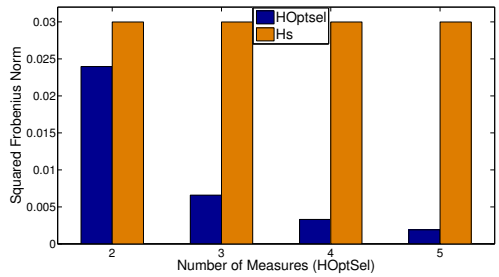

Figure 4.15: Squared Frobenius norm for the *a posteriori* covariance matrix of H_s with $m = 5$ measures, and H_d^* with $m = 2, 3, 4, 5$ measures, in case of noise-free measures.

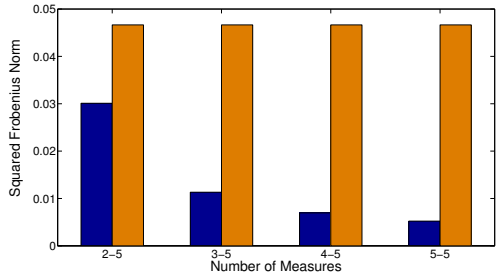

Figure 4.16: Squared Frobenius norm for the *a posteriori* covariance matrix of H_s with $m = 5$ measures, and H_d^* with $m = 2, 3, 4, 5$ measures, in case of noisy measures.

their corresponding standard deviations for each DoF are reported. For the estimated DoFs, performance with H_d^* is always better or not statistically different w.r.t. the one referred to H_s. Maximum estimation errors underline cases where H_s furnishes smaller values and vice versa, since they strictly depend on peculiar poses; however, results from the two matrices are globally comparable. In figure 4.15, squared Frobenius norm for the *a posteriori* covariance matrix of H_s with $m = 5$ measures, and H_d^* with $m = 2, 3, 4, 5$ measures, in case of noise-free measures. Notice that squared Frobenius norm is signif-

DoF	Mean Error [°]		H_s vs. H_d^*	Max Error [°]	
	H_s	H_d^*	**p-values**	H_s	H_d^*
TA⊗	10.74±8.45	0	0	31.65	0
TR	7.16±4.54	6.84±4.75	**0.72** ⋄	19.50	20.13
TM∘	0	2.17±2.21	0	0	13.04
TI	4.81±3.68	5.33±4.16	**0.64**	19.68	15.15
IA	11.96±5.33	10.55±5.65	**0.14**	26.35	26.15
IM∘	0	4.02±3.43	0	0	16.01
IP	13.26±7.06	5.42±6.44	0	27.46	43.86
MM∘⊗	0	0	–	0	0
MP	12.35±7.75	4.90±2.91	0 ‡	29.94	9.91
RA	3.45±2.43	3.82±2.94	**0.73**	9.51	12.68
RM∘	0	6.68±3.68	0	0	16.01
RP⊗	13.40±9.65	0	0	39.33	0
LA⊗	11.33±5.87	0	0	24.47	0
LM∘⊗	0	0	–	0	0
LP	11.94±9.52	6.27±3.97	0.0002	36.58	16.63

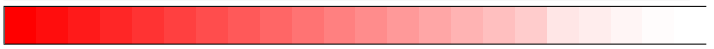

1 ←—— 0

p-values

∘ indicates a DoF measured with H_s

⊗ indicates a DoF measured with H_d^*

Table 4.5: Average estimation errors and standard deviation for each DoF [∘] for the simulated acquisition considering H_s and H_d^* both with five noise-free measures. Maximum errors are also reported as well as p-values from the evaluation of DoF estimation errors between H_s and H_d^*. ⋄ indicates T_{eq} test. ‡ indicates T_{neq} test. When no symbol appears near the tabulated values, U test is used. **Bold** value indicates no statistical difference between the two methods under analysis at 5% significance level. When the difference is significative, values are reported with a 10^{-4} precision. p-values less than 10^{-4} are considered equal to zero. Symbol "–" is used for those DoFs which are measured by both H_s and H_d^*.

icantly smaller in the optimal case, even when a reduced number of measures is considered.

4.3.6.2 Noisy Measures

In case of noise, performance in terms of average absolute estimation pose errors ([°]) obtained with H_d^* is better than the one exhibited by H_s (5.96±1.42 vs. 8.18±2.70). Moreover, maximum pose error with H_d^* is the smallest (9.30° vs. 15.35° observed with H_s). Statistical difference between results from H_s and H_d^* is found (p=0.001, T_{neq}).

In table 4.6 average absolute estimation error with standard deviations are reported for each DoF. For the estimated DoFs, performance with H_d^* is always better or not statistically different from the one referred to H_s. Maximum estimation errors with H_d^* are usually inferior to the ones obtained with H_s.

Notice that, noise randomness can slightly change which DoFs have to be measured compared with the zero noise case. In figure 4.16, squared Frobenius norm for the *a posteriori* covariance matrix of H_s with $m = 5$ measures, and H_d^* with $m = 2, 3, 4, 5$ measures, in case of noise. Also in this situation, squared Frobenius norm is significantly smaller in the optimal case, even if a reduced number of measures is considered, thus suggesting that an optimal design leading to error statistics minimization can be achieved using optimal matrix with an inferior number of measured DoFs w.r.t. H_s. Notice that in this case, squared Frobenius norm values are larger than the corresponding ones obtained in absence of noise, as it is expected.

Finally, in figure 4.14 some reconstructed poses with MVE algorithm are reported by using both H_s and H_d^* measurement matrix, with and without additional noise. Under a qualitative point of view, what is noticeable is that reconstructed poses are not far from the real ones for both measurement matrices. Moreover, it is not surprising that some poses seem to be estimated in a better manner using H_s and vice versa, even if from the previously described statistical results H_d^* provides best average performance. Indeed, MVE methods are thought to minimize error statistics rather than worst-case sensing errors related to peculiar poses [110].

DoF	Mean Error [°]		H_s vs. H_d^*	Max Error [°]	
	H_s	H_d^*	**p-values**	H_s	H_d^*
TA⊗	6.7±5.62	4.87±3.57	**0.19**	23.35	15.93
TR	7.65±5.57	7.54±5.00	**0.91** ⋄	27.46	22.73
TM∘	2.81±1.75	2.63±1.90	**0.61** ⋄	7.2	8.78
TI	6.08±4.63	5.42±4.74	**0.32**	19.6	19.10
IA	10.74±5.6	11.52±5.81	**0.32**	27.31	28.46
IM∘	4.15±3.17	6.91±5.00	0.003	11.66	21.49
IP	14.61±7.93	6.61±6.01	0	31.85	38.07
MM∘⊗	4.59±3.08	4.71±3.19	**0.77**	11.43	15.72
MP⊗	13.71±8.07	4.08±2.98	0 ‡	37.61	13.71
RA	3.12±2.37	3.28±2.45	**0.71**	9.18	9.37
RM∘	4.03±3.07	6.30±4.72	0.01 ‡	12.94	12.91
RP	16.78±11.07	6.89±3.82	0 ‡	50.66	16.34
LA	8.97±5.11	9.86±5.45	**0.38** ⋄	20.86	21.48
LM∘⊗	3.82±3.05	4.82±4.30	**0.44**	11.33	14.26
LP⊗	14.64±9.68	3.94±2.95	0	48.61	11.03

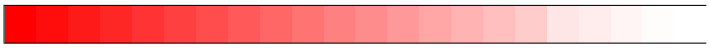

1 ←—————— 0
p-values

∘ indicates a DoF measured with H_s
⊗ indicates a DoF measured with H_d^*

Table 4.6: Average estimation errors and standard deviation for each DoF [∘] for the simulated acquisition considering H_s and H_d^* both with five noisy measures. Maximum errors are also reported as well as p-values from the evaluation of DoF estimation errors between H_s and H_d^*. ⋄ indicates T_{eq} test. ‡ indicates T_{neq} test. When no symbol appears near the tabulated values, U test is used. **Bold** value indicates no statistical difference between the two methods under analysis at 5% significance level. When the difference is significative, values are reported with a 10^{-4} precision. p-values less than 10^{-4} are considered equal to zero. Symbol "–" is used for those DoFs which are measured by both H_s and H_d^*.

4.4 Conclusions

In this chapter I have first considered reconstruction techniques to estimate static hand poses from a reduced number of measures by a given input glove-based device. These techniques are based on classic optimization and applied optimal estimation methods. The main innovation relies on the exploitation of the *a priori* information embedded in the covariance structure of a set of grasps. This covariance individuates some coordination patterns, defined as *postural synergies*, which reduce hand DoFs to be measured and controlled. Simulation results, where noise effects are also considered, and experiments with a low-cost sensing glove are reported. Performance is compared with the one obtained with a simple pseudo-inverse based algorithm. Statistical analyses demonstrate the effectiveness of the here analyzed hand pose reconstructions.

Afterwards, I have proposed an optimal design of sensing glove on the basis of the minimization of the *a posteriori* covariance matrix. Optimal solution are described for both continuous and discrete sensing and preliminary suggestions are given also for the hybrid case. In the continuous sensing case, optimal measures are individuated by principal components of the *a priori* covariance matrix, thus suggesting the importance of postural synergies not only for hand control. The reconstruction performance obtained by combining the aforementioned estimation technique and optimal designed measures is significantly improved if compared with non optimal measure case. Therefore, I have provided a complete procedure to enhance the performance as well as the design of both sensorization systems for robotic hands and active touch sensing systems, which can be used in a wide range of applications, ranging from virtual reality to tele-robotics and rehabilitation. By optimizing the number and location of sensors the cost of production can be further reduced without loss of effectiveness, thus increasing device diffusion.

4.5 Appendix

This appendix is devoted to the derivation of the gradient equation given in theorem 4.1. In this regard, let me remark that the Frobenius norm of a matrix $A \in \mathbb{R}^{n\times n}$ is given as

$$\|A\|_F = \sqrt{\mathrm{tr}(A^T A)} = \sqrt{\sum_{i=1}^{n} \sigma_i^2}\,, \tag{4.38}$$

and hence,

$$\|P_o - P_o H^T (H P_o H^T + R)^{-1} H P_o\|_F^2 = \mathrm{tr}(P_p^T P_p) \tag{4.39}$$

where $P_p = P_o - P_o H^T (H P_o H^T + R)^{-1} H P_o$. To find the gradient flow, I need to compute

$$\begin{aligned}\frac{\partial \mathrm{tr}(P_p^T P_p)}{\partial H} &= \mathrm{tr}\left(\frac{\partial (P_p^T P_p)}{\partial H}\right) = \mathrm{tr}\left(\frac{\partial P_p^T}{\partial H} P_p + P_p^T \frac{\partial P_p}{\partial H}\right) = \\ &= \mathrm{tr}\left(\frac{\partial P_p^T}{\partial H} P_p\right) + \mathrm{tr}\left(P_p^T \frac{\partial P_p}{\partial H}\right) = 2\mathrm{tr}\left(P_p^T \frac{\partial P_p}{\partial H}\right)\,,\end{aligned} \tag{4.40}$$

as $\partial(\mathbf{XY}) = (\partial \mathbf{X})\mathbf{Y} + \mathbf{X}(\partial \mathbf{Y})$ and $\mathrm{tr}(A^T) = \mathrm{tr}(A)$. Moreover, from differentiation rules of expressions w.r.t. a matrix $\mathbf{X}$, I get $\partial \mathbf{X}^{-1} = -\mathbf{X}^{-1}(\partial \mathbf{X})\mathbf{X}^{-1}$ and hence, assuming $\Sigma(H) = (H P_o H^T + R)^{-1}$, it is obtained

$$\begin{aligned}\frac{\partial P_p}{\partial \mathbf{H}} &= -P_o \left[(\partial H)^T \Sigma(H) H + H^T \left(\frac{\partial \Sigma(H)}{\partial H} H + \Sigma(H)\, \partial H\right)\right] P_o = \\ &= -P_o \left[(\partial H)^T \Sigma(H) H - H^T \left(\Sigma(H) \left(\partial H P_o H^T + \right.\right.\right. \\ &\quad \left.\left.\left. + H P_o (\partial H)^T\right) \Sigma(H) H + \Sigma(H)\, \partial H\right)\right] P_o\,.\end{aligned} \tag{4.41}$$

Substituting (4.41) in (4.40) and by using a well note trace property ($\mathrm{tr}(A+B) = \mathrm{tr}(A) + \mathrm{tr}(B)$) it is achieved

$$\begin{aligned}\frac{\partial \mathrm{tr}(P_p^T P_p)}{\partial H} &= 2\left[-\mathrm{tr}(P_p^T P_o (\partial H)^T \Sigma(H) H P_o) + \right. \\ &\quad + \mathrm{tr}(P_p^T P_o H^T \Sigma(H) \partial H P_o H^T \Sigma(H) H P_o) + \\ &\quad + \mathrm{tr}(P_p^T P_o H^T \Sigma(H) H P_o (\partial H)^T \Sigma(H) H P_o) - \\ &\quad \left. - \mathrm{tr}(P_p^T P_o H^T \Sigma(H) \partial H P_o)\right]\,.\end{aligned} \tag{4.42}$$

Since $\mathrm{tr}(AB) = \mathrm{tr}(BA)$

$$\begin{aligned}\frac{\partial \mathrm{tr}(P_p^T P_p)}{\partial H} &= 2\left[-\mathrm{tr}((\partial H)^T \Sigma(H) H P_o P_p^T P_o) + \right. \\ &+ \mathrm{tr}(P_o H^T \Sigma(H) H P_o P_p^T P_o H^T \Sigma(H) \partial H) + \\ &+ \mathrm{tr}((\partial H)^T \Sigma(H) H P_o P_p^T P_o H^T \Sigma(H) H P_o) - \\ &\left. - \mathrm{tr}(P_o P_p^T P_o H^T \Sigma(H) \partial H)\right] \end{aligned} \tag{4.43}$$

and as $\mathrm{tr}(A^T) = \mathrm{tr}(A)$

$$\begin{aligned}\frac{\partial \mathrm{tr}(P_p^T P_p)}{\partial H} &= 2\left[-\mathrm{tr}(P_o^T P_p P_o^T H^T \Sigma(H)^T \partial H) + \right. \\ &+ \mathrm{tr}(P_o H^T \Sigma(H) H P_o P_p^T P_o H^T \Sigma(H) \partial H) + \\ &+ \mathrm{tr}(P_o^T H^T \Sigma(H)^T H P_o^T P_p P_o^T H^T \Sigma(H)^T \partial H) - \\ &\left. - \mathrm{tr}(P_o P_p^T P_o H^T \Sigma(H) \partial H)\right] , \end{aligned} \tag{4.44}$$

whence, finally

$$\begin{aligned}\frac{\partial \mathrm{tr}(P_p^T P_p)}{\partial H} &= 2\left[-P_o^T P_p P_o^T H^T \Sigma(H)^T + \right. \\ &+ P_o H^T \Sigma(H) H P_o P_p^T P_o H^T \Sigma(H) + \\ &+ P_o^T H^T \Sigma(H)^T H P_o^T P_p P_o^T H^T \Sigma(H)^T - \\ &\left. - P_o P_p^T P_o H^T \Sigma(H)\right] = \\ &= 2\left[(P_o H^T \Sigma(H) H - I) P_o P_p^T P_o H^T \Sigma(H) + \right. \\ &\left. + (P_o^T H^T \Sigma(H)^T H - I) P_o^T P_p P_o^T H^T \Sigma(H)^T\right] . \end{aligned} \tag{4.45}$$

Matrices P_p, P_o and $\Sigma(H)$ are symmetric, and hence, for this particular case I can write

$$\frac{\partial \mathrm{tr}(P_p^T P_p)}{\partial H} = -4\left[P_p^2 P_o H^T \Sigma(H)\right]^T , \tag{4.46}$$

with $\Sigma(H) = (H P_o H^T + R)^{-1}$. Equation (4.46), apart from the sign, represents the gradient flow defined in theorem 4.1.

Part III

Integration of Cutaneous and Kinaesthetic Cues for Softness Rendering

Chapter 5

Integration of Cutaneous and Kinaesthetic Cues in a Haptic Device for Softness Rendering.

In Chapter 2 I have described how cutaneous information, which is predominant in softness discrimination, can be harnessed using suitable reductions, which have enabled for the design of more effective tactile displays. However, perception and precise discrimination of softness depend on both cutaneous and kinaesthetic information: psychophysical experiments leading to this conclusion have been reported in the literature [37].

In this chapter I venture to speculate about kinaesthesia and cutaneous sensing as the two main synergies of the *haptic synergies basis*, which completely describe the mechanics of touch and its perception [22]. Furthermore, as for motor task accomplishment, the more complex the task the larger the number of motor synergies to be employed, the quality of perception and the fidelity by which softness can be artificially rendered should increase with the number of *perceptual synergies* enrolled in rendering. However, nowadays relatively little work has been done on the realization of haptic devices replicating

the two the two main haptic synergies in an integrated and effective manner and the technology of haptic devices is still unsatisfactory as far as softness rendering is concerned.

Although purely kinaesthetic devices, such as e.g. the PHANToM by Sensable (Wilmington, MA- USA) or the Delta Haptic Device (DHD) by Force Dimension (Nyon, Switzerland) have achieved outstanding results in displaying hardness within their impedance range (or Z-width), the impossibility to provide cutaneous cues severely limits their capabilities. On the other hand, although recent advancements in cutaneous displays [130–132] have provided promising results, a technical difficulty remains to achieve sufficient resolution of the stimuli so as to convey a convincing softness information. Devices specifically intended to display softness properties have been proposed in the literature (see e.g. [30, 133, 134, A1]), which are based on surrogating detailed contact shape information with information on the contact area on the fingertip and its changes with varying contact force. These displays have proved able to evoke a reliable softness sensation, enabling better discrimination than a similar, but purely kinaesthetic display [30,A1] for objects in a given class. The main limitations of this display are its limited workspace and softness range. Moreover, the device is unable to decouple the rendering of cutaneous and kinaesthetic information.

To fully exploit the integrated nature of human tactile perception and correspondingly enlarge the class of objects that can be discriminated, in this thesis I propose a combination of kinaesthetic and contact area displays [A7,A8], so as to achieve independent and accurate rendering of both kinaesthetic and cutaneous cues. To motivate the need for integrated displays, I consider a simplified example involving the mechanics of contact between elastic bodies, illustrating unimodally ambiguous objects, i.e. objects that provide equal kinaesthetic but different cutaneous cues, or the other way around. I then describe an integrated display and the control technique to achieve independent control of the kinaesthetic and cutaneous information. To assess the performance of the integrated display, I conducted psy-

chophysical experiments and compared the subjective perception of softness with that obtained by direct touch on physical objects. Results show that the subjects interacting with the integrated haptic display are able to discriminate softness better than with either a purely kinaesthetic or a purely cutaneous display. This conclusion can be easily interpreted in a geometrical-sense; i.e. the fidelity by which softness can be artificially rendered increases with the number of haptic synergies employed for rendering.

5.1 Motivation: Ambiguities in Unimodal Touch

The complex mechanical interaction which occurs when a finger pad touches an object generates a wide range of stimuli for skin receptors and proprioceptive system. In previous chapters, I have introduced some useful lower-dimensional projections of this perceptual manifold, which can be interpreted in a geometrical manner as a synergy basis of the sensory space, whose elements are able to simplify the haptic sensing redundancy with an accuracy related to the level of basis truncation.

To briefly summarize the aforementioned findings, given that sensing resultant forces and kinematic motions are primary objects of kinaesthesia, the P/δ curve of a fingertip/object pair can be considered as a close correlate of kinaesthetic information elicited by probing for softness. For cutaneous information manifold, an high-level projection can obtained e.g. by means of Contact Area Spread Rate paradigm (CASR) [30], which expresses the relation between the contact force P and the measure of the region of contact, or contact area A. Therefore, the P/A curve of a fingertip/object pair can be regarded as a correlate of cutaneous information elicited by probing for softness. It is important to preliminary observe that there may exist quite distinct objects which, probed for softness, provide identical kinaesthetic information but different cutaneous information; and that

the opposite also applies. Indeed, consider objects having a 2-layered structure, for which both layers are flat and have similar thickness, but different Young's moduli $E_1 > E_2$. Two objects, each consisting of the superposition of the two layers, but probed from opposite sides, would exhibit the same P/δ, but different P/A (see figure 5.1). The

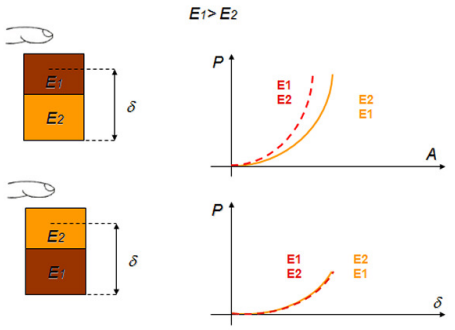

Figure 5.1: An object comprised of two layers of different materials is probed for softness from the two sides. The resultant force-displacement (P/δ) curve is equal, while the force-area (P/A) curve is steeper when the stiffer layer is above.

opposite case of two objects offering similar P/A, but different P/δ curves, can also be conceived. Consider three materials for which the Young's moduli are $E_1 >> E_2 > E_3$, and arrange them in two similar 2-layered objects as in (see 5.2).

A somewhat more detailed illustration of possible unimodal haptic ambiguities can be easily given in terms of the classical Hertzian model of contact. Although this is a very rough model of fingertip contact, it does provide insight in the problem and will inspire and motivate actual psychophysical discrimination experiments. More refined models are available in the biomechanics and haptics literature, e.g. the modified Hertzian model of [135, 136] or liquid-filled membrane model of [137]. However, these models have only been validated for fingertip contact with rigid objects and neglect the effect of the

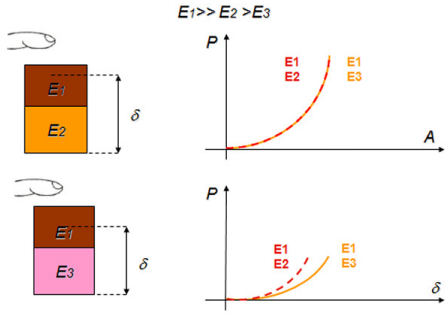

Figure 5.2: Two objects producing similar force-area, but different force-displacement curves.

compliance of the surface of the probed object, which is a crucial aspect of my analysis. Consider the simple contact between two elastic bodies, pressed against each other by force P. Assume the two bodies are locally spherical at the contact, with radii R_1 and R_2, respectively. Let the Young's modulus and Poisson ratio for the material of the two spheres be E_1, ν_1, resp. E_2, ν_2. In Chapter 2, using elementary Hertz contact theory [59, 60], I have described equation (2.10), which expresses contact area under a given loading condition.

By defining E

$$E = \left(\frac{1 - \nu_1^2}{E_1} + \frac{1 - \nu_2^2}{E_2} \right)^{-1} \tag{5.1}$$

equation (2.10) can be rearranged to obtain a simple relationships between force P and contact area $A = \pi a^2$ as

$$P(A) = \frac{4}{3} \frac{E}{R} \left(\frac{A}{\pi} \right)^{\frac{3}{2}}. \tag{5.2}$$

Moreover, a relation between force P and total displacement δ is also achieved as

$$P(\delta) = \frac{4}{3} E \sqrt{R \delta^3} \tag{5.3}$$

These relationships can be used to compare the force-displacement (P/δ) and force-area (P/A) curves obtained for the contact of different pairs of spherical objects. Consider two contact pairs formed by an idealized (linear elastic spherical) fingertip and two objects O_1, O_2. Let the fingertip be characterized by constants R_f, E_f, and ν_f. Experimental *in vivo* characterization of the skin in various parts of the body reported in [60] provides values in the range from $0.7 \cdot 10^4 \mathrm{N/m}^2$ to $3.3 \cdot 10^4 \mathrm{N/m}^2$ for the Young's modulus (parameters in [60] were obtained by applying the Hertzian model of contact to experimental data from skin indentation with spherical objects), whereas a generally accepted value for the Poisson ratio for the skin is 0.5. I assume $R_f = 15$ mm. Let R_i, E_i, $i = 1, 2$ denote the Young's modulus and radius of the two objects, and R_{fi}, E_{fi} the relative radius and equivalent modulus, respectively. From simple calculations, and assuming for simplicity identical Poisson ratio for objects and fingers, it follows that an object O_2 would provide the same kinaesthetic (P/δ) information as an object O_1 if its geometric and elastic parameters satisfy the relation

$$\frac{1}{R_2} = \frac{1}{E_2}\left(\frac{E_{f1}}{R_{f1}}\right) + \left(\frac{\tilde{E}_1}{R_1} - \frac{1-\tilde{E}_1}{R_f}\right) \tag{5.4}$$

where $\tilde{E}_i = \frac{E_i}{E_i + E_f}$. On the other hand, if

$$\tilde{R}_2 = \frac{\tilde{E}_1^2}{\tilde{E}_2^2}\tilde{R}_1, \tag{5.5}$$

with $\tilde{R}_i = \frac{R_i}{R_i + R_f}$, then the finger would observe the same cutaneous P/A information. From these observations, it follows that if either information is used alone, than there exist simple objects for which their different radii and moduli make them indistinguishable (see figure 5.3). As a consequence of these results, it is expected that there exist objects whose softness can only be distinguished if the number of employed elements from the sensory synergy basis increases (i.e.

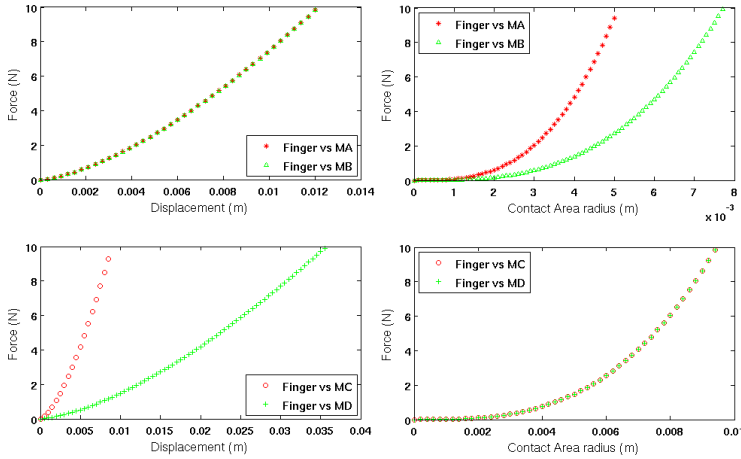

Figure 5.3: Comparison of the force-displacement (left column) and force-area (right column) curves for finger-object contacts. In the first row, two objects M_A and M_B have parameters $E_A = 10^6$ N/m^2, $R_A = 2.5$ mm, $E_B = 1.5{\cdot}10^5$ N/m^2, $R_B = 7.3$ mm, which satisfy relation 5.4. In the second row, two objects M_C and M_D have parameters $E_C = 2{\cdot}10^5$ N/m^2, $R_C = 30$ mm, $E_D = 2{\cdot}10^4$ N/m^2, $R_D = 3$ mm, satisfying relation 5.5.

only when both kinaesthetic and cutaneous cues are available), and that, in general, tactual discrimination of softness can be improved by an integrated device.

5.2 The Integrated Haptic System

The integrated kinaesthetic/cutaneous haptic system is comprised of a softness display combined in series with a commercial haptic interface, the Delta Haptic Device (DHD) (see figure 5.9). For the softness display, I consider the discrete-CASR type device [30], as it has been described in Chapter 2. In order to enable for a better comprehension of the control equations and strategy, in figure 5.4 the geometry and

the appearance of the display are reported. To smooth the change of distribution of pressure against the finger pad, the cylinders were covered with a latex sleeve. In this way any edge effect was reduced. As already said, this softness display can replicate a desired force/area behaviour with good accuracy but when used as a stand alone device, it does not allow to implement arbitrary force-area and force-displacement curves independently. This is true also for the fabric yielding display previously introduced [A1]. The relation between the resultant force P and contact area A in the softness display can be obtained (neglecting losses in the system) by equating the work done by the external force and pressures as

$$P\Delta\delta = -p\Delta V \Rightarrow P = -p\frac{dV}{d\delta}. \tag{5.6}$$

The volume of the inner chamber can be computed geometrically as

$$V = \pi\frac{R^2H}{3} - \pi\frac{\delta^3R^2}{3H^2}, \tag{5.7}$$

in which H is the cone height, and R is the external radius at the basis ($H = 10$ mm and $R = 6.5$ mm for the prototype at hand). Hence it can be obtained

$$P = p\pi\frac{\delta^2R^2}{H^2} = pA. \tag{5.8}$$

It should be noted here that the tip displacement δ corresponds to the overall contact displacement, if the softness display is used alone. Hence, to any given P/A, the display associates a unique P/δ profile. This can be changed by coupling the softness display with a purely kinaesthetic display, such as the DHD. The analytical model of the softness display were experimentally assessed following the characterization procedure described in Section 2.4.4.

5.2.1 Control of the Integrated Display

In the integrated device, the softness display is connected in series with the DHD. If the axial displacement of the former under load is

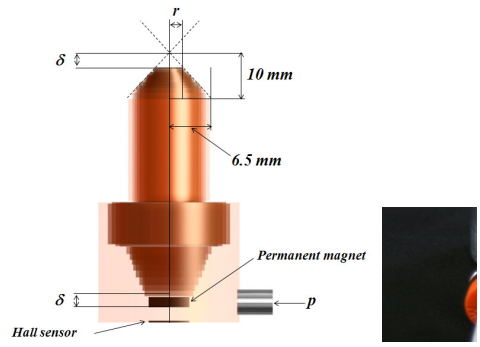

Figure 5.4: Geometry (left) and appearance (right) of the softness display. The prototype has a max. height of 33 mm and a diameter of 13 mm.

denoted by δ_s, and δ_d is that of the DHD, the overall displacement felt by the probing finger is

$$\delta = \delta_s + \delta_d. \tag{5.9}$$

To replicate two arbitrary kinaesthetic and cutaneous curves of a given object marked with the subscript m, as given e.g. by

$$\begin{cases} P = \alpha_m(A_m) \\ P = \beta_m(\delta_m) \end{cases} \tag{5.10}$$

the integrated device offers two independent control inputs, the chamber pressure p and the DHD force P_d. I choose to control the softness display pressure so as to match the force-area curve, i.e. by imposing $A = A_m$ in(5.8) and regulate the air pressure as

$$p = \frac{\alpha_m(A)}{A}. \tag{5.11}$$

According to the softness display model, a displacement is correspondingly obtained as

$$\delta_s = \frac{H}{R}\sqrt{\frac{A}{\pi}} \tag{5.12}$$

The DHD displacement δ_d is therefore controlled so as to obtain $\delta = \delta_s + \delta_d = \delta_m$. The desired δ_m can be obtained by inversion of the given curve (it is assumed here that the inverse exists, which in practical cases is guaranteed by the monotonicity of the curve), i.e. $\delta_m = \beta_m^{-1}(P)$. Hence,

$$\delta_d = \beta_m^{-1}(P) - \frac{H}{R}\sqrt{\frac{P}{p\pi}} \tag{5.13}$$

This value of δ_d is actually used as a reference for a PID control loop for the DHD device, which is fast and stiff enough as to guarantee negligible errors in tracking. The effectiveness of this control scheme for the integrated display was experimentally verified by tracking the characteristic curves of different materials. Typical results are reported in figure 5.5, showing good tracking performance for a spherical foam object of radius $R = 11\,\text{mm}$ for which the characteristic curves had been experimentally obtained [138] as

$$\begin{aligned} P &= 42\delta_m + 0.64 && \text{[N]} \\ P &= 1.4A_m^2 + 0.33A_m + 0.554 && \text{[N]} \end{aligned} \tag{5.14}$$

To assess the actual quality of the integrated display as a haptic display, however, it is necessary to evaluate how good the haptic rendering of softness is for human subjects interacting with the interface. In the next sections, I describe a series of psychophysical experiments and compare the subjective perception of softness rendered by the display, with that obtained by direct touch of real objects.

5.3 Materials and methods

5.3.1 Subjects

After written consensus, 15 healthy volunteers participated in the study. Their age ranged from 23 to 30. None had a history of nerve injury or finger trauma and their finger pads were free of calluses.

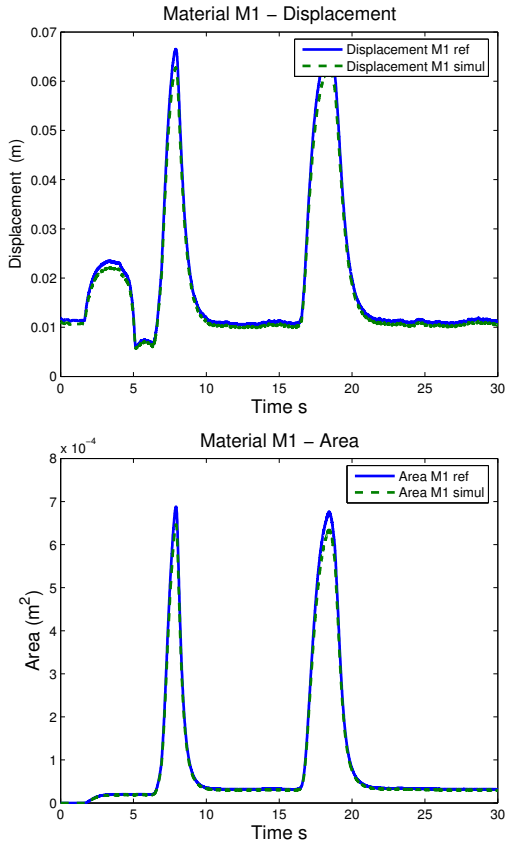

Figure 5.5: Experimental results obtained with the integrated display with the independent control of force-displacement (above) and force-area (below) characteristics. Continuous lines represent the response of the reference object to an externally applied force, while dashed lines describe the display outputs.

5 volunteers participated only in the experiments with silicone specimens; 5 volunteers participated only in the experiments with the haptic display; 5 volunteers participated in both the experiments. Their handedness was evaluated by the Edinburgh Handedness In-

ventory (EHI) [66] and they were allowed to use the dominant hand to perform the task. They always performed the tests comfortably sat, blindfolded and with plugged up ears, to prevent the possible use of any other sensory cues and eliminate any diversion from the task. The chosen arm was locked to the table and the subject was able to move the wrist and fingers only.

5.3.2 Physical Specimens

A set of silicone cylinders was used through one experimental session. Cylinders were made of material obtained by mixing a given quantity of a commercial bi-component, room temperature–curing silicone (BJB TC-5005A/B), with a variable percentage of plasticizer (BJB TC-5005C), acting as a softener. These components are produced by BJB Enterprises Inc.(Tustin,California-USA). Varying the amount of softener in the mixture from 0% to 45%, the Young's modulus decreases as shown in figure 5.6. Each cylinder is 0.7 cm tall with a radius of 1.85 cm. A set of rigid cylinders having the same radius and height as the previous ones, made of polymethyl methacrylate, was also used. By suitably combining these cylinders, three classes of specimens were realized, which are described as follows.

CL1) Five specimens consisting of two silicone cylinders realized with the same amount of softener, stacked along their axial direction. The used softener percentages were $0\%, 10\%, 20\%, 35\%, 45\%$, respectively;

CL2) Five specimens consisting of a rigid cylinder placed on the top of a silicone cylinder with the same percentages of softener as in class 1.

CL3) Five specimens consisting of two silicone cylinders stacked along their axial direction. The softener percentages of each pair were $(0\%-45\%)$, $(10\%-35\%)$, $(20\%-20\%)$, $(35\%-10\%)$, $(45\%-0\%)$.

The second softener percentage of each pair refers to the silicone cylinder placed at the bottom of the stacks. These combinations were carefully chosen to have the same overall force-displacement characteristic.

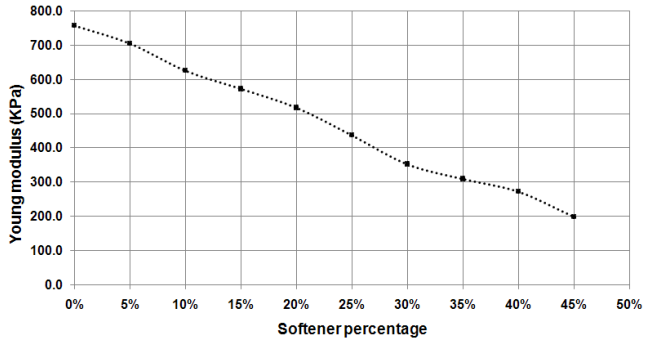

Figure 5.6: Relationship between the percentage of softener used in the silicone samples and the Young modulus produced. Measurements used the instrumented indenter used to characterize the "discrete CASR display" as described in Section 2.4.6.

5.3.3 Rendered Specimens

Artificial softness specimens were used through the second experimental session, rendering different force-displacement and force-area curves through the haptic display described in previous sections. The display was controlled in three different modes:

CM1) the integrated display control method of Section 5.2.1 is used so as to mimic both the P/A and P/δ curves of physical specimens in class CL1;

CM2) the kinaesthetic display (DHD) is controlled to mimic the P/δ curve of specimens in class CL2, while the softness display is replaced by a rigid surface;

CM3) the softness display is controlled to mimic the P/A curve of specimens in class CL3, while the DHD display is used only to compensate for the displacement introduced by the softness display (i.e., to have $\delta_d = -\delta_s$ in (5.9)).

5.3.4 Design and Procedure

Experiments were designed to test the ability of subjects to tactually discriminate softness both in normal conditions and through a haptic interface. The first group of experiments, which hereinafter will be refer to as "direct touch", involved touching physical specimens as described above. The second group, or "rendered touch", involved interaction with artificial specimens rendered through the control of the haptic display. Both groups of experiments included pairwise discrimination and ranking tasks. Each group of experiments was performed in three different configurations, which were designed to approach three ideal conditions:

I) integrated (kinaesthetic and cutaneous) tactile information is available to the subject;

K) subjects can rely only on kinaesthetic information to discriminate the specimens, i.e. cutaneous information is kept unchanged through the experiments;

C) subjects can rely only on cutaneous information to discriminate the specimens, i.e. kinaesthetic information is kept unchanged through the experiments;.

In all tests, subjects had no time limitations and were allowed to check each specimen or haptic stimulus as many times as they wished going back and forth between them at will.

The experiments described in this work should be compared with the experiments reported in [37] and described in Chapter 2, which were also used to investigate the role and relative weight of cutaneous and kinaesthetic cues in haptics. Firstly, in [37] no actively

controlled haptic interfaces are involved in experiments. Here, "direct touch" experiments also differ substantially from those in [37]. Indeed, anaesthesia is not used to suppress cutaneous cues, rather I constructed suitable specimens which equalize the cue itself. Symmetrically, by constructing other specimens which equalize the kinaesthetic cue, I avoided the use of "passive" exploration procedures used in [37], whereby the fingertip was rigidly fixed to the tabletop, and specimens were pressed against it. Overall, these techniques are less invasive and allow comparison of human exploration of physical and rendered objects.

5.3.5 Experiments on Direct touch

Ten subjects participating in this experiment were presented with physical specimens and were asked to judge their softness by touch. They were instructed to do so by pressing vertically or tapping the index or middle finger of their dominant hand against the specimen. Subjects were recommended not to perform movements of the finger across the surface and not to apply lateral forces (see figure 5.7). In this way, according to the literature [54], any anisotropic effect or distortion in softness perception due to the radial/tangential discrepancy in touch is eliminated, only focusing on normal indentation of the specimens. Experiments in the integrated condition (I) used specimens in class CL1. Specimens in class CL2 provided for the kinaesthetic-only conditions of experiments (K). Indeed, as described above (see figure 5.2), these specimens are expected to produce very similar cutaneous cues. Finally, specimens in class CL3 were used for the cutaneous-only experimental conditions (C) (see figure 5.1).

5.3.5.1 Pairwise discrimination

For each condition (I, K, C), five specimens (denoted by $SS1$ to $SS5$) in the relative class were used (see figure 5.8).

In each trial, a standard ($SS3$) and a comparison specimen were

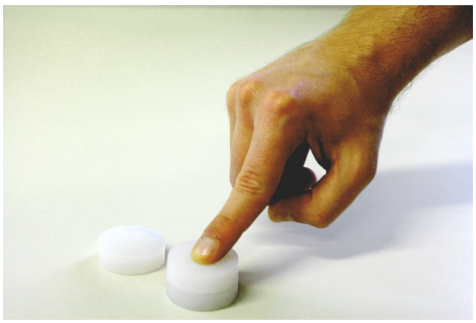

Figure 5.7: A subject's hand palpating one of the silicone specimens used in the tests.

presented to the subjects in random order. After probing the specimens, subjects were asked to report which of the two was softer. Each task was performed three times for each condition (I, K, C).

5.3.5.2 Ranking

In the ranking experiment subjects were asked to probe and sort in terms of softness the set of 5 specimens $SS1$ to $SS5$, presented in random order. The specimens in the ranking experiments, for the three different conditions, are as described above (figure 5.8). Ranking tasks were repeated three times for every condition (I, K, C).

5.3.6 Experiments on Rendered Touch

Ten subjects were presented with the integrated haptic display, controlled as to render the softness of different materials, and were asked to judge softness by touch. Subjects were allowed probing and tapping in the vertical direction (corresponding to the axis of the haptic display) and were instructed to avoid exerting lateral forces. A picture of a subject's hand performing the test is shown in figure 5.9.

	Class CL1 (I)	Class CL2 (K)	Class CL3 (C)
SS1	0 % 0 %	Rigid disk 0 %	0 % 45 %
SS2	10 % 10 %	Rigid disk 10 %	10 % 35 %
SS3	20 % 20 %	Rigid disk 20 %	20 % 20 %
SS4	35 % 35 %	Rigid disk 35 %	35 % 10 %
SS5	45 % 45 %	Rigid disk 45 %	45 % 0 %

Figure 5.8: Naming convention for specimens in different experiments

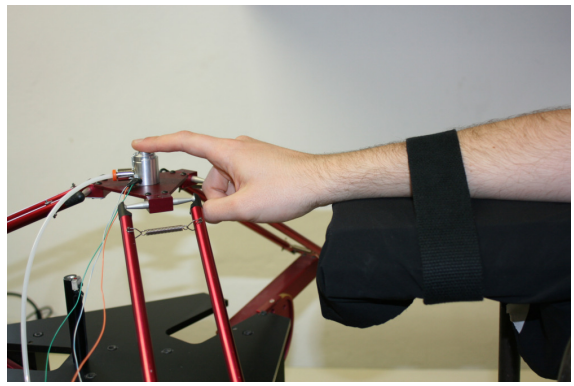

Figure 5.9: A subject interacting with the integrated haptic display used in the experiments.

5.3.6.1 Pairwise discrimination

In pairwise discrimination tests, five specimens, denoted as $SH1$-$SH5$ with $SH3$ as reference, were produced on the haptic system. In the integrated condition (I), specimens were rendered using the control

mode CM1; the control mode CM2 was used for condition (K), and mode CM3 for condition (C).

5.3.6.2 Ranking

The same set of five stimuli use in the pairwise discrimination experiment was employed in the ranking experiment. Subjects were presented with new stimuli in less than a second. Subjects were asked to rank these specimens in the three conditions (I, K, C).

5.4 Experimental Results and Discussion

5.4.1 Pairwise Discrimination with Physical Specimens

Results of pairwise discrimination experiments on silicone specimens are reported in figure 5.10. Answers are classified as $X = 1$ if the subject correctly identifies the softer specimen, or $X = 0$ otherwise. The average number of correct answers m_n is represented by the height of the histogram bars in figure 5.10. The statistics of this binary experiment are described by its Bernoulli distribution. Confidence intervals for expected values $E(X)$ with statistical significance $(1-\alpha)$ are also reported in figure 5.10. The intervals are computed as

$$E(X) \in \left[m_n - z_{\frac{\alpha}{2}} \sqrt{\frac{m_n(1-m_n)}{N}}, m_n + z_{\frac{\alpha}{2}} \sqrt{\frac{m_n(1-m_n)}{N}} \right] \quad (5.15)$$

with $\alpha = 5\%$, sample size $N = 30$, and critical value of the normalized standard distribution $z_{\frac{\alpha}{2}} = 1.96$ (from standard statistical tables).

It is worthwhile noting that when subjects can rely on their full tactual ability of manipulation, i.e. in the integrated condition (I), the percentage of correct recognition of the softer specimen in the pair is 100% with total confidence for all specimens compared with the standard.

A chi-squared binary test was performed to test the hypothesis of sample independence between the three conditions, using chi2bintest function for Matlab (Peder Axensten, © 2007). In this case, p-value expresses the error risk to claim that the samples are independent. A significant level of $\alpha = 0.05$ is assumed.

Results obtained when only cutaneous or kinaesthetic information were available to subjects ((C) and (K), respectively) are clearly weaker than those obtained in integrated conditions, and more so for specimens that are closer to the standard. Indeed, p-values resulting from the comparison of the outcomes between (I) and (K) are less than 0.05 for all probed pairs except for $SS3$-$SS5$. An analogous result is found for (I) and (C), in which $p < 0.05$ for all the pairs except for the specimens further away from the standard ($SS1$ and $SS2$). When stimuli are close to the standard, cutaneous and kinaesthetic information are almost equivalent ($p > 0.3$). For $SS1 - SS3$, cutaneous cues appear to provide more information than kinaesthetic ones, with an error risk of about 0.07 to claim that the samples are independent.

5.4.2 Ranking of Physical Specimens

Results from ranking experiments are shown in table 5.1, where subjective softness is reported versus objective compliance in a confusion matrix structure for the five specimens, under the three different conditions. Values on the diagonal express the amount of correct answers. The percentage of total accuracy is calculated considering the sum of all correct answers. The integrated modality (I) exhibits a percentage of total accuracy very close to 100%, with a diagonal structure. The relative weakness of unimodal cues is apparent also in these experiments. A departure from the perfect ranking is observed in the cutaneous-only condition (C), in terms of both departure from diagonal structure and total accuracy (66%). In kinaesthetic-only conditions (K), the discrepancy is even more pronounced (58%).

Table 5.1: Confusion matrices of ranking experiment results with physical specimens.

CL1 (I)	SS1	SS2	SS3	SS4	SS5	N	Relative Accuracy
SS1	29	0	1	0	0	30	86.67%
SS2	0	30	0	0	0	30	100.00%
SS3	1	0	28	0	1	30	93.34%
SS4	0	0	0	30	0	30	100.00%
SS5	0	0	1	0	29	30	96.67%
							Total Accuracy
N	30	30	30	30	30	150	98.67%

CL2 (K)	SS1	SS2	SS3	SS4	SS5	N	Relative Accuracy
SS1	18	3	1	0	8	30	60.00%
SS2	5	19	1	4	1	30	63.34%
SS3	0	0	19	9	2	30	63.34%
SS4	2	7	7	13	1	30	43.34%
SS5	5	1	2	4	18	30	60.00%
							Total Accuracy
N	30	30	30	30	30	150	58.00%

CL3 (C)	SS1	SS2	SS3	SS4	SS5	N	Relative Accuracy
SS1	24	3	1	1	1	30	80.00%
SS2	2	23	4	0	1	30	76.67%
SS3	2	4	16	0	8	30	53.34%
SS4	1	0	9	18	2	30	60.00%
SS5	1	0	0	11	18	30	60.00%
							Total Accuracy
N	30	30	30	30	30	150	66.00%

5.4.3 Pairwise Discrimination with Rendered Specimens

Figure 5.11 reports results from pairwise discrimination experiments with the haptic display under three different conditions. When the display is controlled to replicate both the kinaesthetic and cutaneous cues (integrated mode I), the correct discrimination rate is 100% for distant pairs (i.e., $SH1 - SH3$ and $SH5 - SH3$). As it could be

Table 5.2: Confusion matrices of ranking experiment results with rendered specimens.

CM1 (I)	SH1	SH2	SH3	SH4	SH5	N	Relative Accuracy
SH1	26	1	1	1	1	30	86.67%
SH2	1	27	0	1	1	30	90.00%
SH3	1	0	27	0	2	30	90.00%
SH4	1	1	1	26	1	30	86.67%
SH5	1	1	1	2	25	30	83.34%
							Total Accuracy
N	30	30	30	30	30	150	87.34%

CM2 (K)	SH1	SH2	SH3	SH4	SH5	N	Relative Accuracy
SH1	18	4	2	2	4	30	60.00%
SH2	6	12	6	5	1	30	40.00%
SH3	1	5	16	7	1	30	53.34%
SH4	3	6	6	15	0	30	50.00%
SH5	2	3	0	1	24	30	80.00%
							Total Accuracy
N	30	30	30	30	30	150	56.67%

CM3 (C)	SH1	SH2	SH3	SH4	SH5	N	Relative Accuracy
SH1	21	4	0	2	3	30	70.00%
SH2	4	23	0	1	2	30	76.67%
SH3	0	1	19	2	8	30	63.34%
SH4	5	0	10	15	0	30	50.00%
SH5	0	2	1	10	17	30	56.67%
							Total Accuracy
N	30	30	30	30	30	150	63.34%

expected, however, for the closer pair $SH2 - SH3$ ($p = 0.005$) artificially rendered specimens are discriminated in a considerably significant poorer way than their physical counterparts, while no difference is found for the pair $SH4 - SH3$ and their physical counterpart ($p = 0.31$).

The performance of subjects in discriminating softness is further lowered if only one cue is rendered. This degradation is more pronounced for rendered kinaesthetic cues than for rendered cutaneous

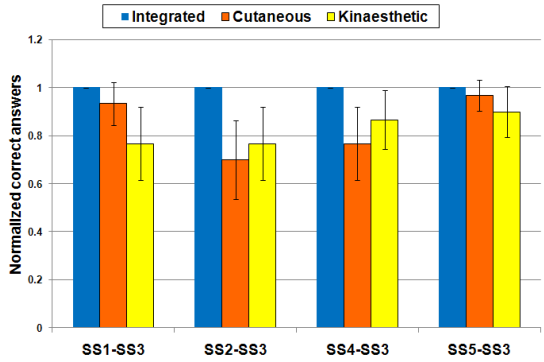

Figure 5.10: Results of pairwise discrimination experiments with silicone specimens under three different experimental conditions. Each bar represents the percentage of correct answers for each pair of specimens presented.

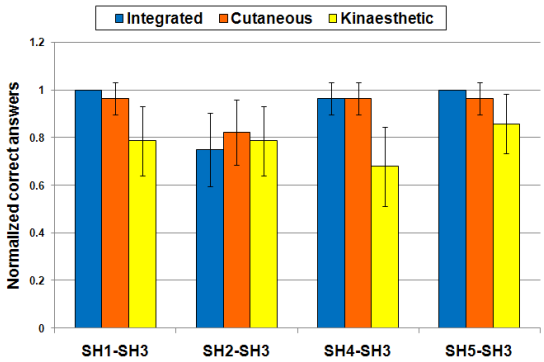

Figure 5.11: Results of pairwise discrimination experiments with artificially rendered specimens. Each bar represents the percentage of correct answers for each pair of specimens presented.

cues, as it results also from the p-values in table 5.3. In case of $SH2 - SH3$ discrimination, performance of subjects is comparable

	SH1-SH3	SH2-SH3	SH4-SH3	SH5-SH3
I vs. K	0.01	0.75	0.003	0.04
I vs. C	0.31	0.52	1	0.31
C vs. K	0.04	0.74	0.003	0.16

Table 5.3: p-values for the comparison between I, K and C for pairwise discrimination.

under the three conditions (I,K,C) ($p > 0.9$), with a percentage of correct recognition close to 80% (mean values are 0.75, 0.82 and 0.79 for (I), (C) and (K) conditions with a confidence interval 0.3, 0.27 and 0.29, respectively). The results support the conclusion that purely kinaesthetic haptic displays are inferior in softness discrimination with respect to cutaneous displays used in the experiments, and that integrated displays obtain the best performance, though this is still not quite as good as that of direct touch.

5.4.4 Ranking of Rendered Specimens

Experimental results on ranking experiments of artificially rendered specimens are shown in table 5.2. Total accuracy of softness perception using integrated haptic displays is weaker than with physical specimens, yet still strongly correlated to the commanded stimulus (87.35%). Results in terms of total accuracy and matrix structure for unimodal cues are very close to the ones observed in ranking experiments with physical specimens. Cutaneous-only stimuli reduce the softness ranking capability to 63.34%, while purely kinaesthetic rendering further reduces it to 56.67%, which is consistent with the results for silicone specimens. What can be concluded is that the integrated haptic device provides results similar to physical specimens in ranking experiments (in terms of both total accuracy and matrix structure), and the integrated modality exhibits the highest performance. Indeed, integrating cutaneous cues with kinaesthetic cues

in artificially rendering haptic softness information increases performance also in tasks such as ranking, which require multiple comparisons and involve haptic memory.

5.4.5 Comparison of Direct and Rendered Touch

The above experimental results of pairwise discrimination and ranking also provide some interesting insight in the evaluation of the performance of the here proposed haptic interface through a comparison with direct exploration of physical specimens. Results from the artificial display of kinaesthetic cues for softness are comparable with those obtained with real specimens ($p > 0.05$). The effects of naturally and artificially rendered cutaneous cues show that the haptic display provides comparable results than the real case ($p > 0.05$), except for the corresponding pair $SH4 - SH3$ and $SS4 - SS3$ ($p = 0.02$). The comparison of results for integrated haptic information between real and artificial stimuli is very satisfactory at both ends of the softness scale. As previously said, for finer discrimination tasks, i.e. materials that are closer in softness, even the integrated haptic display has obvious limitations. However, it is noteworthy that the total accuracy of ranking experiments for the three conditions I, K, and C are comparable for direct and indirect touch.

In summary, results further validate the technology of Contact Area Spread Rate (CASR) cutaneous softness rendering utilized in the here described haptic interface and in the fabric-based display described in Chapter 2, and encourage its use in connection with more traditional haptic interfaces.

5.5 Conclusions

In this work of thesis I have considered the role of kinaesthetic and cutaneous information in the discrimination of softness, both in direct and rendered touch. The results for both cases provide indications

consistent with those in [37] described for direct touch using different methods. Relying only on a touch modality limits the possibility for subjects to discriminate softness, while integrating kinaesthetic and cutaneous information certainly improves discrimination performance. This result can be interpreted in a synergy-inspired sense in terms of enhancement of the quality of the tactual perception with the increasing number of the elements of the perceptual basis employed in rendering.

What can be noticed is that subjects interacting with this new integrated haptic display actually seem to perceive different degrees of softness in a more realistic way. These results are encouraging towards the realization of convincing integrated kinaesthetic and cutaneous displays.

Bibliography

Author's

[A1] M. Bianchi, A. Serio, E. P. Scilingo, and A. Bicchi, "A new fabric-based softness display," in *Proc. IEEE Haptics Symposium*, 2010, pp. 105 –112, **Best Paper and Student Paper Award Finalist**.

[A2] M. Bianchi, E. P. Scilingo, A. Serio, and A. Bicchi, "A new softness display based on bi-elastic fabric," *World Haptics Conference*, pp. 382–383, 2009.

[A3] M. Bianchi, J. C. Gwilliam, A. Degirmenci, and A. M. Okamura, "Characterization of an air jet haptic lump display," in *Proc. IEEE Engineering in Medicine and Biology Society*, 2011, pp. 3467–3470.

[A4] J. C. Gwilliam, A. Degirmenci, M. Bianchi, and A. M. Okamura, "Design and control of an air-jet lump display," in *Proc. IEEE Haptics Symposium*, 2012, pp. 45–49.

[A5] M. Bianchi, P. Salaris, A. Turco, N. Carbonaro, and A. Bicchi, "On the use of postural synergies to improve human hand pose reconstruction," in *Proc. IEEE Haptics Symposium*, 2012, pp. 91–98.

[A6] M. Bianchi, P. Salaris, and A. Bicchi, "Synergy-based optimal design of hand pose sensing," in *Intelligent Robots and Systems, 2012*, 2012, submitted.

[A7] E. P. Scilingo, M. Bianchi, G. Grioli, and A. Bicchi, "Rendering softness: Integration of kinaesthetic and cutaneous information in a haptic device," *IEEE Transactions on Haptics*, vol. 3, no. 2, pp. 109 – 118, 2010.

[A8] E. P. Scilingo, M. Bianchi, N. Vanello, V. Hartwig, L. Landini, and A. Bicchi, *Immersive Multimodal Interactive Presence*. Springer-Verlag, London, 2012, ch. Artificially Rendered Cutaneous Cues for a New Generation of Haptic Displays, pp. 171–188.

[A9] M. Bianchi, G. Grioli, E. P. Scilingo, M. Santello, and A. Bicchi, "Validation of a virtual reality environment to study anticipatory modulation of digit forces and position," in *Proceedings of the 2010 international conference on Haptics - generating and perceiving tangible sensations: Part II*, ser. EuroHaptics'10. Berlin, Heidelberg: Springer-Verlag, 2010, pp. 136–143.

[A10] A. Bicchi, M. Bianchi, and P. Salaris, "Procedimento di ricostruzione virtuale di una posa reale di almeno una porzione di corpo umano," Italian Patent - submitted 232 012, 2012.

Miscellaneous

[11] B. Hannaford and A. M. Okamura, *Springer Handbook on Robotics*. Heidelberg, Germany: Springer, 2008, ch. Haptics, pp. 719–739.

[12] I. Kant, *Anthropologie in pragmatischer Hinsicht*. Reclams, Stuttgart, 1983.

[13] J. R. Augustine, *Human Neuroanatomy. An Introduction*. Elsevier, Inc., 2008.

[14] M. H. Schieber and M. Santello, "Hand function: peripheral and central constraints on performance," *Journal of Applied Physiology*, vol. 96, no. 6, pp. 2293 – 2300, 2004.

[15] M. L. Latash, *Synergy*. Oxford University Press, 2008.

[16] M. Santello, M. Flanders, and J. F. Soechting, "Postural hand synergies for tool use," *The Journal of Neuroscience*, vol. 18, no. 23, pp. 10 105 – 10 115, 1998.

[17] C. R. Mason, J. E. Gomez, and T. J. Ebner, "Hand synergies during reach-to-grasp," *J Neurophysiol*, vol. 86, pp. 2896 – 2910, 2001.

[18] A. Bicchi, "Hands for dextrous manipulation and robust grasping: a difficult road towards simplicity," *IEEE Trans. on Robotics and Automation*, vol. 16, no. 6, pp. 652 – 662, 2000.

[19] C. Brown and H. Asada, "Inter-finger coordination and postural synergies in robot hands via mechanical implementation of principal component analysis," in *IEEE-RAS International Conference on Intelligent Robots and Systems*, 2007, pp. 2877 – 2882.

[20] M. T. Ciocarlie, C. Goldfeder, and P. K. Allen, "Dimensionality reduction for hand-independent dexterous robotic grasping," in *IEEE/RSJ International Conference on Intelligent Robots and Systems*, 2007, pp. 3270 – 3275.

[21] M. T. Ciocarlie and P. K. Allen, "Hand posture subspaces for dexterous robotic grasping," *The International Journal of Robotics Research*, vol. 28, no. 7, pp. 851 – 867, 2009.

[22] A. Bicchi, M. Gabiccini, and M. Santello, "Modelling natural and artificial hands with sinergie," *Phil. Trans. R. Soc. B*, vol. 366, pp. 3153–3161, 2011.

[23] V. Panday, W. M. Bergmann Tiest, and A. M. L. Kappers, "The influence of edges as salient features in haptic shape perception of 3d objects," in *Proceedings IEEE World Haptics Conference*, 2011, pp. 529–532.

[24] V. Hayward, "Is there a "plenhaptic" function?" *Phil. Trans. R. Soc. B*, vol. 366, pp. 3115–3122, 2011.

[25] E. H. Adelson and J. R. Bergen, *Computational Models of Visual Processing*. MIT Press, 1991, ch. The plenoptic function and the elements of early vision, pp. 3 – 20.

[26] A. Bicchi, E. P. Scilingo, D. Dente, and S. Sgambelluri, *In Multipoint interaction with real and virtual objects*. STAR: Springer tracts in advanced robotics, 2005, ch. Tactile flow and haptic discrimination of softness, pp. 165–176.

[27] A. Bicchi, E. P. Scilingo, E. Ricciardi, and P. Pietrini, "Tactile flow explains haptic counterparts of common visual illusions," *Brain Res Bull.*, vol. 75, no. 6, pp. 737–741, 2008.

[28] B. K. P. Horn and B. G. Schunk, "Determining optical flow," *Artificial Intelligence*, vol. 17, pp. 185–203, 1981.

[29] K. O. Johnson, "The roles and functions of cutaneous mechanoreceptors," *Curr. Opin. Neurobiol.*, vol. 11, no. 4, pp. 455–461, August 2001.

[30] A. Bicchi, D. E. De Rossi, and E. P. Scilingo, "The role of the contact area spread rate in haptic discrimination of softness," *IEEE trans. on Robotics and Automation*, vol. 16, no. 5, pp. 496–504, October 2000.

[31] R. D. Howe, W. J. Peine, D. A. Kantarinis, and J. S. Son, "Remote palpation technology," *IEEE Engineering in Medicine and Biology Magazine*, vol. 14, no. 3, pp. 318–323, 1995.

[32] M. V. Ottermo, M. M. Ovstedal, T. Lango, O. Stavdahl, Y. Yavuz, T. A. Johansen, and R. Marvik, "The Role of Tactile Feedback in Laparoscopic Surgery," *Surgical Laparoscopy Endoscopy and Percutaneous Techniques*, vol. 16, no. 6, pp. 390–400, 2006.

[33] G. Moy, C. Wagner, and R. S. Fearing, "A compliant tactile display for teletaction," in *Proc. IEEE Internation Conference on Robotics and Automation.* Ieee, 2000, pp. 3409–3415.

[34] J. H. Killebrew, S. J. Bensmaia, J. F. Dammann, P. Denchev, S. S. Hsiao, J. C. Craig, and K. O. Johnson, "A dense array stimulator to generate arbitrary spatio-temporal tactile stimuli," *Journal of Neuroscience Methods*, vol. 161, no. 1, pp. 62–74, 2007.

[35] K. Inoue, F. Kato, and S. Lee, "Haptic device using flexible sheet and air jet for presenting virtual lumps under skin," in *Proceedings IEEE/RSJ Int'l Conf. on Intelligent Robots and Systems*, 2009, pp. 1749–1754.

[36] S. Mulatto, A. Formaglio, M. Malvezzi, and D. Prattichizzo, "Animating a synergy-based deformable hand avatar for haptic grasping," in *International Conference EuroHaptics*, vol. 2, 2010, pp. 203–210.

[37] M. A. Srinivasan and R. H. LaMotte, "Tactile discrimination of softness," *Journal of Neurophysiology*, vol. 73, no. 1, pp. 88–101, June 1995.

[38] C. U. M. Smith, *Biology of Sensory Systems, Second Edition*. John Wiley and Sons, 2008.

[39] J. Z. Wu, R. G. Dong, S. Rakhejia, A. W. Schopper, and W. P. Smutz, "A structural fingertip model for simulating of the biomechanics of tactile sensation," *Medical Engineering and Physics*, vol. 26, pp. 165–175, 2004.

[40] T. A. Kern, *Engineering Haptic Devices*. Springer-Verlag Berlin Heidelberg, 2009, ch. Biological Basics of Haptic Perception, pp. 35–58.

[41] H. C. Bastian, "The 'muscular sense': its nature and cortical localisation," *Brain*, vol. 10, pp. 1–137, 1888.

[42] G. M. Goodwin, D. I. McClosesky, and P. B. C. Matthews, "The contribution of muscle afferents to kinaesthesia shown by vibration induced illusions of movement and by the effects of paralysing joint afferents," *Brain*, vol. 95, pp. 705–748, 1972.

[43] W. R. Ferrell, S. C. Gandevia, and D. I. McClosesky, "The role of joint receptors in human kinaesthesia when intramuscular receptors cannot contribute," *J Physiol*, vol. 386, pp. 63–71, 1987.

[44] P. B. C. Matthews, *The Mammalian Muscle Receptors and Their Central Actions*. Edward Arnold, London, 1972.

[45] U. Proske and S. C. Gandevia, "The kinaesthetic senses," *J Physiology*, vol. 587, no. 17, pp. 4139–4146, 2009.

[46] M. R. Chambers, K. H. Andres, M. von Duering, and A. Iggo, "The strcuture and function of the slowly adapting type ii mechanoreceptor in hairy skin," *Q J Exp Physiol*, vol. 57, pp. 417–445, 1972.

[47] B. B. Edin and J. H. Abbs, "Finger movement responses of cutaneous mechanoreceptors in the dorsal skin of the human hand," *J Neurophysiology*, vol. 65, no. 3, pp. 657–670, 1991.

[48] B. B. Edin, "Quantitative analysis of static strain sensitivity in human mechanoreceptors from hairy skin," *J Neurophysiol*, vol. 57, pp. 1105–1113, 1992.

[49] B. B. Edin and N. Johansson, "Skin strain patterns provide kinaesthetic information to the human central nervous system," *J Neurophysiol*, vol. 487, no. 1, pp. 243–251, 1995.

[50] D. F. Collins, K. M. Refshauge, G. Todd, and S. C. Gandevia, "Cutaneous receptors contribute to kinaesthesia at the index finger, elbow and knee," *J Neurophysiology*, vol. 94, pp. 1699–1706, 2005.

[51] N. S. Weerakkody, D. A. Mahns, J. L. Taylor, and G. S. C, "Impairment of human proprioception by high-frequency cutaneous vibration," *J Physiology*, vol. 581, pp. 971–980, 2007.

[52] Q. Wang and V. Hayward, "Compact, portable, modular, high-performance, distributed tactile transducer device based on lateral skin deformation," in *14th Symposium on Haptic Interfaces For Virtual Environment And Teleoperator Systems IEEE VR*, 2006, pp. 67–72.

[53] C. R. Wagner, S. J. Lederman, and R. D. Howe, "Design and performance of a tactile shape display using rc servomotors," *Haptics-e*, vol. 3, p. 2004, 2003.

[54] S. L. Lederman and R. L. Klatzky, "Relative availability of surface and object properties during early haptic processing," *Journal of Experimental Psychology: Human Perception and Performance*, vol. 23, no. 6, pp. 1680–1707, December 1997.

[55] R. L. Klatzky, S. J. Lederman, and C. Reed, "Haptic integration of object properties:texture, hardness, and planar contour," *Journal of Experimental Psychology: Human Perception and Performance*, vol. 15, no. 1, pp. 45–57, 1989.

[56] R. L. Klatzky, S. J. Lederman, and D. E. Matula, "Imagined haptic exploration in judgements of objects properties," *J. Exper. Psychol. Learn., Mem, Cogn.*, vol. 17, no. 1, pp. 314–322, 1991.

[57] S. J. Lederman and R. L. Klatzky, "Hand movements: a window into haptic object recognition," *Cogn. Psychol.*, vol. 19, no. 12, pp. 342–368, 1987.

[58] S. D. Newman, R. L. Klatzky, S. J. Lederman, and M. A. Just, "Imagining material versus geometric properties of objects: an fmri study," *Cognitive Brain Research*, vol. 23, no. 3, pp. 235–246, 2005.

[59] K. L. Johnson, *Contact Mechanics*. Cambridge University Press, 1985.

[60] J. Jachowicz, R. McMullen, and D. Prettypaul, "Indentometric analysis of in vivo skin and comparison with artificial skin models," *Skin Research and Technology*, vol. 13, no. 6, pp. 299–309, 2007.

[61] M. Bergamasco, F. Salsedo, M. Fontana, F. Tarri, C. A. Avizzano, A. Frisoli, E. Ruffaldi, and S. Marcheschi, "High performance haptic device for force rendering in textile exploration," *The Visual Computer, Springer Berlin/Heidelberg*, vol. 23, no. 4, pp. 247–256, April 2007.

[62] P. Volino, P. Davy, U. Bonanni, C. Luible, N. Magnenat-Thalmann, M. Mäkinen, and H. Meinander, "From measured physical parameters to the haptic feeling of fabric," *The Visual Computer, Springer Berlin/Heidelberg*, vol. 23, no. 2, pp. 133–142, February 2007.

[63] C. Luible, M. Varheenmaam, N. Magnenat-Thalmann, and H. Meinander, "Subjective fabric evaluation," in *Int. Conference on Cyberworlds, HAPTEX'07 Workshop, IEEE Computer Society*, Hannover, Germany, October 2007, pp. 285–291.

[64] M. Varheenmaam and H. Meinander, "Mechanical properties as a base for haptic sensing of virtual fabrics," in *Proc. Autex 2007 Conference*, Tampere, Finland, June 2007.

[65] N. Magnenat-Thalmann, P. Volino, U. Bonanni, I. R. Summers, M. Bergamasco, F. Salsedo, and F. E. Wolter, "From physics-based simulation to the touching of textiles: The haptex project," *The International Journal of Virtual Reality*, vol. 6, no. 3, pp. 35–44, September 2007.

[66] R. C. Oldfield, "The assessment and analysis of handedness: The edinburgh inventory," *Neuropsychologia*, vol. 9, no. 1, pp. 97–113, March 1971.

[67] R. M. Friedman, K. D. Hetster, B. G. Green, and R. H. LaMotte, "Magnitude estimation of softness," *Exp Brain Res.*, vol. 191, no. 2, pp. 133–142, November 2008.

[68] A. M. Okamura, "Haptic feedback in robot-assisted minimally invasive surgery," *Current Opinion in Urology*, vol. 19, pp. 102–107, 2009.

[69] P. Goethals, "Tactile Feedback for Robot Assisted Minimally Invasive Surgery: An Overview," K. U. Leuven, Tech. Rep., 2008.

[70] Y. Kim, I. Oakley, and J. Ryu, "Human Perception of Pneumatic Tactile Cues," *Advanced Robotics*, vol. 22, no. 8, pp. 807–828, 2008.

[71] M. Culjat, C. H. King, M. Franco, J. Bisley, W. Grundfest, and E. Dutson, "Pneumatic balloon actuators for tactile feedback in robotic surgery." *Industrial Robot*, vol. 35, no. 5, pp. 449–455, 2008.

[72] K. B. Shimoga, "A survey of perceptual feedback issues in dexterous telemanipulation. II. Finger touch feedback," in *Proc. IEEE Virtual Reality Annual International Symposium*, 1993, pp. 271–279.

[73] S. A. Overduin and P. Servos, "Distributed digit somatotopy in primary somatosensory cortex," *NeuroImage*, vol. 23, no. 2, pp. 462–472, 2004.

[74] S. B. Pope, *Turbulent flows*. Cambridge Univ Press, 2000.

[75] T. Davanipour and S. Sami, "Short jet impingement," *Journal of the Hydraulics Division*, vol. 103, no. 5, pp. 557–567, 1977.

[76] C. V. Tu and D. H. Wood, "Wall pressure and shear stress measurements beneath an impinging jet," *Experimental Thermal and Fluid Science*, vol. 13, no. 4, pp. 364–373, 1996.

[77] H. J. Hussein, S. P. Capp, and W. K. George, "Velocity measurements in a high-Reynolds-number, momentum-conserving, axisymmetric, turbulent jet," *Journal of Fluid Mechanics*, vol. 258, no. 1, pp. 31–75, 1994.

[78] N. R. Panchapakesan and J. L. Lumley, "Turbulence measurements in axisymmetric jets of air and helium. Part 1. Air jet," *Journal of Fluid Mechanics*, vol. 246, pp. 197–197, 1993.

[79] ——, "Turbulence measurements in axisymmetric jets of air and helium. Part 2. Helium jet," *Journal of Fluid Mechanics*, vol. 246, no. 1, pp. 225–247, 1993.

[80] G. A. Gescheider, *Psychophysics: Method, Theory, and Application*. Hillsdale, NJ: Lawrence Erlbaum Associates, Inc., 1985.

[81] F. A. Wichmann and N. J. Hill, "The psychometric function: I. Fitting, sampling, and goodness of fit," *Perception & psychophysics*, vol. 63, no. 8, p. 1293, 2001.

[82] ——, "The psychometric function: II. Bootstrap-based confidence intervals and sampling," *Perception & psychophysics*, vol. 63, no. 8, p. 1314, 2001.

[83] L. Dipietro, A. M. Sabatini, and P. Dario, "A survey of glove-based systems and their applications," *Systems, Man, and Cybernetics, Part C: Applications and Reviews, IEEE Transactions on*, vol. 38, no. 4, pp. 461 –482, 2008.

[84] D. J. Sturman and D. Zeltzer, "A survey of glove-based input," *Computer Graphics and Applications, IEEE*, vol. 14, no. 1, pp. 30–39, 1994.

[85] J. M. Elliott and K. J. Connolly, "A classification of manipulative hand movements," *Dev Med Child Neurol*, vol. 26, pp. 283–296, 1984.

[86] M. R. Cutkosky, "On grasp choice, grasp models, and the design of hands for manufacturing tasks," *IEEE Trans Rob Auto*, vol. 5, pp. 283–272, 1989.

[87] J. Fish and J. F. Soechting, "Synergistic finnger movements in a skilled motor task," *Exp Brain Res*, vol. 91, pp. 327–334, 1992.

[88] J. F. Soechting and M. Flanders, "Hand synergies during reach-to-grasp," *J Comput Neurosci*, vol. 4, pp. 29 – 46, 1997.

[89] T. E. Jerde, J. F. Soechting, and M. Flanders, "Biological constraints simplify the recognition of hand shapes," *IEEE Trans Biomed Eng*, vol. 50, pp. 265–269, 2003.

[90] A. M. Gordon, *Handbook of Brain and Behaviour in Human Development*. The Netherlands: Kluwer Academic, 2001, ch. Development of hand motor control, pp. 513 – 537.

[91] M. Santello, M. Flanders, and J. F. Soechting, "atterns of hand motion during grasping and the influence of sensory guidance," *J Neurosci*, vol. 22, pp. 1426–1435, 2002.

[92] T. E. Jerde, J. F. Soechting, and M. Flanders, "Coarticulation in fluent fingerspelling," *J Neurosci*, vol. 23, pp. 2383–2393, 2003.

[93] P. Braido and X. Zhang, "Quantitative analysis of finger motion coordination in hand manipulative and gestic acts," *Human Mov Sci*, vol. 22, pp. 661–678, 2004.

[94] E. Todorov and Z. Ghahramani, "Analysis of the synergies underlying complex hand manipulation," in *IEEE Proceedings Eng Med Biol Soc*, vol. 6, 2004, pp. 4637–4640.

[95] P. H. Thakur, A. J. Bastian, and S. S. Hsiao, "Multidigit movement synergies of the human hand in an unconstrained haptic exploration task," *J Neurosci*, vol. 28, pp. 1271–1281, 2008.

[96] M. Gabiccini and A. Bicchi, "On the role of hand synergies in the optimal choice of grasping forces," in *Robotics Science and Systems*, 2010.

[97] K. Cho, J. Rosmarin, and H. Asada, "Design of vast dof artificial muscle actuators with a cellular array structure and its application to a fivefingered robotic hand," in *Proc. IEEE Internation Conference on Robotics and Automation.* Ieee, 2006, pp. 2214–2219.

[98] D. Prattichizzo, M. Malvezzi, and A. Bicchi, "On motion and force controllability of grasping hands with postural synergies," in *Proceedings of Robotics: Science and Systems*, vol. 2, 2010.

[99] A. Tarantola, *Inverse Problem Theory and Model Parameter Estimation*. SIAM, 2005.

[100] P. C. Mahalanobis, "On the generalised distance in statistics," *Proceedings of the National Institute of Sciences of India*, vol. 2, no. 1, pp. 49 – 55, 1936.

[101] D. M. Hawkins, *Identification of Outliers*. Chapman and Hall, London, 1980.

[102] W. Hardle and L. Simar, *Applied Multivariate Statistical Analysis*. Springer-Verlag Berlin Heidelber New York, 2007.

[103] A. Gelb, *Applied Optimal Estimation*. M.I.T. Press, Cambridge, US-MA, 1974.

[104] Q. Fu and M. Santello, "Tracking whole hand kinematics using extended kalman filter," in *Engineering in Medicine and Biology Society (EMBC), 2010 Annual International Conference of the IEEE*, 2010, pp. 4606 – 4609.

[105] G. Stillfried and P. van der Smagt, "Movement model of a human hand based on magnetic resonance imaging (mri)," in *Proc. ICABB*, 2010.

[106] X. Zhang, S. Lee, and P. Braido, "Determining finger segmental centers of rotation in flexion-extension based on surface marker measurement," *Journal of Biomechanics*, vol. 36, pp. 1097 – 1102, 2003.

[107] J. Chambers, W. Cleveland, and B. Kleiner, *Graphical Methods for Data Analysis*. Wadsworth and Brooks/Cole, Pacific Grove, CA, USA, 1983.

[108] H. E. T. Holgersson, "A graphical method for assessing multivariate normality," *Computational Statistics*, vol. 21, pp. 141–149, 2006.

[109] C. R. Rao, *Linear Statistical Inference and Its Applications*. Wiley , New York, 1973.

[110] A. Bicchi and G. Canepa, "Optimal design of multivariate sensors," *Measurement Science and Technology (Institute of Physics Journal "E")*, vol. 5, pp. 319–332, 1994.

[111] L. K. Simone, N. Sundarrajan, X. Luo, Y. Jia, and D. G. Kamper, "A low cost instrumented glove for extended monitoring and functional hand assessment." *Journal of Neuroscience Methods*, vol. 160, no. 2, pp. 335–348, 2007.

[112] S. Wise, W. Gardner, E. Sabelman, E. Valainis, Y. Wong, K. Glass, J. Drace, and J. M. Rosen, "Evaluation of a fiber optic glove for semi-automated goniometric measurements." *Journal Of Rehabilitation Research And Development*, vol. 27, no. 4, pp. 411–424, 1990.

[113] A. Tognetti, N. Carbonaro, G. Zupone, and D. E. De Rossi, "Characterization of a novel data glove based on textile integrated sensors," in *Annual International Conference of the IEEE Engineering in Medicine and Biology Society, EMBC06, Proceedings.*, 2006, pp. 2510 – 2513.

[114] F. Lorussi, W. Rocchia, E. P. Scilingo, A. Tognetti, and D. E. De Rossi, "Wearable, redundant fabric-based sensor arrays for reconstruction of body segment posture," *Sensors Journal, IEEE*, vol. 4, no. 6, pp. 807 – 818, 2004.

[115] A. Tognetti, N. Carbonaro, G. Dalle Mura, M. Tesconi, G. Zupone, and D. E. De Rossi, "Sensing garments for body posture and gesture classification," *TECHNICAL USAGE TEXTILES Magazine*, vol. 68, pp. 33–39, 2008.

[116] F. Pukelsheim, *Optimal Design of Experiments (Classics in Applied Mathematics) (Classics in Applied Mathematics, 50)*. Philadelphia, PA, USA: Society for Industrial and Applied Mathematics, 2006.

[117] K. Chaloner and I. Verdinelli, "Bayesian experimental design: A review," *Statistical Science*, vol. 10, no. 3, pp. 273–304, 1995.

[118] S. Ghosh and C. R. Rao, "Review of optimal bayes designs," in *Design and Analysis of Experiments*, ser. Handbook of Statistics. Elsevier, 1996, vol. 13, pp. 1099 – 1147.

[119] A. Bicchi, "A criterion for optimal design of multiaxis force sensors," *Journal of Robotics and Autonomous Systems*, vol. 10, no. 4, pp. 269–286, 1992.

[120] A. J. Helmicki, C. A. Jacobson, and C. N. Nett, "Control oriented system identification: a worst-case/deterministic approach in h$^\infty$," *Automatic Control, IEEE Transactions on*, vol. 36, no. 10, pp. 1163 –1176, oct 1991.

[121] R. Tempo, "Robust estimation and filtering in the presence of bounded noise," *Automatic Control, IEEE Transactions on*, vol. 33, no. 9, pp. 864 –867, sep 1988.

[122] D. J. Sturman and D. Zeltzer, "A design method for whole-hand human-computer interaction," *ACM Trans. Inf. Syst.*, vol. 11, no. 3, pp. 219–238, 1993.

[123] J. Edmison, M. Jones, Z. Nakad, and T. Martin, "Using piezoelectric materials for wearable electronic textiles," in *Wearable Computers, 2002. (ISWC 2002). Proceedings. Sixth International Symposium on*, 2002, pp. 41 – 48.

[124] F. Vecchi, S. Micera, F. Zaccone, M. C. Carrozza, A. M. Sabatini, and D. P., "A sensorized glove for applications in biomechanics and motor control," in *Annu. Conf. Int. Functional Electr. Simulation Soc.*, 2001.

[125] L. Y. Chang, N. S. Pollard, T. M. Mitchell, and E. P. Xing, "Feature selection for grasp recognition from optical markers," in *Intelligent Robots and Systems, 2007. IROS 2007. IEEE/RSJ International Conference on*, 2007, pp. 2944–2950.

[126] C. R. Rao, "The use and interpretation of principal component analysis in applied research," *The Indian journal of statistic*, 1964.

[127] J. B. Rosen, "The gradient projection method for nonlinear programming. part i. linear constraints," *Journal of the Society for Industrial and Applied Mathematics*, vol. 8, no. 1, pp. 181 – 217, 1960.

[128] K. Diamantaras and K. Hornik, "Noisy principal component analysis," *Measurement'93*, pp. 25 – 33, 1993.

[129] M. M. Zavlanos and G. J. Pappas, "A dynamical systems approach to weighted graph matching," in *Decision and Control, 2006 45th IEEE Conference on*, 2006, pp. 3492 – 3497.

[130] L. Yobas, D. M. Durand, G. G. Skebe, F. J. Lisy, and M. A. Huff, "A novel integrable microvalve for refreshable braille display system," *IEEE J. of Microelectromech. Syst.*, vol. 12, no. 3, pp. 252–263, 2003.

[131] V. H. V. Levesque, J. Pasquero and M. Legault, "Display of virtual braille dots by lateral skin deformation: Feasibility study," *ACM Trans. on Applied Perception*, vol. 2, no. 2, pp. 132–149, April 2005.

[132] S. Koroki, H. Kajimoto, H. Nii, N. Kawakami, and S. Tachi, "Proposal for tactile sense presentation that combines electrical and mechanical stimulus," *ACM Trans. on Applied Perception*, vol. 2, no. 2, pp. 132–149, 2005.

[133] K. Fujita and H. Ohmori, "A new softness display interface by dynamic fingertip contact area control," in *World Multiconf. on Systemics, Cybernetics and Informatics*, Orlando, Florida (USA), July 2001, pp. 78–82.

[134] H. Yokota, A. Yamamoto, H. Yamamoto, and T. Higuchi, "Producing softness sensation on an electrostatic texture display for rendering diverse tactile feelings," in *Second Joint EuroHaptics Conference and Symposium on Haptic Interfaces for Virtual Environment and Teleoperator Systems*, vol. 23, no. 6, Tsukuba, Japan, 2007, pp. 584–585.

[135] D. Pawluk and R. Howe, "Dynamic contact of the human fingerpad against a flat surface," *J Biomech Eng*, vol. 121, no. 6, pp. 605–611, 1999.

[136] ——, "Dynamic lumped element response of the human fingerpad," *J Biomech Eng*, vol. 121, no. 2, pp. 178–183, 1999.

[137] E. Serina, E. Mockensturm, C. Mote Jr, and D. Rempel, "A structural model of the forced compression of the fingertip pulp," *J Biomech*, vol. 31, no. 7, pp. 639–646, 1998.

[138] E. P. Scilingo, N. Sgambelluri, G. Tonietti, and A. Bicchi, "Integrating two haptic devices for performance enhancement," in *World Haptics Conference*, Tsukuba, Japan, March 2007, pp. 139–144.